Bioderived therapeutics for chronic liver diseases

Inaugural dissertation

of the Faculty of Science,

University of Bern

presented by

Aymar Abel Ganguin

from Eschert (BE)

Supervisor of the doctoral thesis:

Prof. Dr. Paola Luciani

Department of Chemistry, Biochemistry and Pharmaceutical Sciences,

University of Bern

Bioderived therapeutics for chronic liver diseases

Inaugural dissertation

of the Faculty of Science,

University of Bern

presented by

Aymar Abel Ganguin

from Eschert (BE)

Supervisor of the doctoral thesis:

Prof. Dr. Paola Luciani

Department of Chemistry, Biochemistry and Pharmaceutical Sciences,

University of Bern

Accepted by the Faculty of Science.

Bern, May 28th, 2023

The Dean

Prof. Dr. Marco Herwegh

Table of Contents

Chapter 1.
Background and Purpose

Parts of this chapter has been published as a chapter in the book “Microfluidics for Cellular Applications”, Edc.: Perozziello G., Kruhne U., Luciani P., Elsevier Science Publishing Co Inc, 2023, 978-0-12-822482-3

Aymar Abel Ganguin, Simone Aleandri, Paola Luciani

Department of Chemistry, Biochemistry and Pharmaceutical Sciences, University of Bern, Bern, Switzerland

Author’s contribution

A.G. led manuscript writing. P.L. and S.A. reviewed and edited the manuscript.

1.1. The liver and its function

The liver is a vital organ crucial for physiological functions of the human body[1]. It is covered by the Glisson capsule, a connective tissue, and located under the diaphragm in the right upper quadrant behind the ribcage[2]. It is built by a large right lobe and smaller left lobes, consisting of a total of eight independent segments with their own vascular and biliary branches (**Figure 1.1.**)[2]. These segmentations are beneficial for transplantations and cancer removals, as they allow for healthy tissue to be preserved and minimizes blood loss through removal of the affected segments only[3]. Each liver segment is further divided into lobules, which are hepatocytes assembled in a hexagonal shape as plates that expand from a central vein (**Figure 1.1.**)[2, 4]. Hepatocytes account for 70% of the total liver mass[5]. The liver also contains non-parenchymal cells that are vital for its function, including epithelial cells (cholangiocytes), sinusoidal endothelial cells, Kupffer cells, liver-associated lymphocytes, biliary cells, and hepatic stellate cells (HSCs), which all interact together through direct cell-cell contact and soluble mediators (**Figure 1.1.**)[4, 6]. Lobules can be further divided into portal triads, which are built by arterial, venous, and biliary vessels[7].

Blood enters the liver through two different pathways, with approximately 75% coming through the portal vein, being rich in nutrients and toxins absorbed from the gastrointestinal tract, and about 25% being oxygenated and coming from the hepatic artery[8]. Blood mixes in the sinusoids, which are capillaries with discontinued endothelium located in the space between lobules, and drains into the central vein exiting the liver with a flow rate of about 1.5 L of blood/min[9, 10]. Fenestrated membranes of sinusoidal endothelial cells allow for an efficient exchange between blood and hepatocytes, enabling proper liver function[9]. Located between the sinusoids and hepatocytes is

the space of Disse, which hosts dendritic cells as well as HSCs, also known as Ito cells (**Figure 1.1.**)[11].

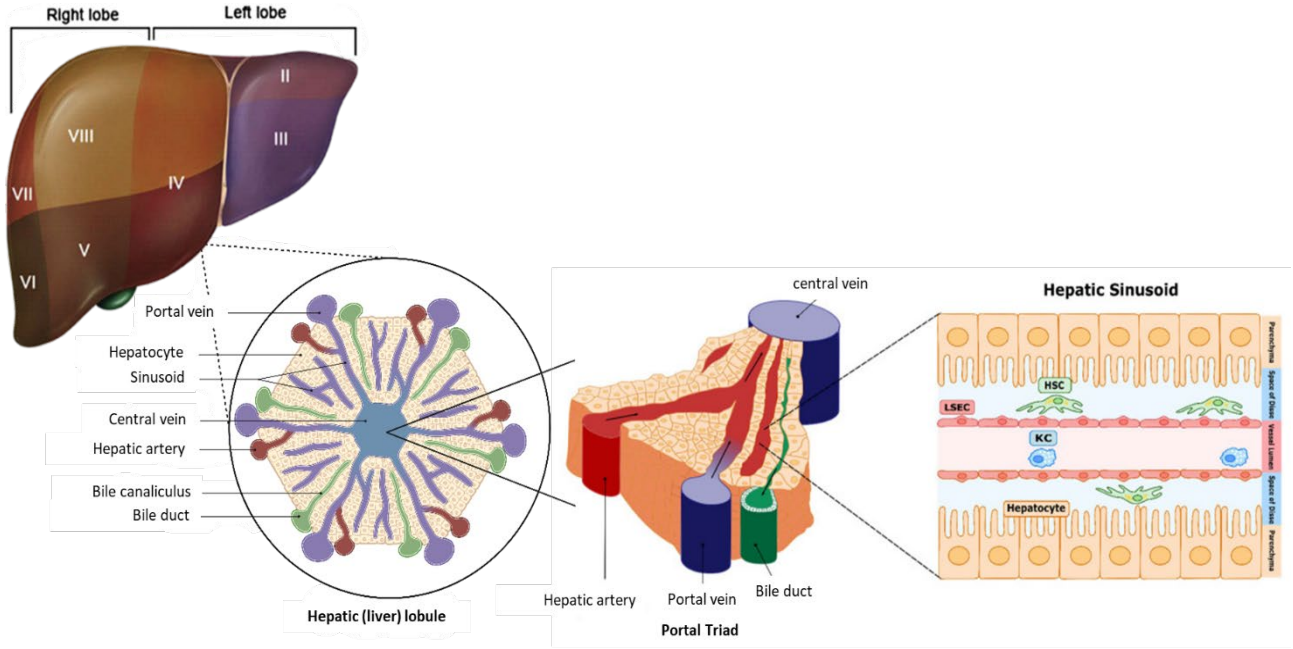

Figure 1.1. Anatomy of the liver.

The liver can be separate into 2 lobes and eight segment (I-VIII), whereas segment I is on the other side of the liver in between segment II, VII, and gallbladder. Each segment consists of hepatic lobules which are assembled in a hexagonal shape around a central vein. Hepatic lobules are built from portal triads, which contain the hepatic artery, portal vein and a bile duct. Lobules are separated by capillaries, also known as hepatic sinusoids. In the sinusoids molecules from the blood can pass through fenestrated sinusoidal endothelial cells (LSEC) and interact with hepatic stellate cells (HSC) in the space of Disse, as well as hepatocytes, allowing signaling between Kupffer cells (KC), HSCs and hepatocytes.

Image adapted from "The Hepatic Sinusoid in Chronic Liver Disease: The Optimal Milieu for Cancer" (Gilbert Ramos et al., 2021) and "Liver anatomy" (Abdel-Misih et al., 2010) and partially created in BioRender.com.

The functions of the liver include clearance of damaged erythrocytes (red blood cells), management of nutrients (such as lipids, carbohydrates, and vitamins), and synthesis of plasma proteins (such as globulins, albumin, protein C, insulin-like growth factors, and clotting factors)[2,

[12-14]. It is also the main organ for detoxifying harmful substances, being essential to the maintenance of overall health and well-being[2, 15].

Xenobiotics, which are harmful toxins that can enter the body through various routes such as ingestion, inhalation, or through wounds are eliminated in a two-step process consisting of biotransformation and conjugation[16, 17]. However, during the process non-toxic molecules can be transformed into toxic ones, potentially causing hepatic injury, which if unresolved can led to chronic liver diseases[16].

1.1.1. Chronic liver disease formation and fibrosis progression

Chronic liver diseases originate as a wound-healing process to liver injury[18]. The liver has an enormous potential for tissue repair and can return to normal size after 90% of tissue removal[19]. However, if the wound healing process gets dysregulated it becomes dangerous as the liver steadily progresses to liver cirrhosis and liver failure[20]. Wound healing renders the liver more resistant to acute injury and collagen type 1 protects hepatocytes against several toxic substances, but excessive extracellular matrix production leads to scars and altered tissue function, till complete functional loss[21, 22]. The most common causes of liver injury are diabetes, alcohol abuse, bad diet, non-alcoholic fatty liver disease (NAFLD), and hepatitis[23-25] (**Figure 1.2.**). The repetitive injury to the liver due to those named causes leads to damage of the cholangiocytes and hepatocytes resulting in an overactivated regeneration[22, 26].

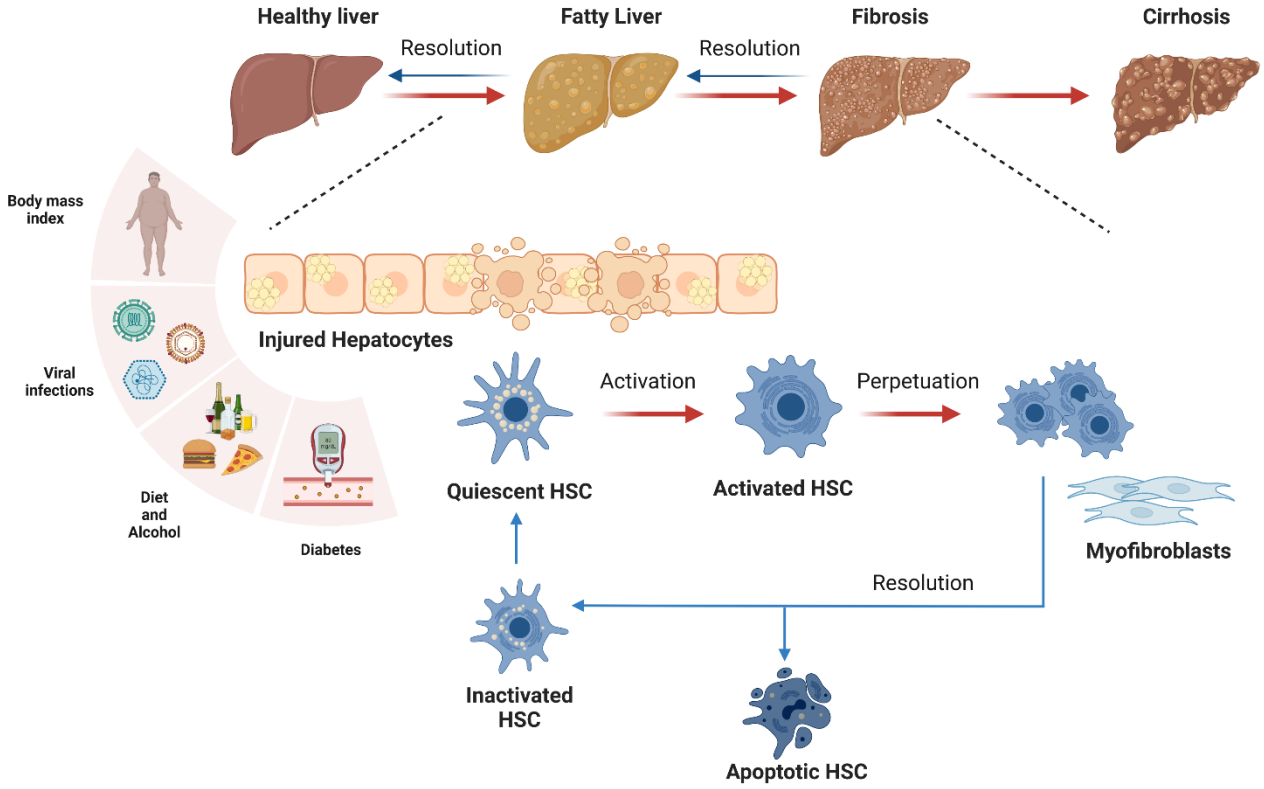

Figure 1.2. Progression of chronic liver diseases.

Chronic liver injuries, such as due to alcohol abuse, fatty diet, obesity, viral infections, or diabetes, lead to an inflammation of the liver forming a fatty liver. If the injury is not resolved, injured hepatocyte can activate quiescent HSCs resulting in fibrosis formation. Perpetuated HSCs can be deactivated leading either to apoptotic HSCs or inactivated quiescent-like HSCs. If the fibrosis further develops to cirrhosis no resolution can be obtained anymore resulting in the need of a liver transplantation.

Image created in BioRender.com

NAFLD is worldwide the most abundant liver disease with a prevalence of 25% with a continues increase[27]. Development of NAFLD is very complex and involves several molecular and metabolic changes described as a "multiple hits" hypothesis[28]. NAFLD can further progress either to non-alcoholic fatty liver (NAFL), also known as fatty liver, or into non-alcoholic steatohepatitis (NASH)[28-30]. NAFL tends to be benign, however, if not diagnosed and left untreated it can progress into NASH, which is way more serious and increases the chances drastically for further progression to fibrosis, cirrhosis, liver failure or hepatocellular carcinoma (liver cancer) (**Figure**

1.2.)[31, 32]. Mitochondrial dysfunctions contribute significantly to the development of hepatic steatosis[33, 34]. The accumulation of cholesterol, as well as free fatty acids in mitochondrial leads to the formation and release of reactive oxygen species (ROS) damaging hepatocytes[34]. The apoptotic hepatocytes release their cellular content which triggers Kupffer cells to release pro-inflammatory mediators such as interleukin (IL) 6, tumor necrosis factor alpha and IL-1b and especially pro-fibrotic factors such as transforming growth factor beta 1 (TGF-β_1), progressing the fibrosis[26]. Those factors, among other cytokines, stimulate a transdifferentiation of HSCs from a quiescent status into an activated myofibroblast-like status[22, 26, 35-37].

HSCs have been described to be the key player in fibrosis progression[38, 39]. They are lipophagic and fat storing cells and residue in the space of Disse between hepatocytes and endothelial cells and are therefore targetable through the blood system. Hepatic stellate cells are mesenchymal cell types and account for 5-8% of the total healthy liver mass[39]. They are not only responsible for Vitamin A storage as retinyl esters but also contribute to vasoregulation and extracellular matrix homeostasis, liver development, and drug and retinoid metabolism[40]. Upon activation they undergo functional and morphological changes demonstrated by a drastic altered gene expression profile enabling enhanced proliferation and development[41]. The activation process can be divided into an initiation phase and a perpetuation phase[42]. The initiation phase, also called the proinflammatory phase, is the primary answer to paracrine stimuli from damaged parenchymal cells and is characterized by early changes in phenotype and gene expression. Non-resolution of this phase leads to the perpetuation stage which is regulated by autocrine and paracrine stimuli and characterized by distinct changes in HSCs including proliferation, matrix degradation, enhanced contractility due to elevated cytoskeleton filament expression, increased extracellular matrix expression, chemotaxis and loss of retinoids[42, 43]. However, liver fibrosis has been described as

being reversible upon termination of the liver injury[44]. This process, also called the resolution phase, HSCs either reverse into a quiescent status or become apoptotic through numerous pathways[43, 44]. The pivotal role of HSCs in liver fibrosis, their resolution potential, and their accessibility in the space of Disse make those cells suitable therapeutical targets for antifibrotic compounds[42, 45, 46].

Nevertheless, currently no specifically for liver fibrosis approved treatment exists. The available options are meant to address the underlying causes such as steroids to treat excessive inflammation in autoimmune hepatitis or entecavir, an antiviral agent, to treat viral hepatitis[47, 48]. Other drugs involve obeticholic acid and elafibranor, which are both currently into phase 3 clinical trials (https://clinicaltrials.gov/ct2/show/NCT02548351/https://clinicaltrials.gov/ct2/show/NCT05627362) for NASH patients.

1.1.2. Essential phospholipids as potential therapy

Due to their supposed anti-inflammatory and antioxidant properties, essential phospholipids (EPLs) have been used as an approach to manage fatty liver disease[49]. Studies on phospholipids and their involvement in liver regeneration date back half a century[50]. EPLs are highly purified soybean extracts, enriched in polyenylphosphatidylcholines (PPCs, >72%) with 1,2-dilinoleoylphosphatidylcholine (DLPC) being the most abundant lipid[51] DLPC is a polyunsaturated lipid with a *36:4* structure and considered as the active component of PPCs[49]. Previous studies have shown that PPCs suppressed collagen and αSMA expression in human HSCs by reducing TGF-β_1 induces ROS production[52, 53]. Previous research in our group showed that unilamellar liposomes (particle surrounded by a lipid bilayer entrapping an aqueous core, **Figure 1.3.**) formed with S80 lipids (soybean extract with 73-79% phosphatidylcholine) show a fibrosis-resolving potential in an *in vitro* model of LX-2 cells, an immortalized HSC cell line with key

features of hepatic stellate cells[54, 55]. Administration of S80 liposomes on naïve and TGF-β_1 activated LX-2 cells restored lipid droplets and decreased main fibrotic markers, such as collagen and αSMA[45]. Nevertheless, further experiments are required to understand the underlying mechanism of action and understand the resolution phase. Further efforts are happening in our lab trying to form S80 tablets as an easily administrable drug.

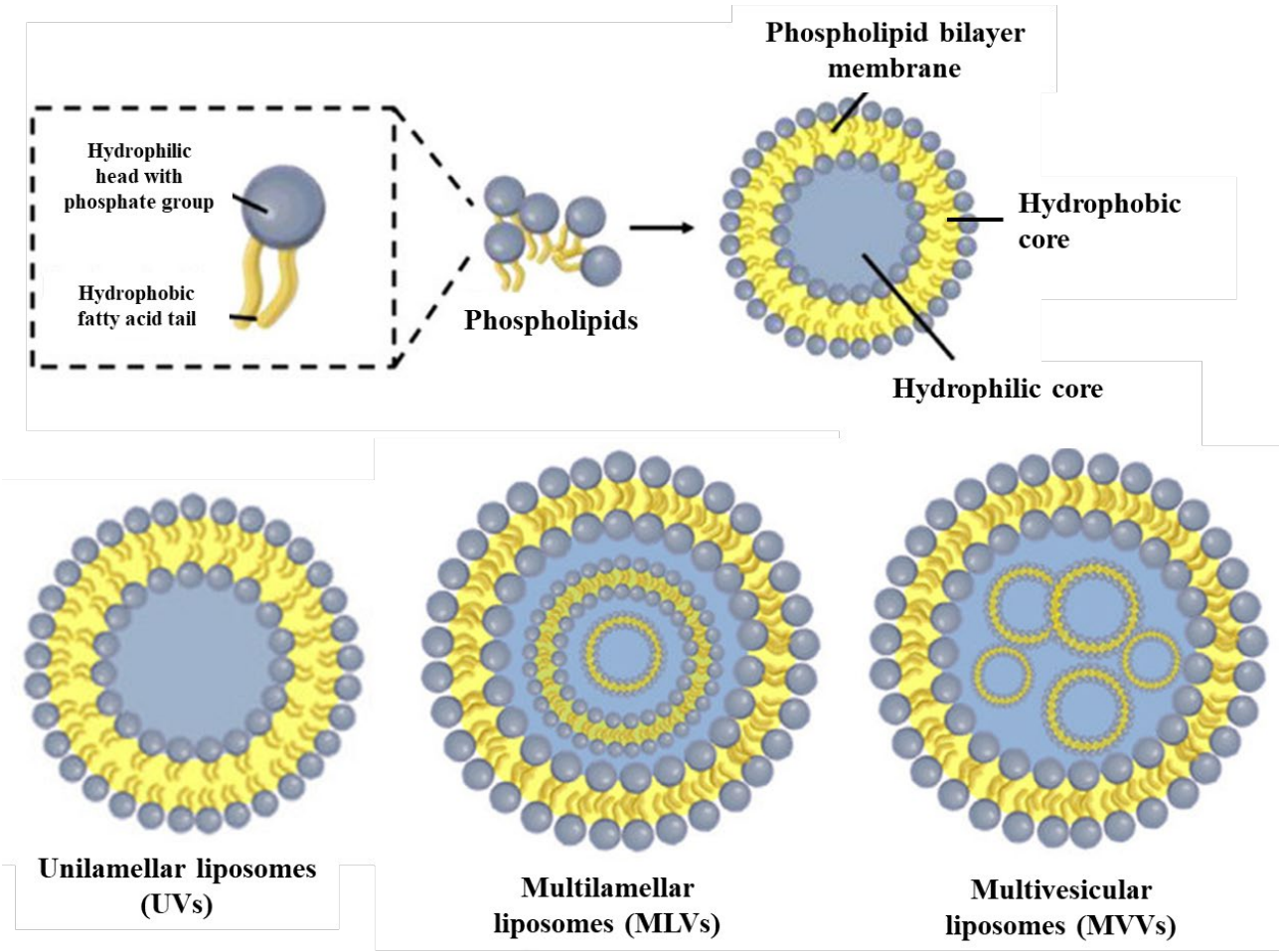

Figure 1.3. Classification of liposomes.

Liposomes are typically built from phospholipids which are characterized by a hydrophilic head containing a phosphate group and hydrophobic fatty acid tails. The phospholipids form a hydrophobic lipid bilayer entrapping a hydrophilic core, which is composed of the lipid rehydration buffer used. Liposomes can be categorized depending on their lamellarity and composition. The most common liposome types are unilamellar liposomes (UVs) ranging from 50 nm to several µm, multilamellar liposomes (MLVs), which are typically bigger than one µm, and multivesicular liposomes (MVVs), which are liposomes entrapping other MLVs or UVs and in the µm size range.

Image adapted from "Liposome-based delivery of biological drugs" (Kosheli Thapa Magar et al., 2022)

1.2. Extracellular vesicles

Extracellular vesicles (EVs) refer to particles enclosed by a lipid membrane which are released by all eukaryotic cell types, and which are typically categorized by their biogenesis (**Figure 1.4.**)[56, 57]. Dying cells release apoptotic bodies through blebbing of the cell membrane. Apoptotic bodies are the EVs with the broadest size distribution, ranging from a few nm till several µm in diameter and are often combined with microvesicles under one term. Microvesicles, also known as ectosomes or oncosomes, originate from the outward budding and fission of the cellular plasma membrane and vesicles formation[58]. They typically range from 50 nm to 500 nm, but have been described to reach sizes in the µm range as well[56]. Exosomes are intra-luminal vesicles (ILVs) formed by the inward budding of endosomal membrane in the early endosome during the maturation of multi-vesicular bodies (MVBs), which are intermediate structures in the endosomal system (**Figure 1.4.**).

They are secreted into the extracellular lumen upon the fusion of MVEs with the cell membrane[59]. Exosomes are generally described to have a diameter of 30 – 150 nm[56, 57] with some studies claiming sizes up to 200 nm[60, 61]. Currently it is still not possible to distinguish different EVs subtypes smaller than 200 nm once collected from a biofluid, due to overlapping compositions, sizes, densities, and membrane markers[56, 62]. They can only be distinguished if the biogenesis of the vesicle was observed e.g., through microscopy. Originally EVs were considered to be just waste carriers, this with the fact that they are largely heterogenous hindered the research and characterization of those particles for a long time.

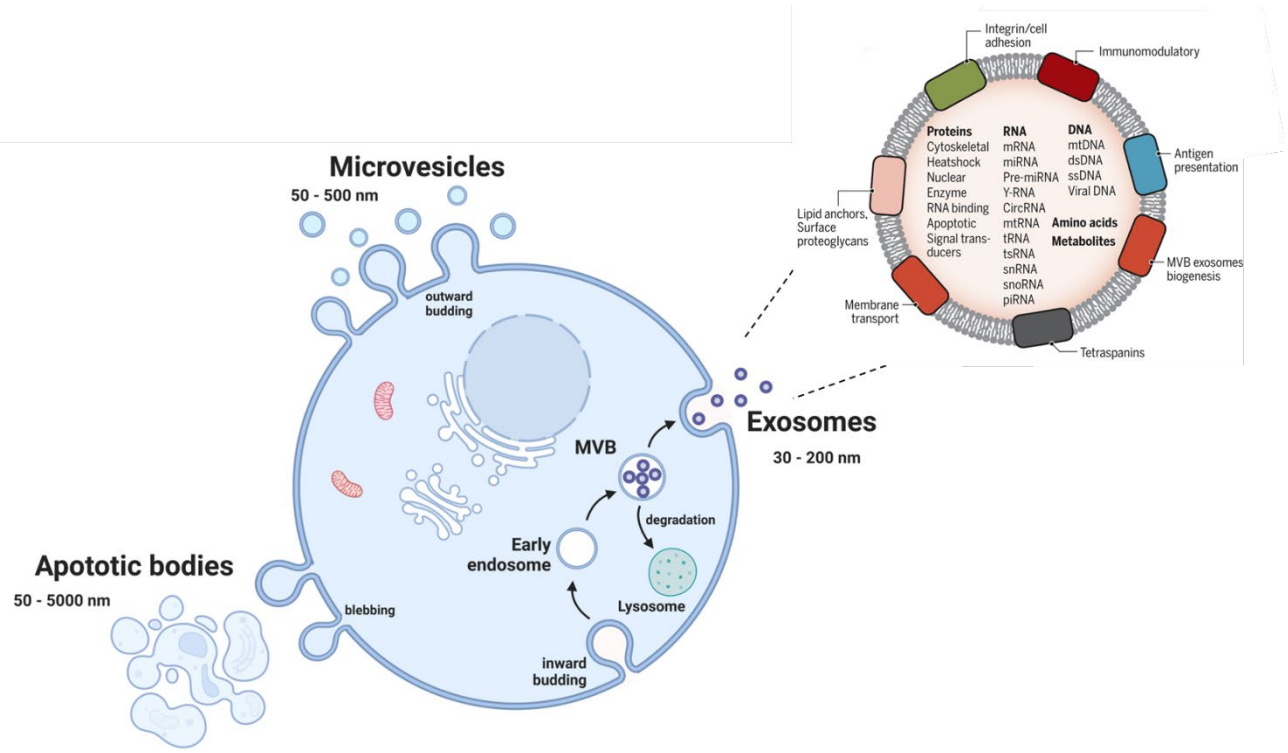

Figure 1.4. Biogenesis of Extracellular Vesicles.

EVs are categorized based on their biogenesis. Apoptotic bodies form upon blebbing, whereas microvesicles form upon outward budding of the plasma membrane. Exosomes are formed through the endosomal system and are either released in the extracellular space via exocytosis or are degraded by lysosomes. Exosomes are surrounded by a lipid bilayer and contain various (trans-)membrane proteins, peptides, glycosides, nucleic acids etc. which contribute to their function.

Image adapted from "The biology, function, and biomedical applications of exosomes" (Raghu Kalluri et al., 2020) and partially created in BioRender.com.

However, EVs have been found to play a crucial role in various (patho)physiological processes such as intercellular communication, cancer development, and infection propagation, by enabling the exchange of genetic material, proteins, and lipids among cells[56, 63, 64]. They have been described to show no or very low immunogenicity, to be able to cross biological barriers, to allow short-distance and long-distance communication, to protect cargo from degradation, and to functionally deliver cargo to a host cell via, different mechanisms such as membrane fusion,

phagocytosis, pinocytosis, and endocytosis[56, 63-66]. Therefore, EVs show an enormous potential as diagnostics, therapeutics, and drug delivery systems[63, 65, 67, 68]. EVs derived from stem cells and dendritic cells have been described in various studies to modify the immune answer lowering inflammation or induce inflammation in cancer patients[69-71]. Additionally, EVs can be used as drug delivery systems delivering various loaded cargo, such as small drug molecules, siRNA, miRNA, mRNA, CRISPR/Cas9, proteins, and peptides[63, 72, 73]. Due to preserved homing effect in EVs, the particles show a natural property for targeted drug delivery, which is a big advantage compared to conventional liposome systems which are typically conjugated with ligands such as antibodies, antibody derivatives, and aptamers, specific for receptors on the target cell to achieve targeted delivery, leading to immune responses and other complications[74-78]. The loading techniques can be divided in two separated approaches. First, by manipulation of the host cell, either true cargo loading into the host cell or through genetic modification resulting in EVs with the desired cargo. Secondly, EVs can be loaded post isolation, such as through sonication, electroporation, incubation, click-chemistry, or transfection[63, 73, 79, 80]. Hence, 116 clinical trials have been recorded according to ClinicalTrials.gov, whereas 50% were for biomarker studies, 33 were registered as EV-therapy, from which 22 studies use EVs derived from mesenchymal stem cells (September 2022)[71]. The remaining clinical studies were registered for drug delivery systems (6), vaccine studies (2), and basic EV analysis (17).

Nevertheless, EV research suffers from the enormous heterogenicity of particles with differences depending on harvest conditions, such as time point, stress status, and method which often results in long and complex purification processes limiting yield and scalability[63, 66, 71, 81]. Other critical challenges are, a lack of standardization, regulations, GMP compliant manufacturing, and unknown mechanisms making a translation of EV use in difficult[64, 71, 82-84]. Therefore, alternatives

have been studied as drug delivery and therapeutic systems trying to combine the advantages from EVs with the advantages from liposomes engineering EV-mimetics[84-86].

1.3. Engineered extracellular vesicles

To overcome drawbacks of EVs artificial EVs can be engineered. EV engineering can be separated into fully artificial EVs, based not on EV as starting material, and semi-synthetic EVs, where first EVs are isolated and then modified (**Figure 1.5.**). Methods of semi-synthetic EVs include surface modification of EVs through e.g., click-chemistry, cargo loading through e.g., electroporation and freeze/thawing, as well as fusion with liposomes to create an EV hybrid with changed the membrane properties, cargo, or membrane proteins[84, 87]. Those techniques have been used in various studies and showed to be able to improve various EV properties, such as circulation time, cargo delivery, therapeutic effect, and targeting ability[66, 88-90]. However, as EVs are used as starting material, semi-synthetic particles do not overcome the limitations of EVs and require general improvements in the EV field to become valid alternatives. Fully synthetic EVs can be created through top-down and bottom-up approaches. The bottom-up way creates complex structures by using simple creating blocks, such as lipids, nucleic acids, peptides, and proteins by using their physicochemical properties[91, 92].

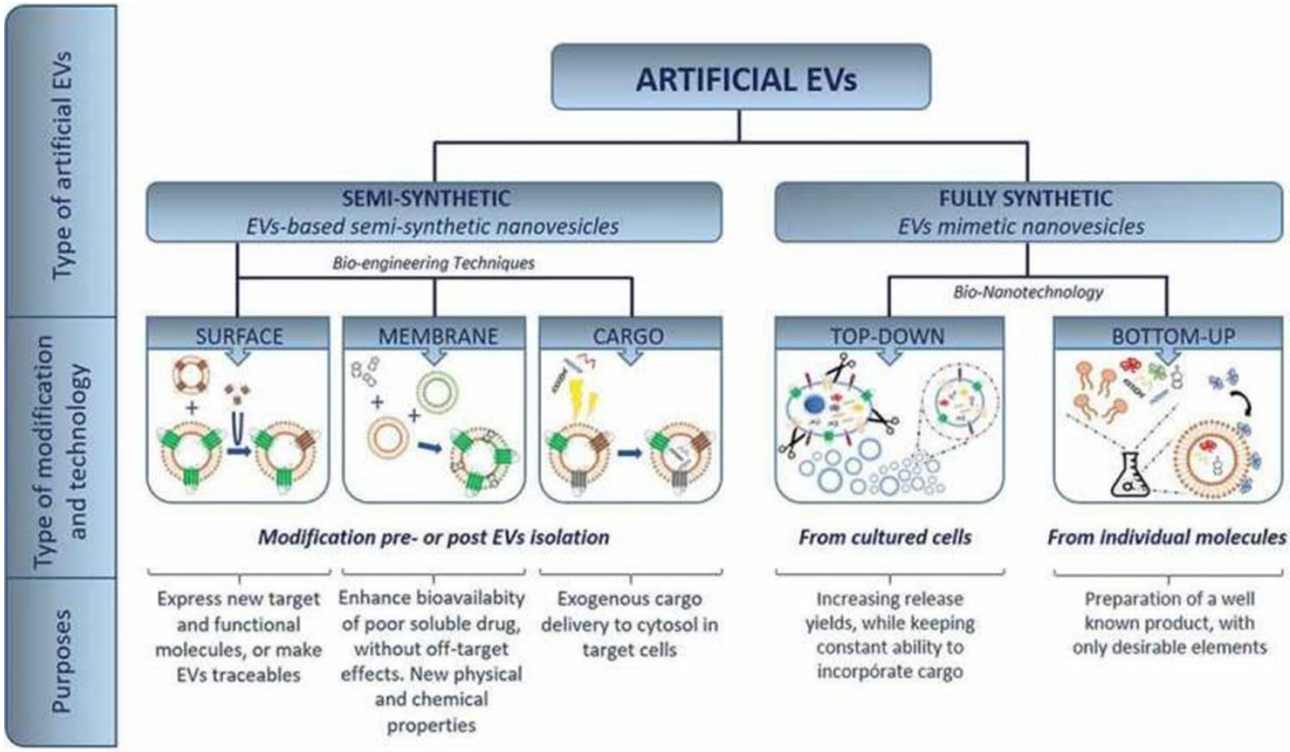

Figure 1.5. Artificial EV landscape.

Artificial EV creation can be separated in semi-synthetic engineering using EVs as starting material and fully synthetic engineering using different sources as starting material. Each method has its own advantages and disadvantages and serves a different purpose.

Image adapted from "Therapeutic biomaterials based on extracellular vesicles: classification of bio-engineering and mimetic preparation routes" (Pablo García-Manrique et al., 2018).

Therefore, usually liposomes are used as a promising starting point, as they can be easily produced to be unilamellar and nanosized. Liposomes can be formed with lipids that mimic the composition of exosomes and be modified post-formation. For example, T cell activation in an autoimmune disease could be downregulated by incorporation of certain ligands in a liposome or the targeting of tumor cells could be increased by conjugation of antibodies on the particle surface[93, 94]. However, even though those particles are usually scalable in production with high yields they also often exert an increased immunogenicity and further knowledge on EVs is needed to know exactly which features have to be engineered resulting in particles retaining positive EV

features. On the other hand, the top-down approach relies on breaking down bigger and more complex materials, such as cells, into nanosized vesicles. Vesicles are produced either by applying shear stress on the cell membrane, breaking it leading to spontaneous vesicle formation or through chemical stimulation with e.g., sulfhydryl blocking agents leading to vesicle formation by cell membrane blebbing[86, 95]. Those vesicles have been mainly used for drug delivery, but studies have shown their ability to enhance cell proliferation, enhance angiogenesis, modulate immune answers, reduce inflammation, enhance regenerative mechanisms, and enhance cellular uptake[88, 90, 96-101]. The most common top-down approach is formation of artificial EVs through serial extrusion over a polycarbonate membrane[84, 92]. Large-scale devices as well as GMP-compliant production has already been developed for extrusion-based artificial EV formation, whereas particle yields could be increased up to 250 times compared to natural EV production[90-92, 95]. The increased particle yield is probably due to the fact that through extrusion not only the plasma membrane breaks forming nano-sized particles, but also organelles, such as the mitochondria and the Golgi apparatus[90]. Resulting particles are usually smaller than 200 nm in diameter and show a proteomic profile which is much closer to the originating cell compared to natural EVs[102]. The EV proteosome is different from the cell proteosome due to the strict sorting during the formation in the endosomal system[56]. Even though top-down produced vesicles need similar purification techniques used for natural EVS, they show enhanced yield and scalability, better standardisation potential, and can be further improved through the same methods used for semi-synthetical EV production making it a very promising alternative to the usage of natural EVs.

1.4. Novel approach for intraperitoneal drug administration

The liver, as well as other organs, such as the spleen lay in the peritoneum, which is a cavity in the abdomen covered by thin membranes. Intraperitoneal injection (IP) offers an alternative route

to intravenous- or oral administration to target the liver with drugs. The advantages of IP are among others, the easy administration, the suitability for repetitive dosing, the high drug absorption, and the suitability for different formulations (drugs with different physiochemical properties)[103]. However, due to the very fast absorption of small molecules into the portal vein, the first pass effect of drug metabolism is almost as high as for orally administered drugs leading to a small active drug concentration in the systemic circulation. The fast clearance also hinders to have a high local drug concentration in the peritoneum. Still, progress has been made in the past years and IP has been more extensively used, especially for treatments of peritoneal metastasis, from cancers that have spread to the peritoneum from other organs after turning malignant (**Figure 1.6.**)[104].

However, for chronic liver diseases, IP-administered treatments are still underexploited[105]. So far, it has mostly been used to infuse hepatocytes to paediatric patients with acute liver failure[106, 107]. However, this successful and safe cell infusion paves the avenue for similar approaches to deliver small molecules for chronic liver disease or fibrotic events in the peritoneal space. A novel approach to deliver small drug molecules through the IP route is to use additive manufacturing for the formation of hydrogel depots which contain encapsulated small molecules. Due to their size, the hydrogels cannot be cleared from the peritoneum. Additionally, the sustained drug release reduces the dissolution rate of the drug, resulting in a higher drug concentration in the peritoneum and decreased uptake into the portal vein.

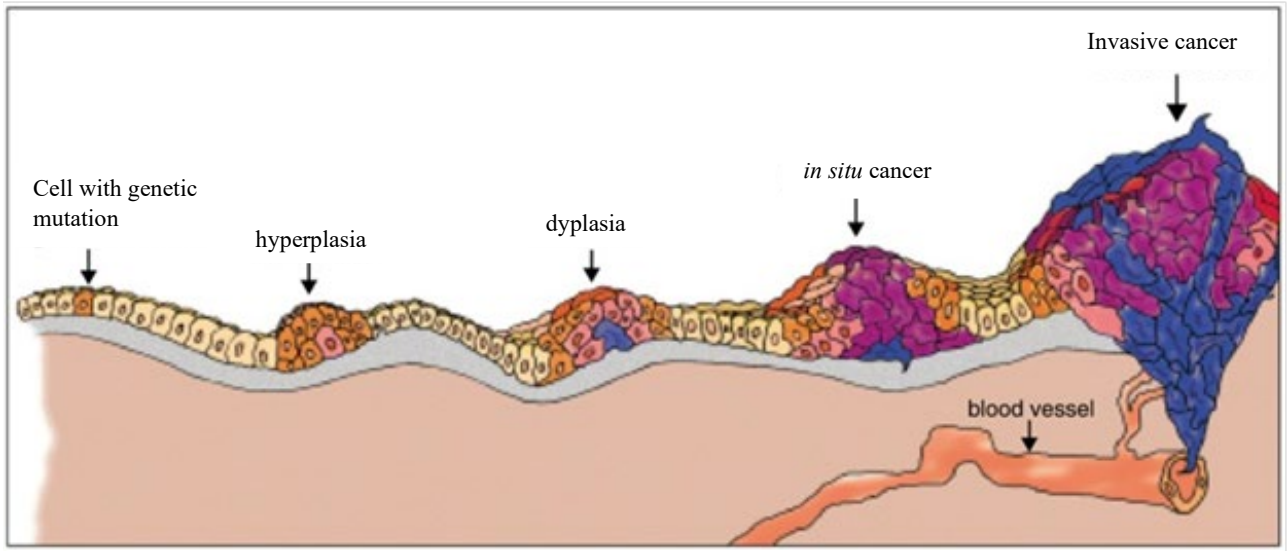

Figure 1.6. Formation of malignant tumors.

Tumor formation often starts with a genetic mutation that leads to sustained cell proliferation/growth, after a while of promoted cell growth a condition called hyperplasia is reached. If, after further mutations leading to the loss of differentiation and abnormal growth, the cells are still in their tissue of origin, they are called in situ cancer. However, if the tumor cells are shred into blood or lymph vessels (because of additional mutations) to invade other tissues and form new metastases the tumor is said to be malignant. Cancer spreading from peritoneal organs, such as the gastrointestinal track, lead to the formation of peritoneal metastasis.

Source: National Institutes of Health (US); Biological Sciences Curriculum Study. NIH Curriculum Supplement Series [Internet]. Bethesda (MD): National Institutes of Health (US); 2007. Understanding Cancer. Available from: https://www.ncbi.nlm.nih.gov/books/NBK20362/

1.5. Scope of the thesis

The increasing prevalence of fibrosis and the lack of specific treatments calls for novel anti-fibrotic therapeutics. We set out to establish a protocol for the formation and purification of artificial EVs, termed cell-derived nanovesicles (cdNVs) from differently pre-treated HSCs, with fibrosis-resolving properties. We have previously shown the release of EVs with different compositions and activities, depending on the HSC cell status, and their fibrosis-resolving properties[108]. However, due to limitations in EV usage they are not suitable as anti-fibrotic therapeutics. We sought to overcome those drawbacks by creating cdNVs, while preserving the

HSC fibrosis resolution potential of EVs, to create potential bioderived therapeutics for chronic liver diseases.

In **Chapter 2** different cdNV formation methods were tested to establish an upstream process starting from quiescent, naïve and TGF-β_1 activated LX-2 cells. Therefore, several methods were evaluated based on their lysis efficiency, as well as on the quality (size, PDI, yield) of the formed cdNVs. Additionally, fluorescent microscopy experiments were performed to assess the ability of the formed cdNVs to induce a phenotypical shift of cdNV-treated activated LX-2 cells into a quiescent-like state.

Building upon the previous chapter, in **Chapter 3** we established methodological practices for the purification, enrichment, and sterilization of cdNVs derived from differently pre-treated LX-2 cells. Additionally, soluble factors were collected during the downstream process acting as a control to investigate activity loss and activity specificity.

Chapter 4 covers all the activity studies performed on LX-2 cells treated with cdNVs formed through the established upstream and downstream processes. Genotypical and phenotypical deactivation in naïve, as well as TGF-β_1 activated LX-2 cells upon cdNV treatment was assessed via fluorescent microscopy and real-time polymerase chain reaction (qPCR) on several markers involved in HSC activation. Surface corona and lipids were investigated for their role in cell deactivation. Further, homing of cdNVs was studied and compared between naïve and TGF-β_1 activated LX-2 cells via flow cytometry.

We believe that our work lays the foundation for LX-2 cdNVs, which confirmed to be a promising candidate for the development of anti-fibrotic therapies.

In **Chapter 5**, we describe a novel approach that employs additive manufacturing to develop bioorthogonal and biodegradable hydrogel microbeads. These microbeads can be loaded with various liposomal formulations, creating a platform that enables sustained release of multiple small drug candidates. These drug candidates, both hydrophilic and hydrophobic, are encapsulated in different liposomal formulations leading to a sustained release in the peritoneum. As proof-of-concept gefitinib was used, which is a small hydrophobic drug against peritoneal adhesion, as well as tumours epidermal growth factor receptor mutations.

Chapter 2.

Establishment of an upstream process for the formation of cell-derived nanovesicles from LX-2 cells

2.1. Abstract

Cell-derived nanovesicles (cdNVs) have become an increasingly popular research topic in recent years[90, 95, 96, 99-101, 109, 110]. There are several methods that have been tested for the formation of cdNVs, including serial extrusion, freeze/thawing, and sonication. However, serial extrusion has been shown to be the most effective method for producing quality cdNVs. In this process, cells are forced through membranes with decreasing pore sizes resulting in membrane rupture and formation of small vesicles. In order to maximize the benefits of serial extrusion, the process was optimized by conducting 5 extrusions through 10 μm, 5 through 5 μm, and 5 through 1 μm pore diameters. Freeze/thawing and sonication prior to extrusion resulted in some improvement, but concerns about the harshness and potential damage to biological active components of cdNVs led to the implementation of the optimized serial extrusion method. The results demonstrate that this method is a simple and effective way to produce high-quality cdNVs for therapeutic applications.

2.2. Introduction

The formation of uniform and nano-sized particles is crucial as, by having a homogenous particle size distribution, it becomes possible to predict and control the properties and behaviour of the final product. Therefore, a good technique for a consistent formation of these particles out of cells is needed. The used LX-2 cells for cell-derived nanovesicles (cdNVs) formation were grown and expanded in 2D cell culture with flasks having a surface of 175 cm^2. The aim of this study was to determine the optimal technique for the formation of nano-sized, anti-fibrotic, and uniform cdNVs. In this chapter, the efficiency and suitability of different cell lysis methods, including sonication, freeze/thawing, serial extrusion, and lysis by a BioVortexer, to produce uniform and biologically active cdNVs were compared.

Sonication is a process in which cells are exposed to high-frequency sound waves that cause mechanical stress, leading to the breakage of the cell membrane and release of intracellular components[111]. The sound waves cause the liquid to cavitate, or form small bubbles, which can then implode and cause pressure leading to lysis of the cells[112]. This cell lysis type is often performed using a sonicator with a microtip that can directly be inserted into the sample with the resuspended cells. As this kind of lysis generates plenty of heat, the lysis is typically performed on ice, with breaks in between impulses, allowing the sample to cool down

Freeze/thawing cell lysis is another method that involves alternately freezing and thawing a cell suspension[111]. The mechanical stress occurring due to the rapid expansion and contraction of ice crystals during freezing and thawing of the sample weakens the cell membrane and causes it to break[113]. This type of cell lysis is often performed by rapidly freezing the cell suspension in liquid nitrogen or a dry ice/ethanol bath, and then thawing it in a water bath. The process is repeated several times to ensure complete cell lysis. Both sonication and freeze/thawing have been used in the production of cell-derived nanovesicles by other research groups.

Serial extrusion and the BioVortexer (BV) from Bio spec are two additional methods for cell lysis and potential nanovesicle formation. Serial extrusion, a frequently cited technique for cell-derived vesicle formation[90, 99, 101, 110], involves forcing cells through membranes with decreasing pore sizes. This creates friction on the cells, causing the membrane to break and spontaneously form vesicles which encapsulate intracellular components The BV, on the other hand, uses high-speed, vortex-like motions to generate friction on cells, leading to cell lysis. Both serial extrusion and the BV can potentially be used in combination with sonication and freeze/thawing to boost the production of cdNVs, depending on the specific requirements of the experiment. Each method has

its own advantages and disadvantages, and the choice of cell lysis method will depend on the quality and yield of the produced cdNVs.

2.3. Material and Methods

2.3.1. Cell culture

LX-2 cells were grown at 37 °C in a humidified atmosphere containing 5% CO_2 in high glucose (4.5 g/L) DMEM (Carl Roth, Germany) supplemented with 10'000 units/L of penicillin and streptomycin (P/S, Gibco), 200 mM L-Glutamine (Sigma, USA), and 2% (v/v) of sterile filtered (0.2 µm, cellulose acetate membrane) fetal bovine serum (FBS; Merck Millipore, USA). Cells were cultivated in T175 flasks (Sarstedt, Germany) and 24 h prior to harvest were treated in serum-free DMEM either with 10 µM retinol (Merck Millipore, USA) and 300 µM palmitic acid (Merck Millipore, USA) (RolPA), 10 ng/mL TGF-β_1 (BioVendor, USA), or 5 mM S80 liposomes. Cells were detached with 2 mL Accutase (Merck Millipore, USA) per flask and 4 min incubation at 37 °C.

2.3.2. cdNV formation

The LX-2 cells were washed with pre-heated (37 °C) PBS (Carl Roth, Germany) and detached as described above. The total cell amount was counted by mixing a small aliquot 1:1 with trypan blue (ThermoFisher, USA) and using a 0.100 mm Neubauer chamber (Hecht Assistant, Germany). The LX-2 cells were then washed by pelleting for 3 min at 500 g. The pellet was resuspended to reach a desired conc. between 1 – 10 x 10^6 LX-2/mL in PBS for all formation experiments.

2.3.2.1. Formation through extrusion

Two different extruders were used for the formation. The first was the Mini-Extruder (Avanti Polar Lipids, USA), where pressure was built by manually pushing a syringe, and the second was

the LIPEX extruder (Evonik, Canada), where pressure was generated using an external nitrogen gas source. The extruders were assembled with polycarbonate membranes (Sterlitech) with various pore diameters (10 μm, 5 μm, 1 μm) as per the manufacturer's instructions. The resuspended LX-2 cells were serially extruded through the 10 μM, 5 μM and 1 μM polycarbonate membrane. The formed cdNVs were stored on ice upon further use.

2.3.2.2. Formation by BioVortexer

Cell lysis was performed using a BioVortexer and Spiral Pestle Grinder (Bio spec, USA) following the manufacturer's instructions. Briefly, the cells were pelleted in a 1.5- or 2.0-mL reaction tube by low spin centrifugation (500 g, 5 min) and lysed with or without the addition of glass grinding beads (0.05 cc) by rotating the spiral pestle on the pellet at 9’000 rpm for 30 sec. The process was repeated a total of 2 times.

2.3.2.3. Formation through sonication

The LX-2 cells were lysed on ice using a tip sonicator by sonicating for 5 s with a peak-to-peak amplitude of 10 microns (22 drive, 0 auto), followed by a 10-second break. The sonication cycle was repeated five times.

2.3.2.4. Formation through freeze/thawing

The LX-2 cells were frozen in liquid nitrogen for 1 min and were thawed by immersing them in a 37 °C water bath. This process was repeated up to 3 times.

2.3.3. Particle characterization

The size distribution, yield, and zeta potential of cdNVs were determined using nanoparticle tracking analysis (NTA, ZetaView 8.05.05 SP2, Particle Metrix, Germany; Sensitivity: 70.0; Shutter: 100) after diluting the sample with filtered MilliQ water. The size distribution of particles

formed by different lysis techniques was compared using dynamic light scattering (DLS; Anton Paar, Austria) by measuring particles diluted in filtered PBS. The protein content was measured using a micro-BCA protein assay kit (ThermoFisher, USA) following the manufacturer's instructions.

2.3.4. Screening of cdNV Activity on LX-2 cells

The cell viability and formation of lipid droplets were checked by treating naïve LX-2 cells with the particles to verify if they carried anti-fibrotic potential. A colorimetric assay was used to measure cell viability, and microscopy was used to examine the formation of lipid droplets.

2.3.4.1. Quantitation of viable cell number in cytotoxicity assays

LX-2 cells were seeded in a 96-well plate (Faust, Switzerland) at a density of 10'000 cells per well. The cell viability was determined using the CCK-8 assay (Merck Millipore, USA) according to the manufacturer's instructions. After treatment with PBS, the cells were washed and 90 µL of FBS-free medium and 10 µL of CCK-8 solution were added to each well. The plate was further incubated at 37 °C and 5% CO2 for 2 h. The absorbance at 450 nm (reference at 650 nm) was measured using a plate reader (Infinite MNano; Tecan, Switzerland). The cell viability was calculated using the following equation:

$$cell\ viability\ [\%] = \frac{OD_{treatment}}{OD_{DMEM}} * 100$$

where "OD treatment" refers to the optical density of the LX-2 cells treated with the specific treatment and "OD DMEM" refers to the optical density of LX-2 cells treated with the vehicle (FBS-free DMEM).

2.3.4.2 Lipid droplet content analysis

The lipid droplet analysis was performed as described before with slight adjustments[45] Briefly, 30'000 LX-2 cells were seeded in a 48-well plate (Faust, Switzerland) and treated with different treatment. Then cells were washed and fixed with 200 µL/well Roti®-Histofix 4% (Carl Roth, Germany) for 10 min at RT, and washed once with 1 mL/well deionized MilliQ water. LX-2 cells were stained with 200 µL/well of a filtered (0.45 µm, PVDF; Merck Millipore, USA) Oil Red O (ORO, 0.5% w/v; Merck Millipore, USA) solution in propylene glycol for 15 min at RT. The remaining ORO was removed and cells were washed twice with PBS. Nuclei were counterstained with 200 µL/well of a 4 µM DAPI solution (ThermoFisher, USA) in PBS for 5 min at RT. Afterwards, cells were rinsed with PBS and phase contrast (bright field, BF) acquired as well as fluorescent images using an inverted Nikon Ti-U microscope (Nikon Instruments, Japan) equipped with a Plan Fluor DL WD 15.2 10x, with a numerical aperture of 0.3 (Nikon Instruments, Japan), DAPI filter (ex 360, em 460, 100 ms exposure) and Texas Red filter (ex 560, em 645, 300 ms exposure).

The fluorescent binary area and the cell count were analysed using a script with the open-source FIJI software (detailed information can be found in the Appendix). The fluorescent binary area was then divided by the cell count to obtain the lipid droplets area [μm^2] per LX-2 cell.

2.4. Results

2.4.1. Formation of cdNVs through serial extrusion

Serial extrusion of cells is the most commonly cited technique to form cdNVs, whereas commercial extruders[99, 109, 110] and home-made extruders using either manual force, external gas pressure, peristaltic pumps[90] or centrifugation[95, 100] are used. Commonly, a combination of serial extrusion through membranes with pore diameters of 10 µm, 5 µm, and 1 µm are used to form

cdNVs from mammalian cells[95, 100, 102, 109, 110]. Hence, the same membrane pores were used, whereas either one or five extrusions through the membranes with the same pore size were tried and characterized the formed vesicles by their size distribution, mean diameter, polydispersity index (PDI), particle yield, and protein amount. Already after one extrusion through a membrane with 10 µm pores cdNVs with a mean diameter between 170 – 200 nm were obtained (**Figure 2.1a**). Increasing the extrusion cycles to five times did not change the mean diameter but led to a slightly narrower size distribution, visualized by a smaller PDI with a smaller SD (**Figure 2.1a/b)**. Further extrusion through 5 µm and 1 µm pores did not alter the mean diameter but led to smaller PDIs till one extrusion through the 1 µm pore. Increasing the extrusion cycles through the 1 µm pore did not lower the PDI. Five extrusions through the 10 µm pores increased the particle yield ~4x compared to only one extrusion (**Figure 2.1c**). The additional extrusion through the 5 µm and 1 µm pores did not change the particle yield. However, the more extrusion cycles and the smaller the pore size of the membrane, the lower the resulting protein amount in the cdNV sample was (**Figure 2.1d**) and therefore the lower the protein-to-particle ratio became. Hence, additional extrusion cycles do not lead to more particles, but to a purification of the sample, probably due to unspecific protein absorption on the polycarbonate membrane.

The particle yield after extrusion could be increased by increasing the LX-2 cell concentration in the pre-extrusion sample (**Figure A2.1a**). However, since a higher cell concentration means more cells are forced through the pores at the same time, a higher pressure was needed for extrusion, making the mini-extruder very hard to use for cell concentrations above 5.0 x 10^6 LX-2/mL. The high cell concentration did lead to clogging of the membrane and high back pressure, which led to leaking and a total sample loss of 40% (mass) after full extrusion (**Figure A2.1b**). Even though cdNVs could be formed just by serial extrusion, explored different methods to see if

the cdNV formation process could be improved. As lysis calculations based on weight are very imprecise due to the sample loss during extrusion, the protein concentration in the collected supernatant after pelleting unlysed cells and aggregates was used to compare cell lysis.

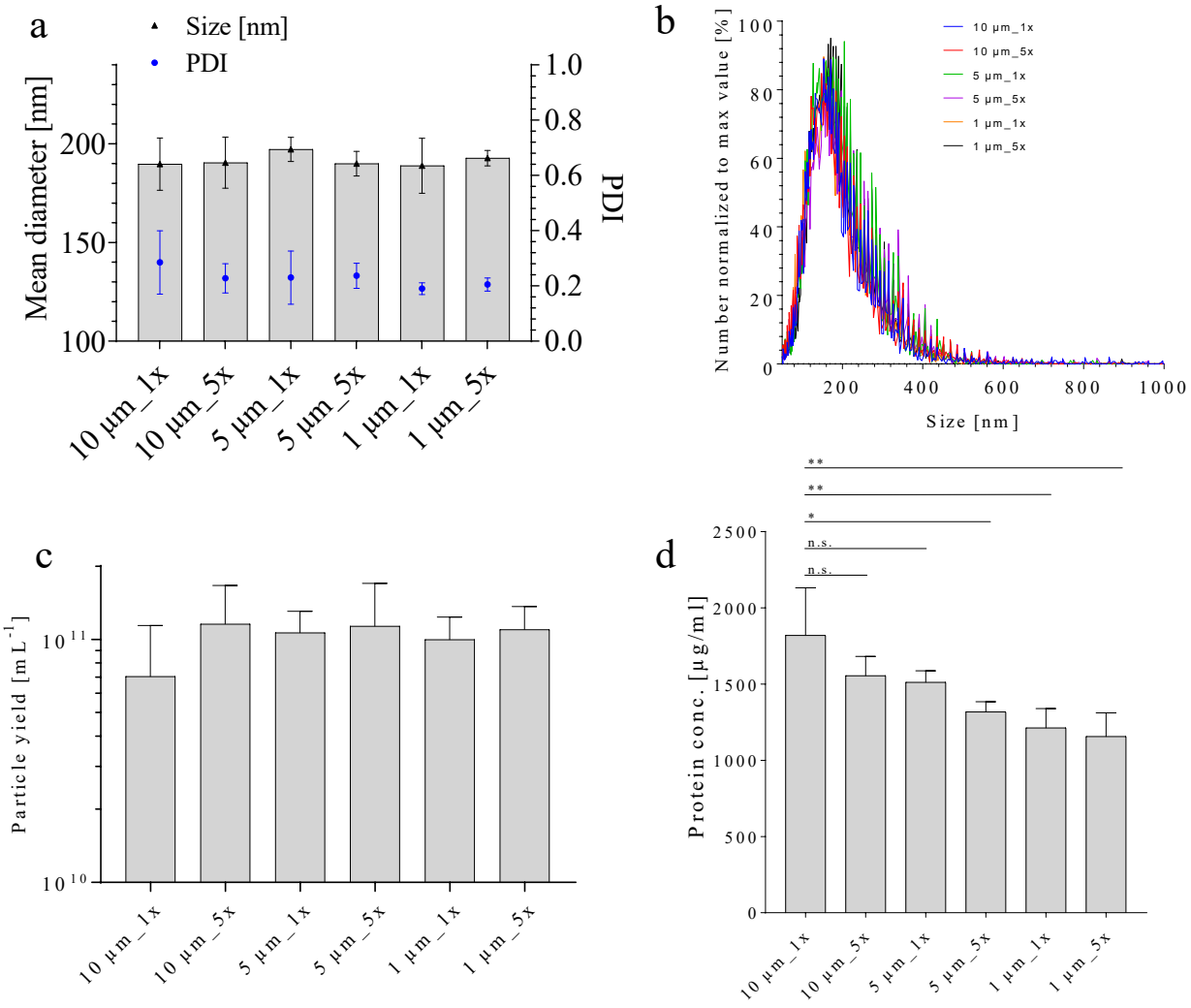

Figure 2.1. Physicochemical characterization of cell-derived nanovesicles (cdNVs) formed through serial extrusion.

a, Mean diameter and PDI of freshly formed cdNVs at different points through serial extrusion of untreated LX-2 cells (mean ± SD, n = 3). **b,** Size distribution profile of freshly formed cdNVs at different points through serial extrusion of untreated LX-2 cells at a concentration of 5.0 x 10^6 cells/mL (mean ± SD, n ≥ 3). **c,** Particle yield per mL of freshly formed cdNVs at different points through serial extrusion of untreated LX-2 cells (mean ± SD, n ≥ 3). **d,** Protein concentration of freshly formed cdNV solutions at different points through serial extrusion of untreated LX-2 cells (mean ± SD, n ≥ 3) (Ordinary one-way ANOVA; * represents p-value > 0.05; ** represents p-value > 0.01)

2.4.2. Formation of cdNVs by the BioVortexer

The BV is designed to homogenize pellets by rotating a spiral pestle with 9'000 rpm. In addition, with glass grinding beads (GGB) lysis of soft tissue should be completed in seconds. The lysis of the BV with and without GGB was tested by pelleting the LX-2 cells and applying the BV for 30 s, before repeating the procedure two additional times. After lysis, a low-speed centrifugation (500 g, 5 min) was performed on each sample and the supernatant (sn) was collected to measure its particle content. Since the cells dye over time and produce apoptotic bodies with a size range of 50 to 5000 nm[114] a control sample was added where no lysis was performed. The protein concentration, as well as size distribution measured by DLS, in the sn of BV, BV + GGB (BVG), and control sample were compared. The protein concentration in the sn of BV and BVG was higher than the one measured in the control sample, with BVG leading to the highest protein concentration (**Figure 2.2a**). However, the protein concentration in BVG was only roughly 50% of what was reached with extrusion, hinting at worse lysis. The formed cdNVs were very heterogenous and showed particles bigger than 500 nm. This bigger population was also discovered in the no-lysis control, therefore it cannot be excluded that those are apoptotic bodies (**Figure 2.2b**). Even though the BV is simpler and quicker compared to the extruder, the produced cdNVs are of insufficient quality to proceed. Nevertheless, a combination of BVG with 10 µm extrusion (5 times) was tested to see if the cdNV production can be improved by lowering sample loss and increasing particle yield. BVG prior extrusion did not change the cdNV size distribution, as the extrusion itself is the reason for the homogenous distribution (**Figure 2.2c**). During the lysis with BVG a small sample amount is lost, this is because the added glass beads must be removed after BVG lysis before continuing with extrusion. The removal of BVG was performed by letting the GGB sediment and collecting the sn which resulted in leaving ~35% sample back. Therefore, the overall sample loss

was barely decreased in BVG + extrusion compared to extrusion alone, even though the extrusion itself led to ~60% less sample loss after BVG (**Figure 2.2d**). The particle yield after BVG + 10 µm extrusion was smaller than extrusion alone which could be due to absorption of cdNVs on

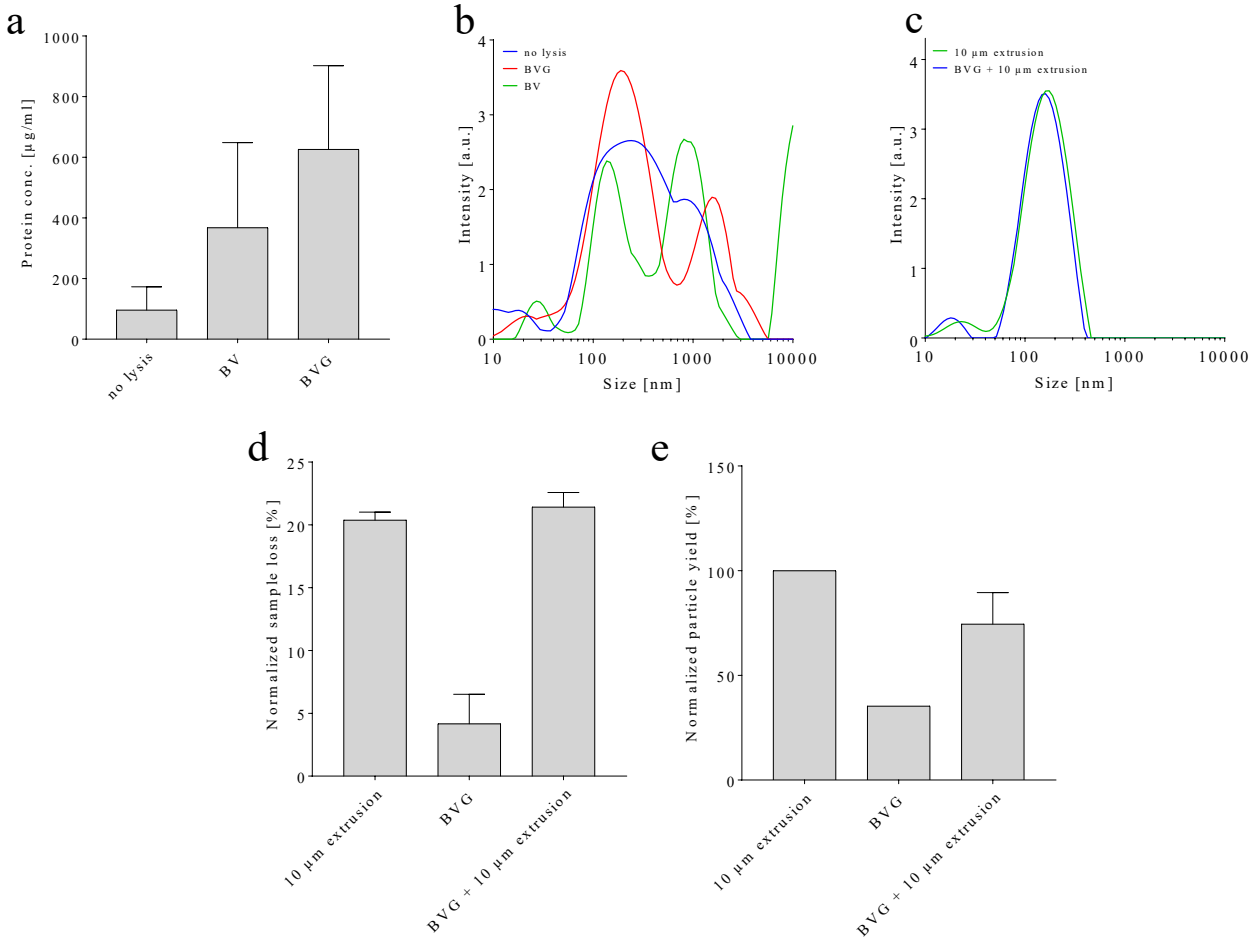

Figure 2.2. Physicochemical characterization of cell-derived nanovesicles (cdNVs) formed by the BioVortexer.

a, Protein concentration of freshly formed cdNVs solutions by the BioVortexer with and without glass (BVG/BV) beads of untreated LX-2 cells compared to a non lysed control sample (mean ± SD, n = 2). **b,** Size distribution profile of freshly formed cdNVs by BV and BVG of untreated LX-2 cells compared to a non lysed control sample. **c,** Size distribution profile of freshly formed cdNVs obtained through five extrusion cycles using a 10 µm pore membrane (10 µm extrusion), with and without pre-lysis by BVG of untreated LX-2 cells. **d,** Sample weight loss during lysis through 10 µm extrusion, BVG and combination normalized to the starting weight of the non-lysed sample (mean ± SD, n = 2). **e,** Particle yield of freshly formed cdNVs obtained through 10 µm extrusion, BVG and combination normalized to yield obtained after 10 µm extrusion (mean, n = 1-2).

glass beads (**Figure 2.2e**). Overall, the BVG did not improve the yield, nor the quality of the formed particles and therefore it was not considered for further usage.

2.4.3. Formation of cdNVs through sonication

Sonication creates high-frequency soundwaves, which lyses cells by disrupting the cell membrane. LX-2 cells were resuspended in PBS and lysed with a tip sonicator by exposing them to several pulses of sound waves for the formation of cdNVs. The sn of sonicated cells was compared with the sn of 5x extruded (10 μm) LX-2 cells and analysed on their particle and protein content after low spin centrifugation to remove debris. Sonication increased the protein amount in the sn by 25% compared to 10 μm extrusion (**Figure 2.3a**) which hints at improved lysis. The protein concentration decreased slightly after extrusion due to proteins that got stuck on the polycarbonate membrane. The suspected lysis improvement by sonication was confirmed by a higher particle amount in the sn compared to extrusion only (**Figure 2.3b**). The particle yield was further increased by approximately 20% when sonication and extrusion were combined. However, upon sonication, the resulting cdNV population was very dispersed and contained micro-sized particles (**Figure 2.3c**). Extrusion removed the micro-sized particle population and narrowed the cdNV particle population which had a similar distribution to the cdNVs formed by only 10 μm extrusion The loss of samples during sonication is minimal, as the only instance of sample loss occurs through adherence of solution to the sonication tip. Even though cell lysis was improved by sonication, no improvement in the extrusion process was observed as the same sample loss was still the same (**Figure 2.3d**). Hence, regardless of the slight increase in particle yield that was observed upon sonication, decided to not continue with this method, as the particles were more polydisperse and no improvement of the following extrusion was observed.

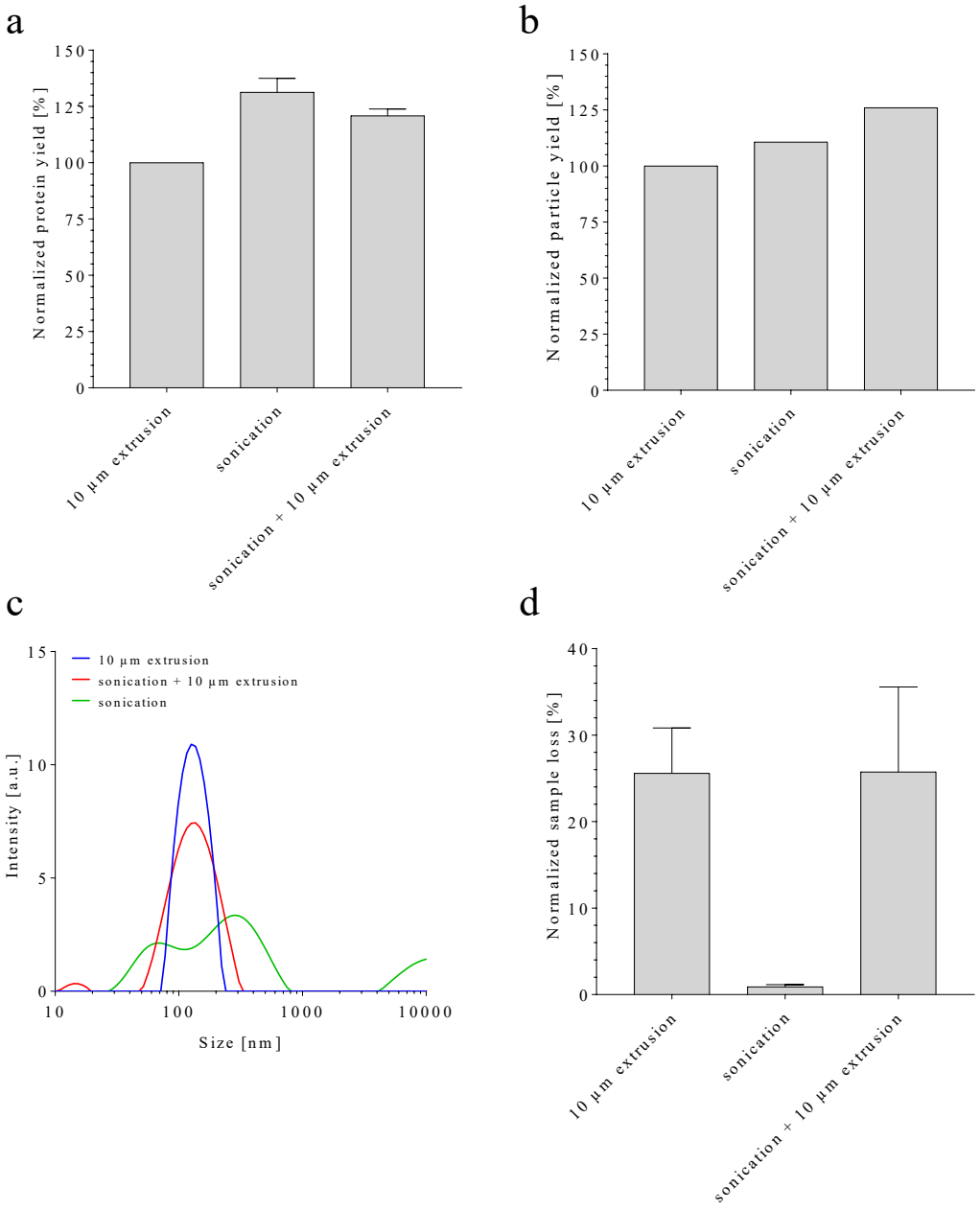

Figure 2.3. Physicochemical characterization of cell-derived nanovesicles (cdNVs) formed by sonication.

a, Protein concentration of freshly formed cdNVs formed from untreated LX-2 cells through five extrusion cycles using a 10 µm pore membrane (10 µm extrusion), sonication, and combination normalized to protein concentration after 10 µm extrusion (mean ± SD, n = 2). **b,** Particle yield of freshly formed cdNVs obtained through 10 µm extrusion, sonication, and combination normalized to yield obtained after 10 µm extrusion (mean, n = 1-2). **c,** Size distribution profile of freshly formed cdNVs obtained through 10 µm extrusion, sonication, and combination. **d,** Sample weight loss during lysis through 10 µm extrusion, sonication, and combination normalized to yield obtained after 10 µm extrusion (mean ± SD, n = 2).

2.4.4. Formation of cdNVs through freeze/thawing

Freezing of cells causes ice formation on the cell membrane which leads to break down of the plasma membrane upon thawing. The process was not repeated more than three times, as it can destroy/desaturate cellular components which are sensitive to temperature, such as most proteins. Same as for sonication and BVG, freeze/thawing (F/T) was tested alone and in combination with 10 µm extrusion. After cell lysis, the sn was collected by low-spin centrifugation and the sample was characterized by its particle and protein content. The protein concentration in the sn upon lysis was increased for F/T compared to 10 µm extrusion hinting at improved lysis (**Figure 2.4a**). Extrusion after F/T decreased the protein concentration slightly which is, as described above, due to unspecific protein adherence on the polycarbonate membrane. Indeed, the particle amount was increased by 10% after F/T compared to 10 µm extrusion only (**Figure 2.4b**). Extrusion of F/T lysed LX-2 cells did not improve the particle yield. The particles resulting from F/T cell lysis were very polydisperse and contained a micro-sized particle population which was not what we were aiming for (**Figure 2.4c**). Extrusion upon F/T narrowed the particle size distribution and led to cdNVs with a slightly smaller diameter compared to cdNVs formed through 10 µm extrusion only. As F/T was performed by freezing a cell suspension in a closed reaction tube by immersing it in liquid nitrogen and thawing the suspension still in the closed reaction tube in a 37 °C water bath, no sample gets lost during the procedure. The loss of sample during extrusion could be slightly decreased if three F/T cycles were added prior 10 µm extrusion (**Figure 2.4d**). Nevertheless, also here, the benefits of F/T were too small to add it routinely prior extrusion for cdNV formation.

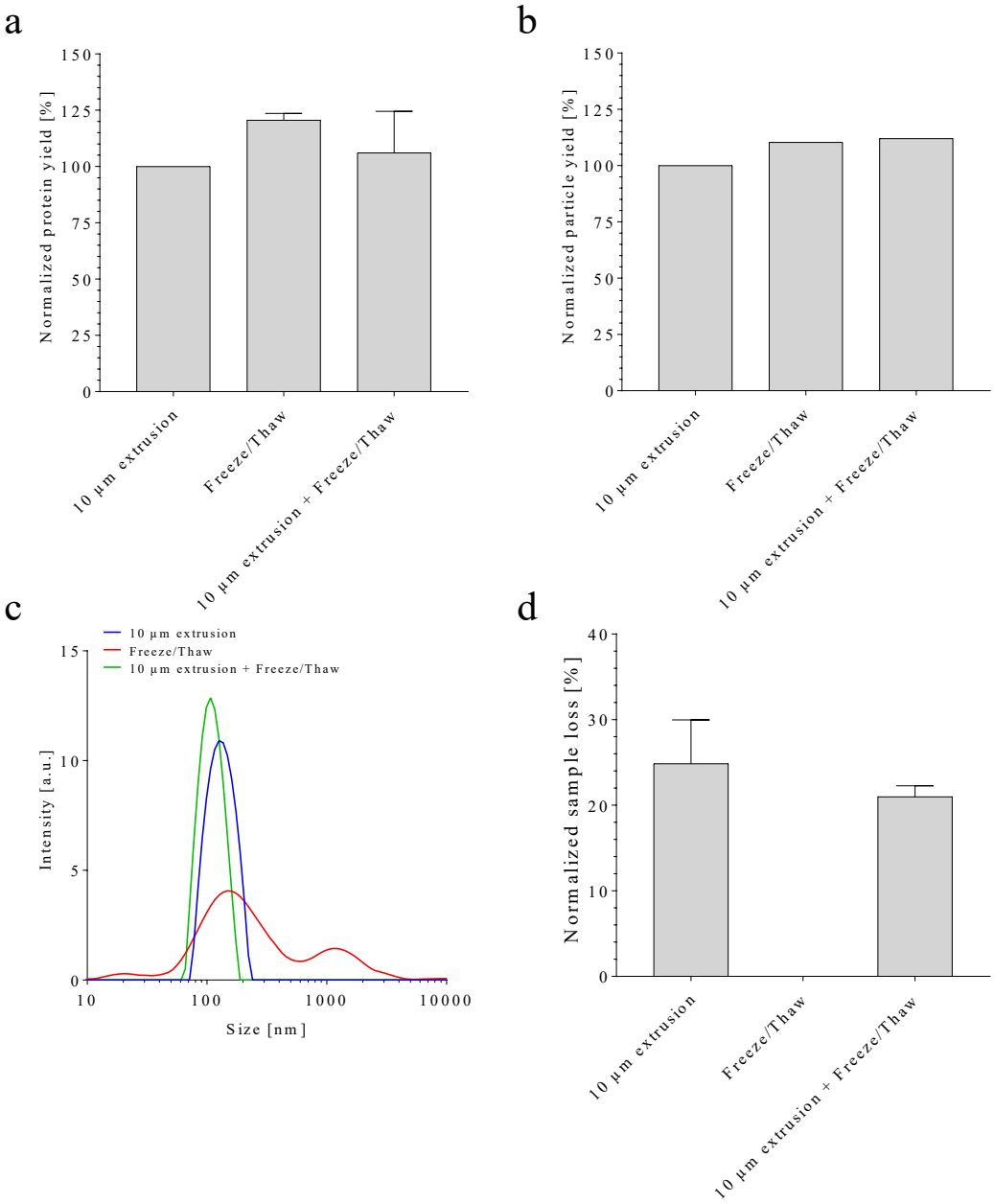

Figure 2.4. Physicochemical characterization of cell-derived nanovesicles (cdNVs) formed by freeze/thawing.

a, Protein concentration of freshly formed cdNVs formed from untreated LX-2 cells through five extrusion cycles using a 10 µm pore membrane (10 µm extrusion), freeze/thawing (F/T), and combination normalized to protein concentration after 10 µm extrusion (mean ± SD, n = 2). **b,** Particle yield of freshly formed cdNVs obtained through 10 µm extrusion, F/T, and combination normalized to yield obtained after 10 µm extrusion (mean, n = 1-2). **c,** Size distribution profile of freshly formed cdNVs obtained through 10 µm extrusion, F/T, and combination. **d,** Sample weight loss during lysis through 10 µm extrusion, F/T, and combination normalized to yield obtained after 10 µm extrusion (mean ± SD, n = 2).

2.4.5. Effect of cdNVs formed through serial extrusion on the viability and lipid droplet content in naïve LX-2 cells

In the initial stages of cdNV formation, the primary goal should not be focused only on achieving the highest yield possible. It is even more important to assess whether the resulting cdNVs exhibit an anti-fibrotic effect upon their administration to naïve LX-2 cells. Lipid droplets can be used to determine the phenotype of LX-2 cells[45, 54, 108]. They are present in a quiescent state, such as after treatment with retinol supplemented with palmitic acid, the gold standard for in vitro fibrosis resolution, and absent in naïve or activated LX-2 cells. Lipid droplets can be stained with Oil Red O (ORO) and appear as red spots in fluorescent images (ORO FL) or as brown spots in bright field images (ORO BF) under a fluorescent microscope. Although no purification or sterilization method has been established, a preliminary activity test was performed by comparing the effect of cdNVs formed from DMEM-, RolPA-, and S80-treated LX-2 cells by serial extrusion on naïve LX-2 cells. After cdNV formation, low spin centrifugation was performed to eliminate remaining cell debris, potential aggregates, and nuclei. The particle concentration of the cdNV samples was normalized to 4.0×10^{11} particles/mL (A) prior to administration, and, additionally, testing was performed using 10x (B) and 20x (C) dilutions (2.0×10^{10} particles/mL (B); 1.0×10^{10} particles/mL (C)). The cdNV concentration A and B had no impact on cell metabolism, but the concentration C resulted in decreased cell viability, especially when using cdNV_S80 (**Figure 2.5a**). Microscopy images demonstrated that naïve cells treated with cdNVs generated lipid droplets in a concentration-dependent manner, suggesting transdifferentiation into a quiescent-like state (**Figure 2.5b**). The semi-quantification of lipid droplets was performed by normalizing the area of lipid droplets to the number of cells, and all cdNVs tested resulted in lipid droplet formation in naïve LX-2 cells (**Figure 2.5c**). Furthermore, high cdNV concentrations resulted in more lipid

droplets than direct RolPA treatment. Additional experiments were conducted with cdNV_S80 to investigate the correlation between particle concentration and lipid droplet formation. A linear regression analysis of the ORO FRI of four different replicates against the particle concentration yielded an R square value of 0.5828, indicating a moderate correlation[115] (**Figure 2.5d**). Although the addition of more particles is expected to lead to more lipid droplets, as more lipids are delivered to the cells, the particles must be purified to truly evaluate the anti-fibrotic potential of cdNVs and obtain more reproducible data.

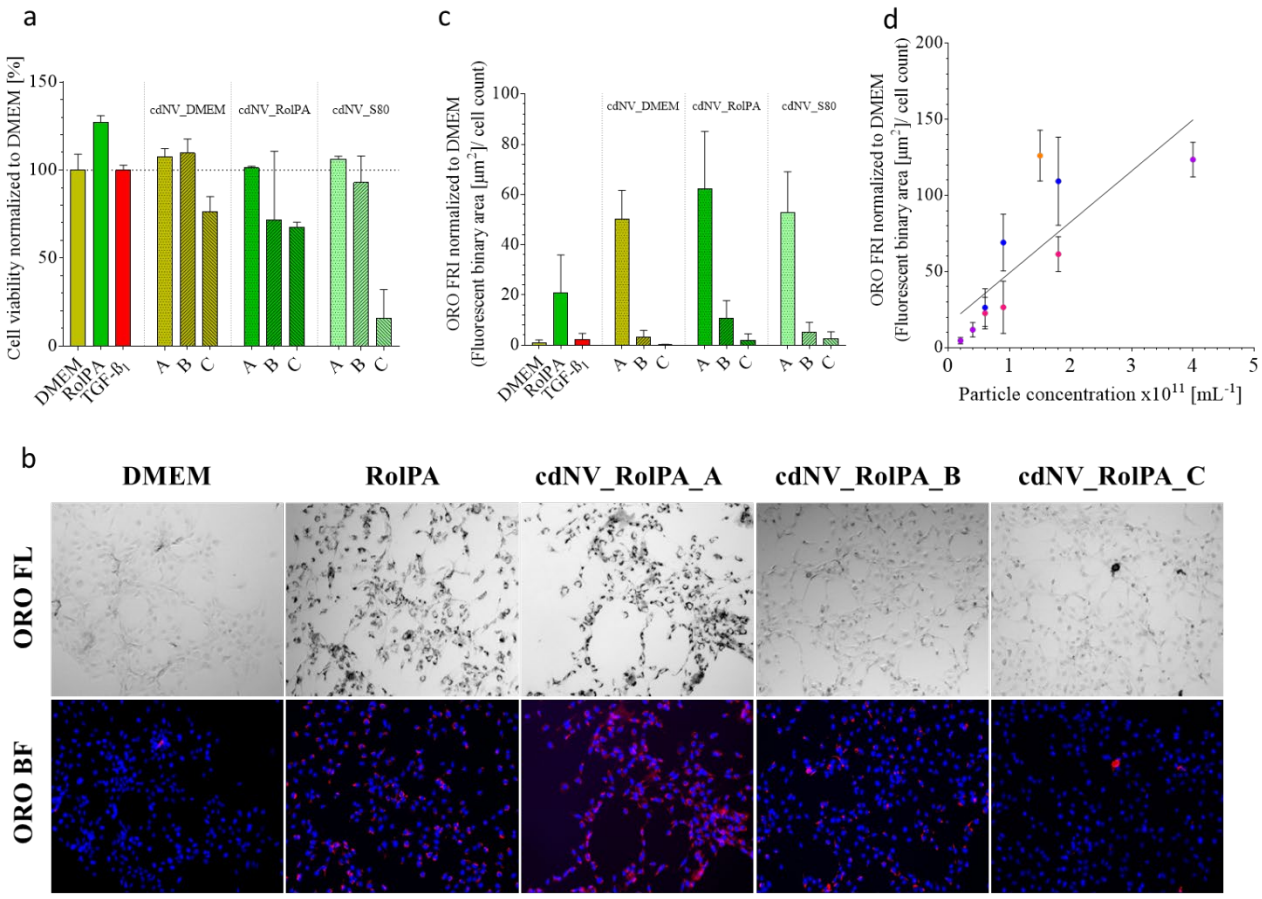

Figure 2.5. Activity of cell-derived nanovesicles (cdNVs) on naïve LX-2 cells.

a, Cell viability of naive LX-2 cells treated with three different cell-derived nanovesicles (cdNVs) concentrations (A = 4.0 x 10^{11} cdNVs/mL; B = 4.0 x 10^{10} cdNVs/mL; C = 2.0 x 10^{10} cdNVs/mL) derived from DMEM, RolPA, or S80 treated LX-2 cells (mean ± SD, N = 6, n = 1). **b,** Representative 10x microscopy images of lipid droplets stained with Oil red O (ORO) in differently treated naïve LX-2 cells. Lipid droplets in fluorescence (ORO FL) show in red (nuclei counterstained with DAPI (blue)) and in bright field (ORO BF) show in brown. **c,** Graph showing the ORO fluorescence normalized to the cell count in the DAPI field (FRI) and normalized to the ORO FRI of DMEM (mean ± SD, N = 6, n = 1). **d,** Correlation between the concentration of cdNV_S80 and the quantity of lipid droplets per cell following administration to naive LX-2 cells (mean ± SD, N (technical replicate) = 24, n (biological replicate) = 4). Each colour represents one replicate (linear regression, R square 0.5828).

2.5. Discussion and conclusion

In this study, several methods were evaluated for the upstream process of forming cell-derived nanovesicles (cdNVs) from LX-2 cells: sonication, freeze/thawing, serial extrusion, and by lysis through the BV. Extrusion was found to be the most efficient and effective method, producing cdNVs with a mean diameter of 170-200 nm already after one extrusion through a 10 µm pore. Increasing the number of extrusion cycles and decreasing the pore size purified the sample but did not increase the number of particles. The particle yield could be increased by starting with a higher cell concentration in the pre-extrusion sample, but this also resulted in clogging of the membrane and sample loss if a hand-extruder was used. The BV method was quicker and simpler, but the resulting particles were extremely heterogeneous, and the lysis was very inefficient. The combination of the BV method with extrusion did not result in improved lysis or an increase in particle quality. Although freeze/thawing and sonication have been shown to enhance cdNV yield, these methods can be harsh and may result in damage to biologically active components within the cdNVs. Consequently, the methods in question were not implemented in the formation of cdNV for this study, as the marginal advantages they offered were not enough to counterweight drawbacks and the extra effort required.

Due to the observed results obtained by extrusion, we decided to invest into a Lipex thermobarrel stainless steel extruder from Evonik which operates with an external pressure source and allows for usage of membranes with a bigger surface area. Through this the quality of extrusions was further improved and allowed the extrusion of denser cell suspensions. After forming the cdNVs through serial extrusion using the Lipex extruder, a screening was performed which revealed that cdNVs restore lipid droplets in naive LX-2 cells in a concentration-dependent

manner. However, to further analyse the activity potential of cdNVs, a downstream process is needed, allowing to study purified cdNVs.

Chapter 3.
Establishment of a downstream purification process of serially extruded cell-derived nanovesicles

3.1. Abstract

This study aimed to create a downstream purification process for cell-derived nanovesicles (cdNVs) optimizing yield and purity, without losing biological activity. Various methods were evaluated, including density gradient ultracentrifugation (DGC), size-exclusion chromatography (SEC), ultracentrifugation (UC), and sterile filtration. Stability studies showed that particles were more stable at lower temperatures, so all purification processes were conducted at 4 °C whenever possible. DGC on an iodixanol gradient was used as pre-purification, as it removed 70% of the proteins while conserving 60% of the cdNVs and enriching the sample. Even though higher particle purity could be achieved, SEC was not included due to the lower yield and stability of the purified particles. UC was used to pellet the particles and enable resuspension in low volumes of cell culture medium. Filtration through a 0.22 µm pore size regenerated cellulose (RC) filter was found to be the most effective method for aggregate removal and sample sterilization. The final purification process comprised DGC, followed by UC and sterile filtration, and resulted in a recovery of 40% of all particles while discarding 95% of the total protein.

3.2. Introduction

From the field of extracellular vesicles (EVs), we learned that the selection of an appropriate technique for particle isolation and purification plays a crucial role in ensuring the quality and reliability of the obtained EV preparations. The isolation technique will influence the yield, purity, size, shape, content, and thus the activity of the EVs[116-120]. Therefore, a comprehensive understanding of the strengths and limitations of each technique is necessary to optimize the quality of the isolated EVs and to ensure their suitability for downstream applications. EVs can originate from cultured cells but also from biological fluids, such as urine, saliva, or blood making the purification more complex due to the co-isolation of contaminants, such as lipoproteins[121, 122].

cdNVs are originating from a controlled monoculture and are particles with a more homogenous dispersion which simplifies the downstream process. Various techniques, such as UC[108], SEC[123], ultrafiltration[124], immunoprecipitation[125], tangential flow filtration (TFF)[126], among others, have been used alone or in combination. Each method has its own advantages and disadvantages, leading to EV samples with different yields and purities (**Figure 3.1.**). The choice of isolation technique depends on the type of sample, the intended downstream application, and the available resources. UC is a widely used method for EV isolation, but it has several limitations including damage to particles due to high centrifugal forces[127]. Density gradient ultracentrifugation (DGC) is a more sophisticated technique that allows the separation of particles based on their density, resulting in higher purity and yield compared to UC. However, the technique requires experienced staff, is time-consuming, and limits parallel sample processing. In contrast, SEC, another commonly used technique, can provide higher purity, but it often results in lower yield and diluted samples requiring an enrichment step afterward. Precipitation-based methods are faster and simpler, but they may lead to co-isolation of non-EV particles and protein contamination, resulting in reduced purity and yield of EVs[128]. Microfluidic-based approaches have emerged as a promising alternative for EV isolation due to their high specificity and reproducibility, as well as their ability to handle small sample volumes[129-131]. Moreover, microfluidic devices can integrate multiple isolation steps, into a single platform, allowing for rapid and efficient EV isolation[131]. However, the high cost and limited availability of microfluidic devices remain a challenge to their widespread use. TFF has raised as one of the most promising isolation techniques, due to its scalability allowing particle isolation from large volumes[126, 132], but they also come with high costs for specialised instruments and required membranes. Through a combination of several

methods, we were able to overcome certain limitations, especially the high shear stress of UC as the runs could be shortened.

The aim of this study was to develop a downstream strategy for the separation of cdNVs from proteins and other soluble factors. To achieve this, various combinations of UC, DGC, and SEC were tested and optimized. Additionally, different sterile filters with various membrane materials were evaluated as a sterilization method, optimizing for maximal particle recovery. The resulting particles were then characterized by their concentration, shape, protein content, RNA content, and biological activity.

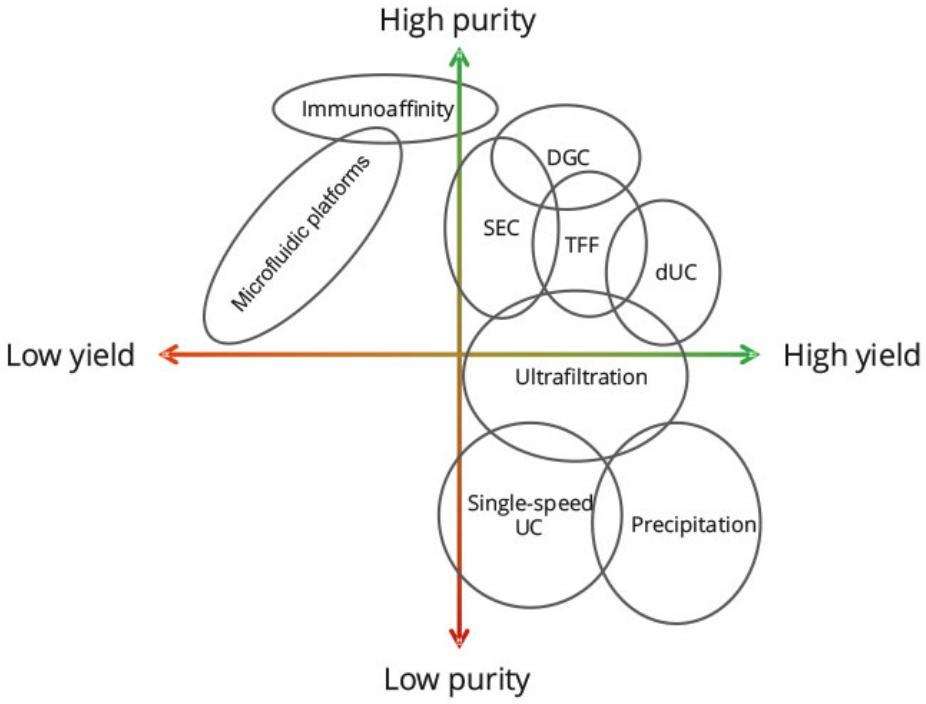

Figure 3.1. Commonly used purification processes.

Purification methods plotted based on the resulting extracellular vesicle (EV) yield (x-axis) and purity (y-axis). The outcome varies depending on which EV source is used, as well as protocol, equipment, and operator variations. SEC: size-exclusion chromatography, DGC: density gradient ultracentrifugation, TFF: tangential flow filtration, dUC: differential ultracentrifugation, UC: ultracentrifugation. (Image source: https://doi.org/10.47184/tev.2019.01.02)

3.3. Material and Methods

The formation process of cdNVs is described in Chapter 2. After formation kept the particles on ice or at 4 °C whenever possible to minimize degradation of components.

3.3.1. cdNV purification by DGC

The 50% (w/v) and 10% (w/v) Iodixanol (Alere Technologies AS, Norway) solution was prepared in 1x filtered (RC, 0.22 µm; ThermoFisher, USA) PBS (Carl Roth, Germany). A cushion was formed by pipetting 1 mL of a 4 °C 10% solution carefully on top of 1 mL of a 4 °C 50% solution in a thick-walled 10 mL PC centrifugal tube (Beckman Coulter, USA). To form the stack, a micropipette (Brandt, Germany) was used, and the centrifugal tube was held at an angle of 15°. The cdNV solution in PBS was then pipetted up to 6 mL on top of the Iodixanol. Ultracentrifugation was performed using an Optima L-90k ultracentrifuge (Beckman Coulter, USA) at 100’000 g for 1 h at 4 °C in a Type 70.1 Ti fixed-angle titanium rotor (Beckman Coulter, USA). Next, 1 mL fractions were carefully collected in pre-cooled Axygen reaction tubes (Corning, USA). The two main particle fractions were selected after particle concentration measurement by NTA (details described in Chapter 2).

3.3.2. cdNV purification by SEC

A 22.5 mL Sepharose Cl-2b matrix (Merck Millipore, USA) was filled into 1.5 cm diameter glass econo-columns (Bio-Rad, USA). Prior to loading the sample, the column was flushed with two elution volumes of filtered (RC, 0.22 µm; ThermoFisher, USA) and degassed PBS. The column was then loaded with up to 1 mL of cdNV solution and eluted with up to 45 mL of filtered and degassed PBS, with fractions collected in Axygen reaction tubes. After elution, the column was flushed with two bed volumes of PBS and one bed volume of 20% (v/v) ethanol (Biosolve, Netherlands) in MilliQ water for storage.

3.3.3. cdNV purification by UC

The cdNV main fractions from DGC or SEC were pipetted into a thick wall 10 mL PC centrifugal tube and diluted with filtered PBS up to 8 mL. The samples were pelleted with 140’000 g in an Optima L-90K UC for 2.5 h at 4 °C, unless otherwise specified. The sn containing all the soluble factors was collected, and it was enriched with a 10’000 MWCO Amicon Ultra-4 Centrifugal Filter Unit by centrifugation (15-30 min, 4’000 g) in a benchtop centrifuge. The transparent cdNV pellet was resuspended by vigorous up and down pipetting and vortexing, either in filtered PBS or in FBS-free DMEM. The particle concentration and protein content of the cdNV pellet and sn were measured by NTA and with a micro-BCA assay (as described in chapter 2).

3.3.4. Sterile filtration of cdNVs

The particle solution was passed through a filter with 0.22 µm pores for sterilization. Non-resuspended aggregates were pelleted briefly by quick spin centrifugation for 5 sec using a benchtop centrifuge (BlueSpin Mini; Serva Electrophoresis, Germany). The sn was then filtered through a pre-wetted 0.22 µm filter with various membrane materials. The sterile filtration was carried out aseptically under a laminar airflow cabinet (NuAir, USA).

3.3.5. RNA isolation

TRIzol reagent (ThermoFisher, USA) was used for total RNA isolation following the manufacturer’s instructions. The vesicles were lysed with TRIzol directly in the Axygen reaction tubes. A volume of chloroform equivalent to one-fifth of the total TRIzol volume was added to the samples, which were then vigorously vortexed for 10 sec and incubated at room temperature for 10 minutes. The samples were then centrifuged for 20 min at 4 °C and 16’000 g with a benchtop centrifuge. The upper phase was transferred to a new reaction tube and 1 µL glycogen (Merck Millipore, USA), as well as one volume of isopropanol (Biosolve, Netherlands), were added prior

to a 10 min incubation on ice for RNA precipitation. The RNA was pelleted by centrifugation for 10 min at 4 °C with a speed of 24'000 g. The sn was discarded, and the pellet was washed with 1 mL 70% EtOH in DEPC-treated (Carl Roth, Germany) MilliQ water. The ethanol washing was repeated twice and the final pellet was resuspended, after 5 min of air drying, in DEPC-treated MilliQ-water. Finally, the RNA concentration was measured using a NanoDrop (ThermoFisher, USA).

3.3.6. Transmission electron microscopy (TEM)

The Microscopy Imaging Centre (MIC) of the University of Bern performed TEM. For imaging of negatively stained samples, 5 µL of the vesicle suspension was adsorbed on glow-discharged and carbon coated 400 mesh copper grids (Plano, Germany) for 3 min. After washing the grids 3 times by dipping them in pure water, grids were stained with 2% uranyl acetate in water (Electron Microscopy Science, Switzerland) for 45 s. The excess fluid was removed by gently pushing them sideways to filter paper. The samples were then examined at 80 kV with a transmission electron microscope (Tecnai Spirit; FEI, USA) equipped with a digital camera (Veleta; Olympus Life Science, Germany).

3.4. Results

3.4.1. Particle enrichment with DGC on an iodixanol gradient

Upon extrusion, freshly formed cdNVs are diluted in the formation buffer containing contaminants from the cell cytosol, including soluble factors like proteins, peptides, nucleic acids, as well as non-soluble aggregates such as cell debris and protein aggregates. Thus, the isolation and enrichment of cdNVs from contaminants are essential to obtain a solution with a high particle concentration. A concentrated particle solution is desired because SEC columns can only be loaded with small volumes, and a highly concentrated solution is beneficial for cell culture assays in case

the particles need to be diluted into DMEM, or if small volumes are used in cell culture plates so that higher particle doses can be tested. To achieve an enrichment with purification, an OptiPrep gradient was used with 50% (w/v) and 10% (w/v) iodixanol. Iodixanol is non-ionic, non-toxic, sterile, endotoxin-free, and metabolically inert[133]. Therefore, iodixanol has been employed in various downstream processes for the purification and enrichment of cdNVs. Its ability to preferentially enrich cdNVs in the 10% Iodixanol fraction, while simultaneously excluding numerous soluble factors, has been reported in several studies[102, 109, 110, 134].

A total of 5 mL of freshly extruded cdNVs were carefully pipetted onto an iodixanol cushion consisting of 1 mL of a 10% (w/v) iodixanol solution layered on top of 1 mL of a 50% (w/v) iodixanol solution (**Figure 3.2a**). The process was performed at 4 °C, as preliminary studies revealed that the particles remain more stable on ice compared to room temperature (RT) (**Figure A3.1a**). After DGC for 1 h at 100'000 g most of the solution became transparent, whereas especially the 10% (w/v) iodixanol fraction turned milky suggesting a high particle presence (**Figure 3.2b**). Aggregates were visible at the interface of the solution to the 10% fraction and at the interface of the 10% and 50% fractions, which were either already present in the extruded sample and/or formed during DGC. One mL fractions were collected from the top to the bottom and their particle and protein concentration was measured. Most of the particles were not in fraction 2 as expected (DGC_2), but in fraction 3 (DGC_3) (**Figure 3.2c**). The particles were found to be mostly at the interface of DGC_3 and DGC_2 and depending on the collection they enriched in fraction DGC_3 or DGC_2. DGC_1 and DGC_4 contained 13% respectively 7% of the cdNVs, hinting that not all formed particles have the same density, whereas some particles could be aggregates or other particles not surrounded by a lipid bilayer. The size distribution analysis revealed that the particles in fractions DGC_1-4 were identical in size, while the few particles

detected in the other fractions were slightly larger (**Figure 3.2d**). The soluble proteins were distributed almost equally over all fractions with a slightly diminishing presence in iodixanol-containing fractions, whereas it cannot be excluded that those proteins found in iodixanol entered the iodixanol because they are associated with the particles. Achieving consistent results in pipetting the gradient is challenging and requires experience. As a result, better recovery was achieved with subsequent experiments, leading to some variability in the fractions obtained.

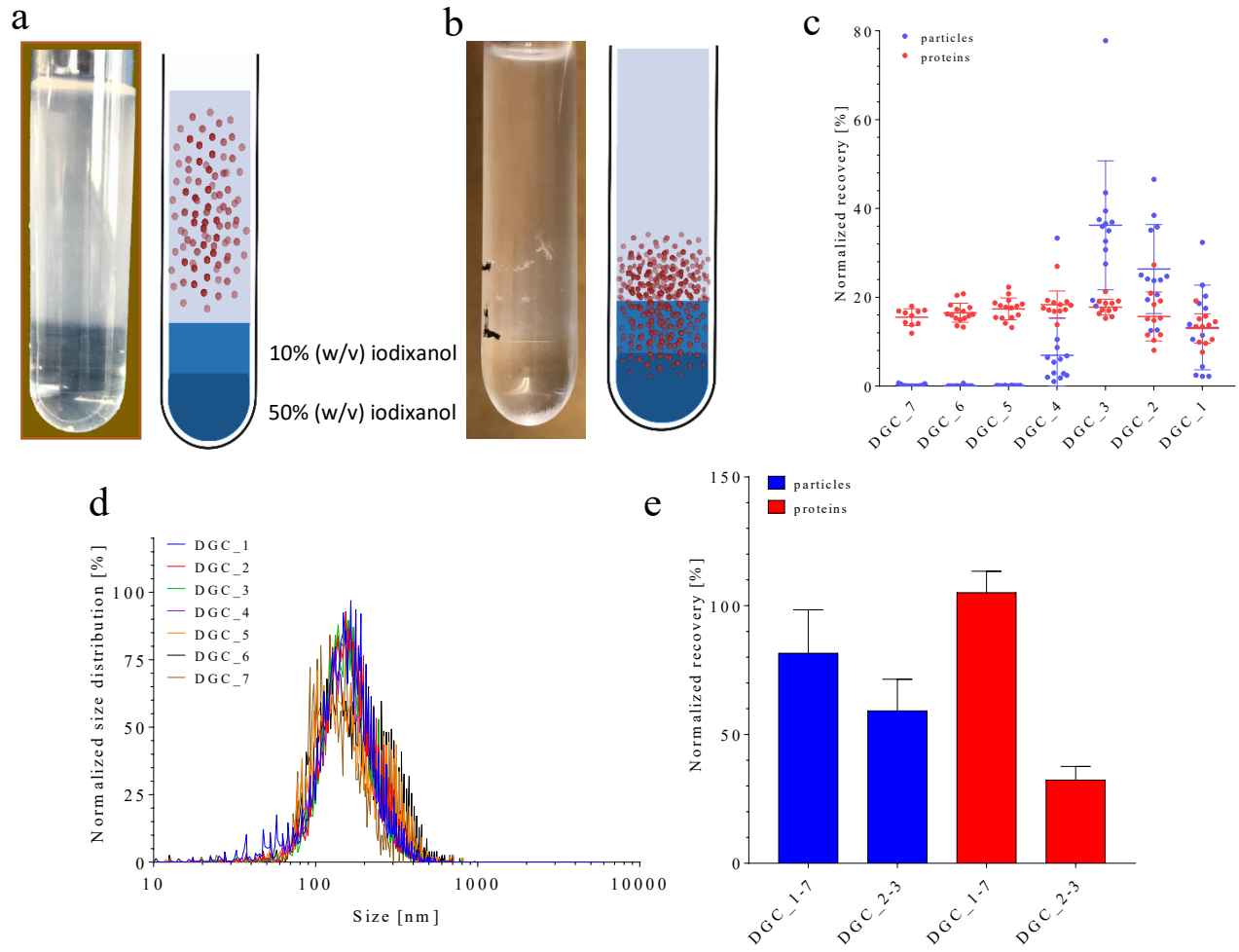

Figure 3.2. Evaluation of density gradient ultracentrifugation (DGC).

a, Image of freshly extruded cell-derived nanovesicles (cdNVs) on top of an iodixanol cushion and its schematic representation where the cdNVs are visualized as red dots. **b,** Image of a cdNV sample after DGC and its schematic representation showing the presence of cdNVs. **c,** Particle and protein recovery in different fractions (fraction 7 top fraction, fraction 1 50% iodixanol fraction) after DGC of freshly extruded cdNVs normalized to values obtained after 10 µm extrusion (mean ± SD, n ≥ 10). **d,** Size distribution profile of cdNVs in different fractions after DGC (mean ± SD, n = 3). **e,** cdNVs and protein yield in all DGC fractions compared to DGC fraction 2 and 3 (mean ± SD, n ≥ 7).

Overall, all proteins and slightly over 80% of the total particles were recovered after DGC. The DGC_3 and DGC_2 fractions contained the majority of the particles, accounting for 60% of the total, with only 30% of the total protein amount (**Figure 3.2e**). Thus, fractions DGC_2 and DGC_3 were collected and used for further downstream processing.

In order to avoid potential issues during further purification, it was attempted to eliminate aggregates that may cause clogging of the SEC column. Two approaches were employed: removal of aggregates prior to DGC to determine if new aggregates formed and removal of aggregates after DGC. The first method involved centrifugation at 9'000 g for 30 min, which effectively eliminated the aggregates but also resulted in the removal of over 60% of cdNVs that may have pelleted together with the aggregates (**Figure A3.1b**). Therefore, an alternative method using 0.22 µm filters was adopted, which selectively excluded aggregates while allowing nano-sized cdNVs to pass through. Six different hydrophilic membrane materials, including polypropylene (PP), regenerated cellulose (RC), cellulose acetate (CA), polyvinylidene fluoride (PVDF), nylon, and polyether sulfone (PES) were tested for filtration performance after serial extrusion. PP and nylon were not suitable as they resulted in significant particle loss (≥50%) (**Figure 3.3a**). The highest particle recovery (90%) was observed with RC filters, followed by CA (85%), PVDF (84%), and PES (80%). RC, CA, and PVDF filters also recovered 90% of the proteins, whereas PES only recovered 65%, meaning that it not only removed aggregates but also purified the system from proteins. However, due to the higher back-pressure observed, PES was excluded from further experiments, and RC was selected. The filtration of cdNVs before and after DGC through a RC membrane was compared showing that the recovery was slightly better if the filtration was performed post-DGC (**Figure 3.3b**). Even though filtration pre-DGC removed aggregates, aggregate formation still occurred during DGC. Hence, considering the aggregation formation

during DGC and slightly better recovery of particles after filtration post-DGC, chose to filter the particles post-DGC for aggregate removal prior to SEC.

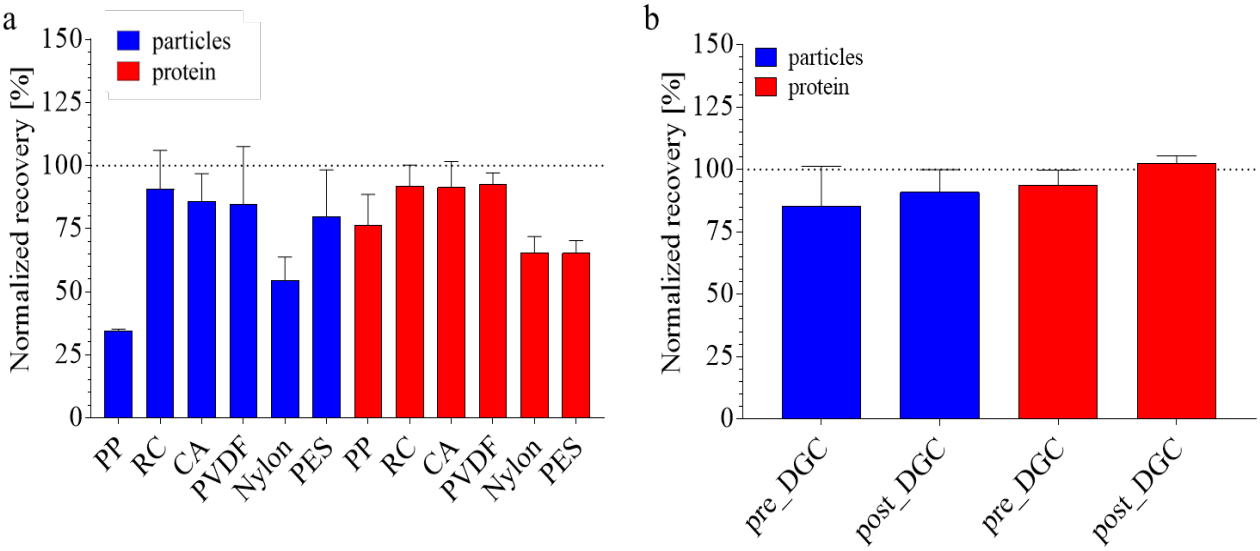

Figure 3.3. Effect of different membranes for sterile filtration on cell-derived nanovesicles (cdNVs).

a, Particle and protein recovery after 0.22 µm sterile filtration of freshly extruded cdNVs normalized to pre-filtration (mean ± SD, n ≥ 3). PP: polypropylene, RC: regenerated cellulose, CA: cellulose acetate, PVDF: polyvinylidene fluoride, PES: polyether sulfone. **b,** Comparison between the recovery of particles and proteins of cdNVs before and after density gradient ultracentrifugation (DGC), using 0.22 µm RC filtration (mean ± SD, n = 3).

3.4.2. Purification of cdNVs by SEC

After removal of aggregates from the two main DGC fractions the cdNVs were further purified by SEC. Therefore, an SEC column was prepared with a Sepharose Cl-2b matrix, as this matrix is very suitable to separate particles with a diameter of 150-200 nm from proteins due to its pore size of 75 nm[108, 135, 136]. Up to 2 mL of the sample could be loaded on the SEC, which was then eluted with filtered and degassed PBS. The SEC purified solutions contained 2.3 x 10^{11} ± 0.7 x 10^{11} cdNVs and 1145.00 ± 188.13 µg protein. The elution profile showed that almost all particles were eluted in fractions 6 and 7 (**Figure 3.4a**). There was considerable variability, but this was due to the manual collection of fractions. When both fractions were combined, the standard deviation was

reduced (**Table A3.1a**). Additionally, proteins co-eluted with vesicles in fractions 6 and 7. These proteins are presumed to be associated with the vesicles, possibly membrane proteins and/or proteins absorbed on the particle surface forming a corona. Overall, over 90% of the particles and 73% of the proteins were recovered after SEC (**Figure 3.4b**), whereas 77% particles and only 8.7% proteins were in fractions 6 and 7, indicating high purification of the sample (**Table A3.1b**). The number of particles and proteins decreased progressively after fraction 7 until fraction 11, where the remaining proteins started eluting. All particles eluted between fractions 5 and 9. Increasing the loaded particle amount to 8.0 x 10^{11} particles with 2240 µg protein did not change the SEC elution profile showing the scaling potential of the method (**Figure A3.2.**).

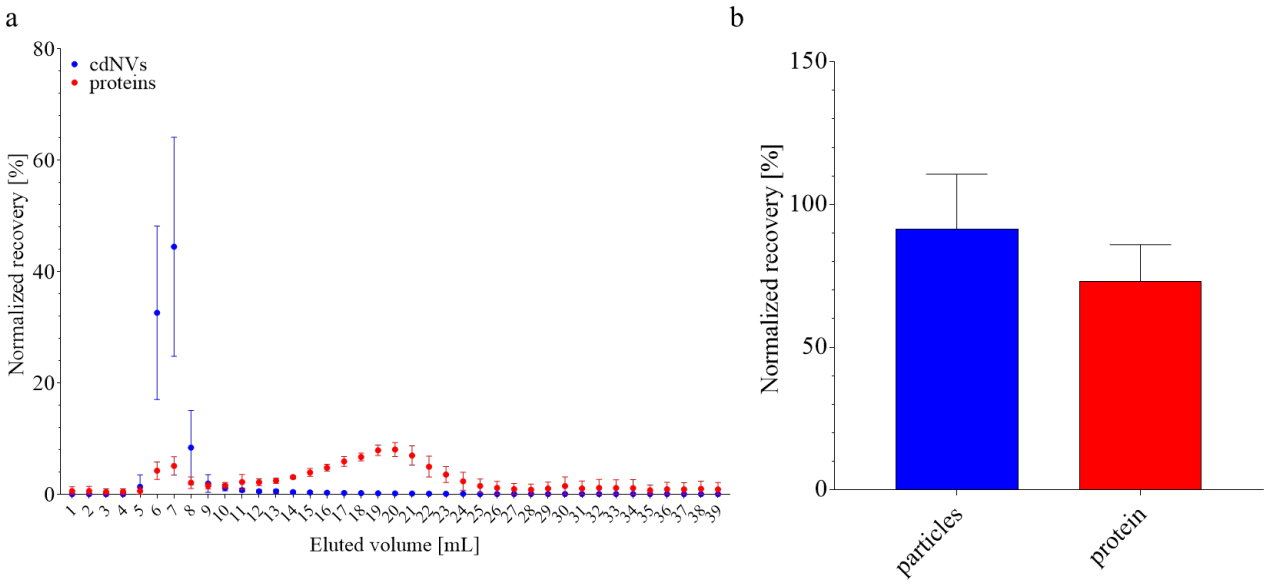

Figure 3.4. Evaluation of size exclusion chromatography (SEC).

a, SEC elution profile of density gradient ultracentrifugation (DGC) pre-purified cell-derived nanovesicles (cdNVs). The cdNV and protein amount was normalized to the loaded amounts (mean ± SD, n ≥ 3). **b,** cdNV and protein recovery after SEC normalized to the loaded amounts (mean ± SD, n ≥ 6). The particle recovery was 91.5% ± 19.2% and the protein recovery was 73.2% ± 12.7%.

3.4.3. Particle enrichment through UC

The SEC method was successful in purifying the cdNV sample, but it also resulted in dilution of the particles and the elution buffer was not suitable for cell culture experiments. To address this issue, UC was performed to concentrate the particles and enable their direct resuspension in the appropriate cell culture medium. Initially, different UC rotation speeds were evaluated first for cdNV samples after DGC and secondly for samples after DGC + SEC, to determine the optimal speed for particle and protein recovery in the pellet and supernatant (sn). The UC conditions were set at 4 °C and 2.5 h. Results indicated that speeds of 120'000 g or 140'000 g were optimal (**Figure 3.5a**), as lower speeds resulted in a significant number of particles remaining in the sn, and higher speeds caused particle destruction (**Figure A3.3a**). Notably, more particles were recovered after UC in the DGC pellet compared to the DGC + SEC pellet, possibly due to higher protein and iodixanol levels in the DGC sample, which might stabilize the particles. Interestingly, more loaded proteins were recovered after UC in the DGC + SEC pellet compared to the DGC pellet, even though more protein was present in the DGC sample prior UC (**Figure A3.3b**). This suggested, as hinted by the SEC elution profile, that these proteins are strongly associated with the particles as part of the hard cdNV corona and therefore pelleted together with the cdNVs. In contrast, the DGC sample contained more proteins not associated with the particles, which had not been removed by previous purification steps. Not all particles were recovered for both UC settings, indicating that some particles may still have been destroyed, due to the high centrifugal forces, or lost through aggregate formation. Therefore, to obtain a sterile and aggregate-free sample for treatments, the 0.22 µm sterile filtration (with RC membrane) was performed as a final step after UC. The recovery rate of particles post UC in the DGC sample was not affected by the speed of UC, but more particles were recovered in the DGC + SEC sample at 140'000 g than at 120'000 g, where

only 20% of the loaded particles were recovered. This cannot be due to the centrifugal force, as they were bigger in the condition with 140'000 g. Overall, 40% of all formed particles and only 4.2% of the proteins were recovered in the pellet if UC was performed right after DGC (**Figure 3.5b**). The addition of SEC prior to UC removed 50% more protein recovering only 2% of the total proteins present after 10 µm extrusion. However, also only 17% of the total cdNVs were recovered. Hence, the decrease in protein could be a result of a smaller recovered cdNV amount. The purification factor, which compares the ratio of particles to protein before and after purification revealed that UC after DGC purified cdNVs had 10 times less protein per particle compared to before purification, while addition of SEC led to a purification factor of 11.8, which was only slightly higher than without SEC (**Figure A3.3c**).

As the upstream and downstream processes are quite lengthy, the stability of particles purified using different processes was evaluated, and their stability was tested at 4 °C after DGC, DGC+UC, and DGC+SEC+UC. The results showed that particles with higher purity were less stable (**Figure A3.3d**), which is consistent with published findings that EVs are more stable in the presence of proteins[137]. Considering the minimal purity gain from SEC but also the additional processing time, the decreased throughput, and the increased particle instability compared to using DGC + UC only, it was decided to drop the SEC from the downstream pipeline. The final purification process included DGC, UC and RC 0.22 µm filtration. The purification process was validated with cdNVs derived from differently pre-treated LX-2 cells. All cdNVs had the same size distribution, showing no aggregates (**Figure 3.5c**) and yielded 10^4 particles per LX-2 cell (**Figure 3.5d**). Transmission electron microscopy confirmed the round shape and hydrodynamic diameter obtained by NTA of cdNVs (**Figure 3.5e**). The sn contained fewer particles (~8x less particles compared to the pellet), more protein (**Figure A3.3e**), and less RNA (**Figure A3.3f**).

However, due to the presence of soluble factors such as particles, peptides, proteins, and nucleic acids, the sn was kept as a control for cdNV activity studies.

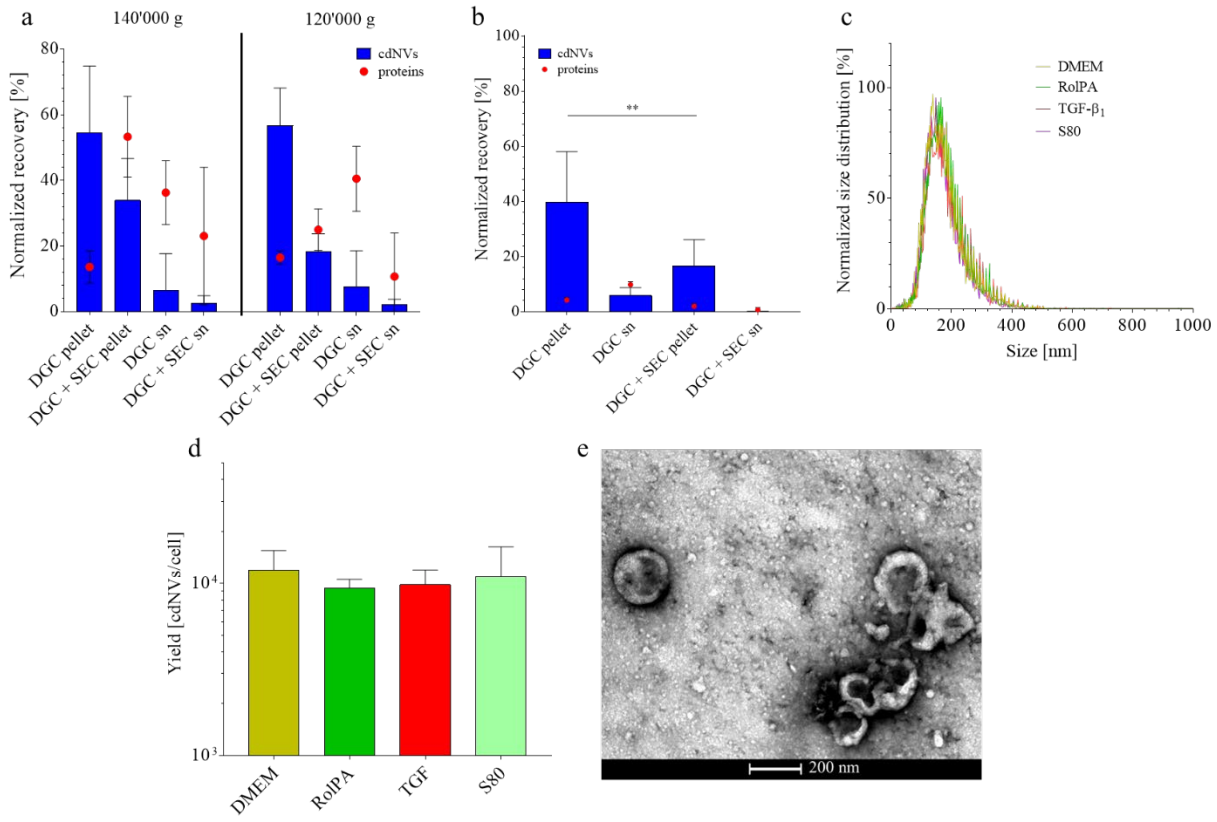

Figure 3.5. Evaluation of ultracentrifugation (UC).

a, Recovery of cell-derived nanovesicles (cdNVs) and proteins in the pellet and supernatant (sn) of samples after UC at two different speeds (120'000 g and 140'000 g) that underwent pre-purification by density gradient ultracentrifugation (DGC) alone and DGC followed by size exclusion chromatography (DGC + SEC) (mean ± SD, n ≥ 3). The data was normalized to the loaded amounts. **b,** Recovery of cdNVs and proteins after UC normalized to the amount obtained after 10 µm extrusion (mean ± SD, n ≥ 4) (Welch's t-test for particle recovery between DGC pellet and DGC + SEC pellet, p-value 0.0023). **c,** Size distribution profile of purified cdNVs derived from differently pre-treated LX-2 cells (mean ± SD, n = 3). **d,** Purified cdNV yield per cell of differently pre-treated LX-2 cells (mean ± SD, n = 5). There was no significant difference between the different conditions (Ordinary one-way ANOVA). **e,** TEM image of DGC + UC + 0.22 µm filter purified cdNVs derived from untreated LX-2 cells.

3.5. Discussion and conclusion

Different purification methods and protocols were assessed to establish a downstream pipeline for obtaining high yield and purity of cdNVs. The evaluated methods included density gradient ultracentrifugation (DGC), size-exclusion chromatography (SEC), ultracentrifugation (UC), sterile filtration, and high-speed centrifugation, either alone or in combination. Stability studies indicated that purification processes should be performed at 4 °C as the particles were more stable at lower temperatures. DGC was suitable for pre-purification after extrusion, as it did not only remove 70% of the proteins while conserving 60% of the cdNVs but also enriched the particles. However, particle recovery varied, and some particles were lost due to aggregation during DGC. The variation came from the preparation of DGC. Forming the stack for DGC is not easy and requires patients, as well as experience. Hence, with repetition, the particle yields also increased. The majority of the particles were localized at the interface of the buffer and 10% iodixanol fraction. Approximately 30% of the particles were detected in the 10% iodixanol fraction, as well as at the interface of the 50% iodixanol fraction. Around 10% of the particles were found in the 50% iodixanol fraction suggesting the presence of particles with varying densities. Hence, altering the duration and velocity of the centrifugation, and introducing additional iodixanol fractions of varying concentrations, may lead to the identification of particle subtypes generated by serial extrusion, and enhance the yield, as not all particles are retrieved during DGC. Aggregates formed during DGC were possibly caused by high centrifugal forces and the presence of soluble factors, such as peptides, proteins, and nucleic acids. Therefore, DNase treatments may lower aggregation during downstream processing and reduce DNA transfer risks, as demonstrated by other studies[90].

To eliminate aggregates, high-speed benchtop centrifugation at 9’000 g for 30 min was evaluated. Although via this approach all aggregates could be successfully removed, a significant amount of

cdNVs were also discarded. This could be attributed to the co-precipitation of particles with aggregates, as well as the potential loss of particles resulting from the execution at room temperature. Hence, tested filtration through a membrane with 0.22 µm pores and different hydrophilic membrane materials. RC, CA, and PVDF were found to be suitable candidates as they removed all aggregates and recovered approximately 90% of the particles. RC filters were selected due to their slightly superior performance. Before filtration, it is important to consider the loading factor of the used filter, as it indicates the number of particles that can be filtered per surface area unit. For highly concentrated samples, a larger surface area has to be utilized to reduce the risk of clogging and excessively high back pressure leading to membrane breakage. Other potential approaches for aggregate removal include filtration through larger pore sizes, such as 0.45 µm. However, due to the unavailability of alternative sterilization methods like ionizing radiation, we utilized the filters not only for aggregate removal but also for the sterilization of cdNVs and therefore kept the filtration through 0.22 µm pores. As sterilization is needed for cell treatments, it was decided to be done as the final step of the purification procedure.

The inclusion of SEC in the purification process was considered due to the difference in size between cdNVs and proteins, making separation possible. Soluble proteins were removed from cdNVs with an efficiency of nearly 100%, while 77% of particles were recovered in two main fractions. SEC revealed the existence of strongly associated proteins that are either a constituent of the hard protein corona and/or incorporated into the lipid bilayer as membrane proteins. However, further experiments such as proteomics or protein digestion with proteinases would be needed to confirm the association. Potentially, the recovery of particles could have been improved if SEC had been conducted at 4 °C instead of room temperature, but this might also have slowed down the elution.

In order to test the biological effect of cdNVs on cells, it is required that they are resuspended either in cell culture medium or present in a high concentration, which can be diluted into the medium. A UC step was incorporated either directly after DGC or SEC to pellet the particles, enabling the particles to be resuspended in low volumes of cell culture medium. The UC protocol was standardized with a fixed temperature of 4 °C and a duration of 2.5 h, while varying rotational speeds. Among the tested speeds, 140'000 g resulted in the highest recovery. However, recovery differed when comparing samples before and after SEC. Results from the stability studies and UC experiment revealed that DGC + SEC + UC-purified particles were less stable compared to those purified only by DGC + UC, which was attributed to their lower content in protein. Therefore, optimizing UC protocols according to the specific sample source is essential for maximal recovery. Due to the lower yield of cdNVs obtained with SEC and the decreased stability of the particles, the decision was made not to utilize SEC for downstream purification. Instead, the purification process was concluded with DGC, followed by UC and sterile filtration (**Figure 3.6.**), recovering 40% of all particles while removing 95% of all proteins.

To fully validate the purification process, activity tests are required to measure if the fibrosis resolving properties are retained in the pure cdNVs. Detailed information on the activity studies is to be found in the next chapter. The soluble factors in the sn collected after UC were enriched and used as a control treatment.

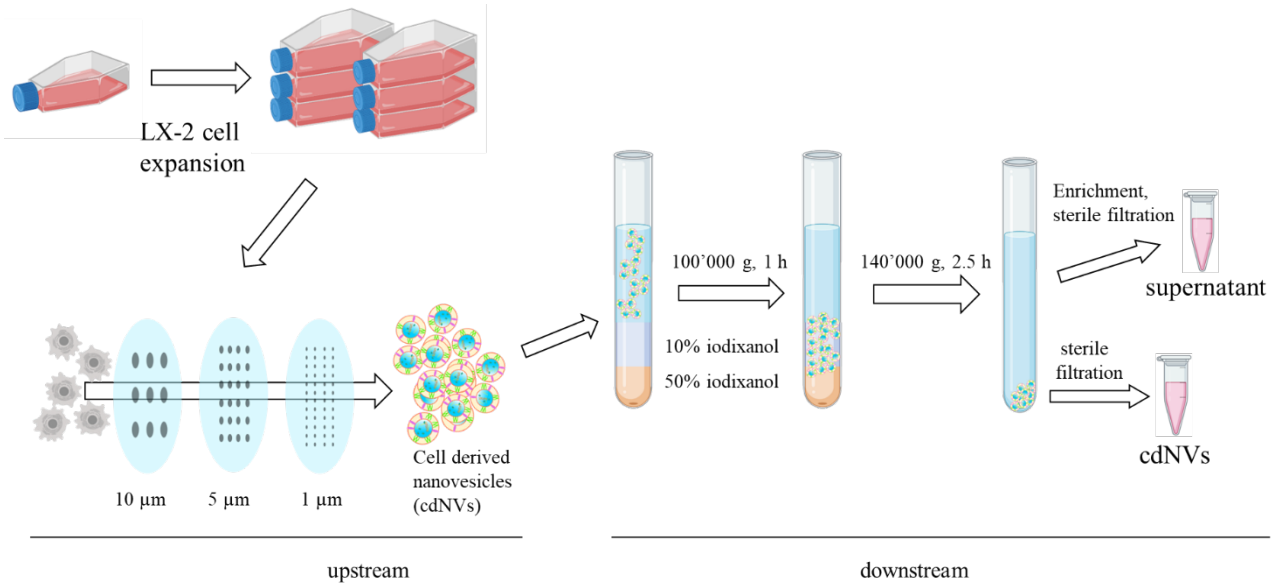

Figure 3.6. Schematic visualization of formation and purification process for cell-derived nanovesicles (cdNVs).

During the upstream process, LX-2 cells are expanded in 2D cell culture and cdNVs are formed by serial extrusion. The downstream process consists of density gradient ultracentrifugation on an iodixanol gradient followed by ultracentrifugation. The pellet as well as the supernatant are collected and sterile filtered before application.

Chapter 4.
Investigation of cell-derived nanovesicles as potential therapeutics against chronic liver diseases

This chapter has been submitted for publication.

Aymar Abel Ganguin, Ivo Skorup, and Paola Luciani

Department of Chemistry, Biochemistry and Pharmaceutical Sciences, University of Bern, Bern, Switzerland

Author's contribution

P.L. conceived and supervised the original project. A.G. devised and performed all the experiments and analysed the data. I.S. supported in devising, performing, and analysing the cellular uptake experiments. A.G. led manuscript writing. P.L. and I.S. reviewed and edited the manuscript.

4.1. Abstract

This study aims to address the lack of effective therapeutics for liver fibrosis, a reversible chronic liver disease, by investigating the formation and purification of cell-derived nanovesicles (cdNVs) from untreated, quiescent, and activated LX-2 cells, an immortalized human hepatic stellate cell (HSC) line with key features of transdifferentiated HSCs. Treatment of naïve and through transforming growth factor beta 1 (TGF-β1) activated LX-2 cells with cdNVs results in a concentration-dependent reduction in cell activation both phenotypically and genotypically. The beneficial effects of cdNVs are linked to the functional corona on their surface. Liposomes formed from lipids obtained through extraction from cdNVs show a reduced anti-fibrotic response in perpetuated LX-2 cells and less efficient cellular uptake, whereas incubation with soluble factors collected during purification results in a new surface corona restoring anti-fibrotic potential. Overall, cdNVs exhibit encouraging therapeutic properties, making them a promising candidate for the development of liver fibrosis resolving therapeutics.

Keywords: cell-derived nanovesicles (cdNVs), LX-2 cells, surface corona, anti-fibrotic potential

4.2. Introduction

The liver is involved in various vital functions, such as vitamin storage,[138] clearance of damaged erythrocytes,[12] elimination of xenobiotics,[139] synthesis of plasma proteins,[140] lipid management,[141] immune response,[142] and more. Injuries to this organ, caused e.g., by viral infections, fatty diets and/or alcohol abuse[22] lead to the formation of extracellular matrix (ECM) proteins,[143] which is an essential part of the wound-healing response. However, if the cause of injury is not resolved, such as in chronic liver diseases, the reversible[22] fibrosis formation will be

promoted leading eventually to irreversible liver cirrhosis, liver cancer and liver failure, due to non-resolved excessive ECM protein production which leads to the formation of scars and loss of organ function,[144] where only a transplantation can save the patient, making the liver the second most transplanted solid organ worldwide.[145] The development of liver fibrosis involves different cell types, cytokines, and response cascades.[22, 146] Hepatic stellate cells (HSCs) have been described to be the major driver of the fibrosis progression in the liver.[147] During physiologically healthy conditions, HSCs are in a quiescent (inactive) state in which they store vitamin A (retinol) in cytoplasmic lipid droplets.[148] Upon activation, HSCs undergo a trans-differentiation into a highly proliferative myofibroblast-like status.[147, 149] In this activated state HSCs proliferate, rapidly lose their ability to store lipid droplets and start producing a lot of ECM components, such as alpha-smooth muscle actin (αSMA), fibronectin, type I and III collagens, as well as the profibrogenic cytokine transforming growth factor beta 1 (TGF-β_1) which further activates other HSCs.[144, 147] The Global Burden of Diseases, Injuries, and Risk Factors Study 2017 (GBD 2017) estimated that 1.5 billion people were suffering from chronic liver diseases worldwide[150] being directly accounted for 2 million yearly deaths,[23] with an increasing tendency. Concerning the worldwide rising obesity and diabetes[151] and the fact that only 11 high-income countries are projected to be able to eliminate all hepatitis virus C infections by 2030,[152] new effective therapies are needed to fight the already present increase in patients reducing the need of lifesaving transplantations.

Extracellular vesicles (EVs) have been extensively studied in the past two decades and show great promise for both diagnostic and therapeutic purposes in a variety of diseases.[81] Because of their physicochemical properties, EVs can pass through biological barriers, elicit a low immune response, and thus have a longer circulation time *in vivo*.[84] Proteins, peptides, nucleic acids,

metabolites, and lipids can be carried by EVs and functionally transferred to target cells.[84] Expression of cell specific epitopes on the EV surface enhanced targeted administration *in vivo*[153-155]. As a result, EVs released from various cell sources, such as hepatocytes,[156] endothelial cells,[157] fibrocytes,[156] macrophages,[156] mesenchymal stem cells (MSCs)[69, 156], induced pluripotent[146, 156] and HSCs[156, 158] have been used to treat liver fibrosis. Depending on the cell state and harvesting point various outcomes can be obtained. For example, EVs from palmitic acid (fibrotic)-treated hepatocytes[159] as well as EVs from injured hepatocytes[156, 160] led to the activation and progression of HSCs. Consequently, it is crucial to understand the source of the EVs. Yet, the use of EVs do not results only in advantages but may also present drawbacks, which makes the translation to clinical trials and thus to a valid biotherapeutic difficult. The main limitations of EVs are their heterogenicity of the particles and the cargo, functional diversity, scalability, lack of regulations[84, 158] and ethical concerns, when stem cells such as mesenchymal stem cells (MSC) are used as a source. Engineered nanovesicles inspired by the biology of natural EVs have shown great promise in being a valid alternative,[96] showing to be able to keep key biological and therapeutical features while tackling issues in production, scalability, and standardization.[86, 90, 91, 161]

In a prior study conducted by our group, it was demonstrated that extracellular vesicles (EVs) harvested from quiescent-like LX-2 cells, a human hepatic stellate cell (HSC) line with retained key features of transdifferentiated human HSCs,[55] resulted in a phenotypical shift towards an anti-fibrotic state upon administration to LX-2 cells.[108] Thus, it was hypothesized that the generation of artificial EVs from quiescent LX-2 cells would retain the fibrosis-resolving properties of the cells and may serve as a potential therapeutic agent against liver fibrosis. Particles generated directly from cells have been described with different names in literature, such as artificial

exosomes,[86] exosome mimetic nanovesicles,[89] cell-engineered nanovesicles,[109] nanoghost[162] etc., were named cell-derived nanovesicles (cdNVs) as previously described in other published work.[99]

To de-activate LX-2 cells and bring them to a state of quiescence, the cells were treated with either retinol or palmitic acid, which have been established as the gold standard for in vitro fibrosis resolution based on previous studies,[54] or with the polyenylphosphatidylcholine-rich (>75%) S80 liposomes, which have been demonstrated to exhibit anti-fibrotic effects on LX-2 cells[45]. To produce highly fibrogenic, perpetuated LX-2 cells, TGF-β1 was utilized, as previously described.[55, 163] After formation of cdNVs by serial extrusion of differently pre-treated LX-2 cells (antifibrotic/fibrotic), purified the cdNVs using a combination of density-gradient ultracentrifugation, as well as standard ultracentrifugation. The formed cdNVs were characterized by size, particle concentration, protein amount, and their biological activity on naïve, as well as through TGF-β_1 perpetuated LX-2 cells.

4.3. Results

4.3.1. Formation and purification of cell-derived nanovesicles

To establish the best working protocol formed cdNVs from expanded untreated (DMEM) LX-2 cells (3.0 x 10^7 LX-2 cells) and characterized the resulting particles in terms of size, yield, morphology, protein content and zeta potential. As schematized in **Figure 4.1.**, LX-2 cells were harvested from T175 flasks and cdNVs were formed by serial extrusion. Subsequently, the formed particles were purified by density gradient ultracentrifugation on a 50% (w/v) iodixanol and 10% (w/v) iodixanol cushion, followed by ultracentrifugation. The resulting cdNV sample contained

40% of the particle amount but less than 5% of the protein amount (**Figure A4.2a**). The soluble factors, which are mostly peptides and proteins, ended up in the supernatant (sn).

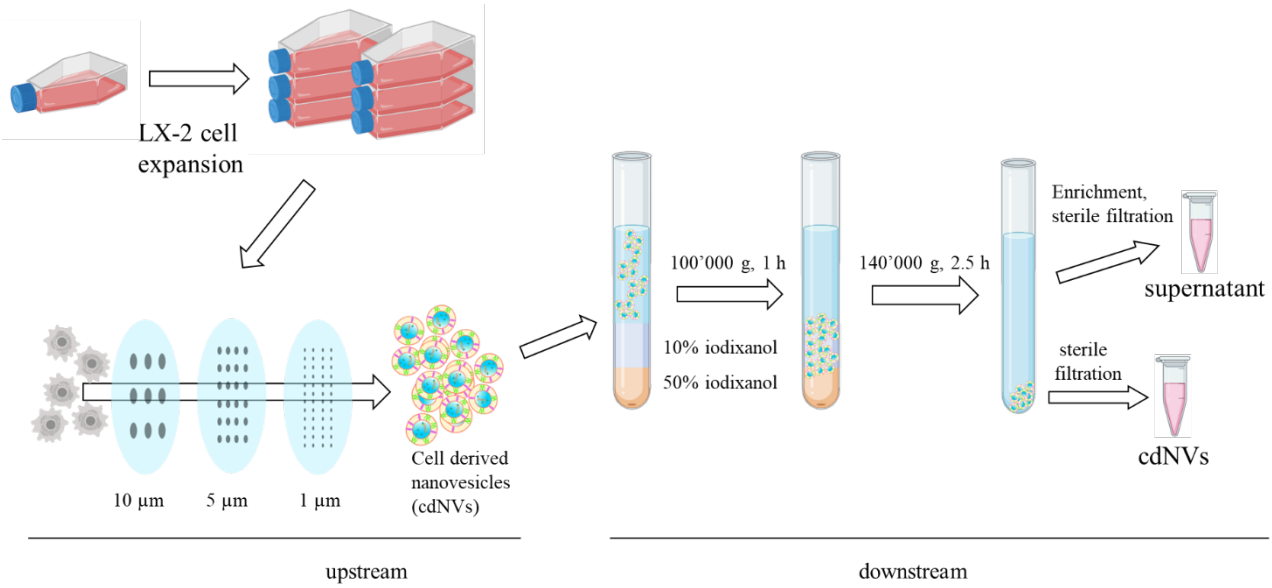

Figure 4.1. Formation and purification of cdNVs.
Illustration of the formation of cell-derived nanovesicles (cdNVs) from LX-2 cells. Untreated or treated LX-2 cells are harvested and serially extruded to form cdNVs, which are then purified with density gradient ultracentrifugation followed by ultracentrifugation. The supernatant (sn) was used as control in activity experiments.

The formed cdNVs showed a hydrodynamic diameter below 200 nm from the first extrusion on (**Figure 4.2a**), whereas further purification lowered the number of particles bigger than 200 nm and increased the number of particles smaller than 200 nm (**Figure 4.2b**). The hydrodynamic diameter of cdNVs was 175 nm and was constant over cdNVs derived from all tested LX-2 cells pre-treatments (**Figure A4.2b**). The surface charge of cdNVs was -38 mV at neutral pH and did not change with different LX-2 conditions (**Figure A4.2c**). TEM images confirmed the spherical morphology of the particles and the measured diameter (**Figure 4.2c**). Different pre-treatments of LX-2 cells prior cdNV formation did not change the size distribution (**Figure 4.2d**) nor significantly changed the yield/cell (**Figure 4.2e**) (Ordinary one-way ANOVA not significant (p value>0.1)).

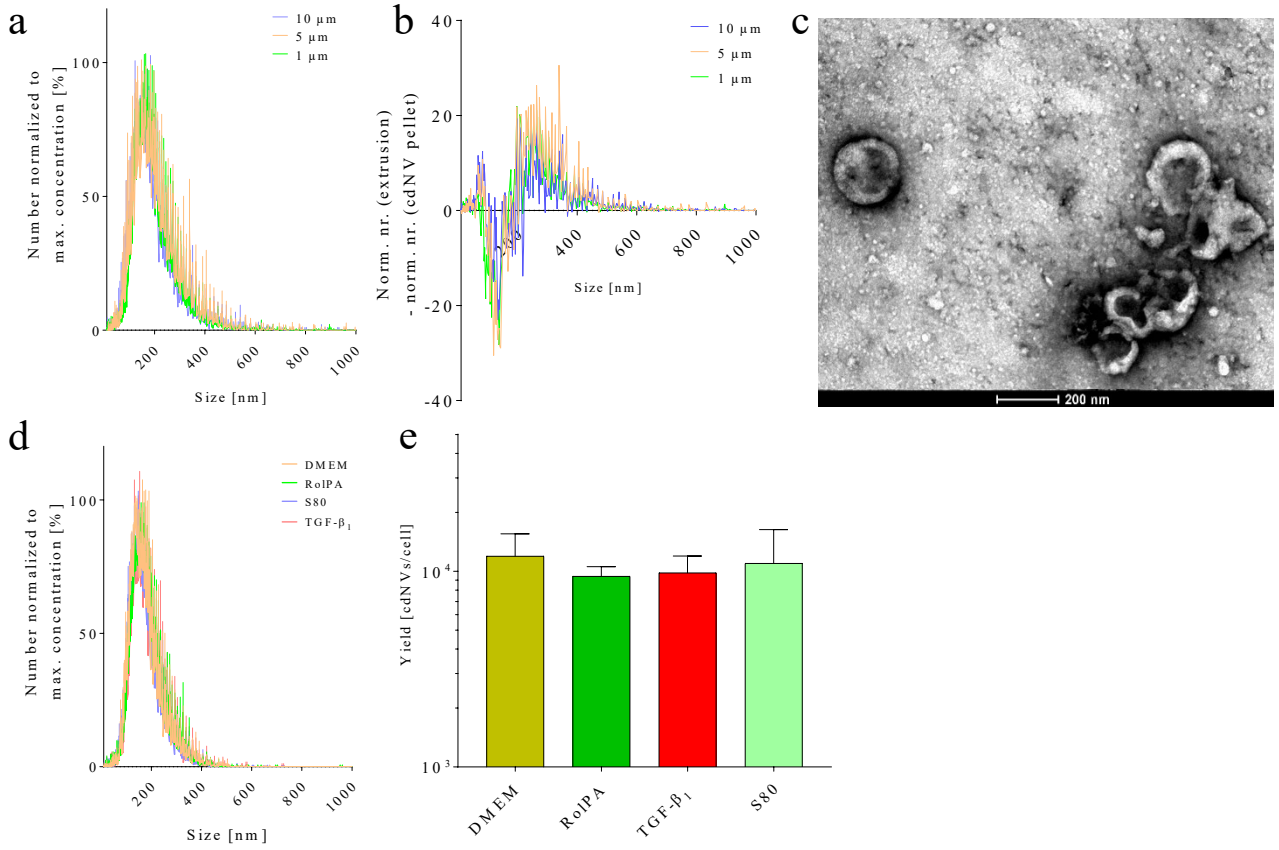

Figure 4.2. Characterization of cdNVs.
a, Size distribution profile of cell-derived nanovesicles (cdNVs) after formation through serial extrusion of untreated LX-2 cells (mean ± SD, n = 3). **b,** Subtraction of the particle number after purification (cdNV pellet) from the particle number after extrusion of untreated LX-2 cells (mean ± SD, n = 3). **c,** TEM image of purified cdNVs derived from untreated LX-2 cells. **d,** Size distribution profile of purified cdNVs derived from differently treated LX-2 cells (mean ± SD, n = 3). **e,** cdNVs derived from differently treated LX-2 cells yield normalized to the number of LX-2 cells used for the formation. (mean ± SD, n = 5).

4.3.2. Treatment of naïve LX-2 cells with cell-derived nanovesicles obtained from LX-2 cells treated with either S80 or TGF-β1

As previously shown by our group, S80 liposomes have a beneficial effect on the resolution of naïve LX-2 cells,[45] whereas TGF-β1, a primary fibrotic cytokine in liver diseases,[55] perpetuates LX-2 cells by activation. Due to their opposite effect, S80 and TGF-β1 were selected as pre-

treatment for LX-2 cells. The formed cdNVs from fibrotic and quiescent (cdNV_TGF/ cdNV_S80) origin were tested on naïve LX-2 cells. First, the outcome of freshly formed cdNVs on the metabolic activity of naïve LX-2 cells was evaluated by resuspending the particles after purification in cell medium to a final concentration of 4.5 x 10^{10} cdNVs/mL and incubating them on the seeded naïve LX-2 cells for 24 h. Treatment of naïve LX-2 cells with 4.5 x 10^{10} cdNVs/mL led to a 25% increase in metabolic activity for both cdNV_S80 and cdNV_TGF, showing no toxicity (**Figure A4.3a**). This was more than the result obtained by direct treatments with TGF-β_1 or S80 respectively, which both barely changed the cell metabolism.

Lipid droplets can be used to determine the phenotype of LX-2 cells.[45, 54, 108] They are present in a quiescent-like state, such as after treatment with retinol supplemented with palmitic acid, the gold-standard for *in vitro* fibrosis resolution, and absent in naïve or activated LX-2 cells.[36, 164] Lipid droplets can be stained with Oil Red O (ORO) and appear as red spots in fluorescent images (ORO FL) or as brown spots in bright field images (ORO BF) under a fluorescent microscope. Succeeding treatment with 4.5 x 10^{10} cdNVs/mL, we semi-quantified lipid droplets in naïve LX-2 cells through normalization of the area of droplets by the number of cells (stained with DAPI) (**Figure 4.3a**). No difference was observed in the amount of lipid droplets upon treatment with cdNV_S80 and cdNV_TGF, suggesting an anti-fibrotic phenotype in LX-2 cells after administration of both nanovesicle samples respectively (**Figure 4.3b**). The quiescent phenotype observed in naïve LX-2 cells after cdNV application was not as pronounced as with the anti-fibrotic controls of direct treatment with 10 µM retinol and 300 µM palmitic acid or 5 mM S80 and was not significantly different from the vehicle control, where no lipid droplets were observed (**Figure 4.3a/b**). However, if the S80 liposomes were diluted to reach the same particle

concentration as in the cdNV treatment no difference in droplet presence was observed (ordinary one-way ANOVA) (**Figure A4.3b**).

After observing a transformation of the naïve LX-2 phenotype, wanted to confirm the quiescent-like state by measuring the effect of cdNVs on the genotype of naïve LX-2 cells by qPCR. Therefore, three different fibrotic mRNA markers were analysed. The first gene of interest was COL1A1, which codes for the pro-collagene-aplha-type-1 protein and which is upregulated in activated hepatic stellate cells as a wound healing response.[35, 55] The second analysed gene was SPARC, which codes for the secreted protein acidic and cysteine rich (SPARC) protein, which is upregulated in activated HSCs.[108, 165] The function of SPARC is to enhance cell migration to the site of injury by binding and remodelling extracellular matrix proteins[166]. The third studied gene was PLIN2, which codes for the adipose differentiation related (ADRP) protein, enhanced in quiescent cells and responsible for the regulation and lipolysis of lipid droplets.[54, 167] COL1A1 mRNA translation was decreased by 70% upon cdNV_S80 treatment and 50% upon cdNV_TGF treatment (**Figure 4.3c**). SPARC mRNA translation was decreased 50% upon cdNV_S80 and 30% upon cdNV_TGF treatments, respectively. PLIN2 mRNA translation was increased 50% after both cdNV treatments. Hence, all three studied markers confirmed the anti-fibrotic potential of cdNVs. Even though treating naïve LX-2 cells with cdNV_S80 showed a more enhanced trend towards quiescent transformation in naïve LX-2 cells compared to cdNV_TGF, it is still unclear if the pre-treatment of LX-2 cells prior cdNV formation influenced their outcome, as the difference was not significant (ordinary one-way ANOVA). Also, if there was pre-treatment specificity, a pro-fibrotic response would have been expected from cdNV_TGF. If the S80 liposomes were diluted to the same particle concentration as in cdNVs prior treatment, the same amount of lipid droplets and PLIN2 mRNA expression was observed as upon cdNV administration (**Figure A4.3c**). However,

a minimal effect on COL1A1, like the observed decrease after control treatment with 1 mM HEPES, and no effect on SPARC was obtained. This indicates that the addition of specific lipids and the resulting increase in PLIN2 mRNA transcription alone were not enough to trigger an anti-fibrotic response and that therefore, other factors in the cdNVs impact the fibrosis regression.

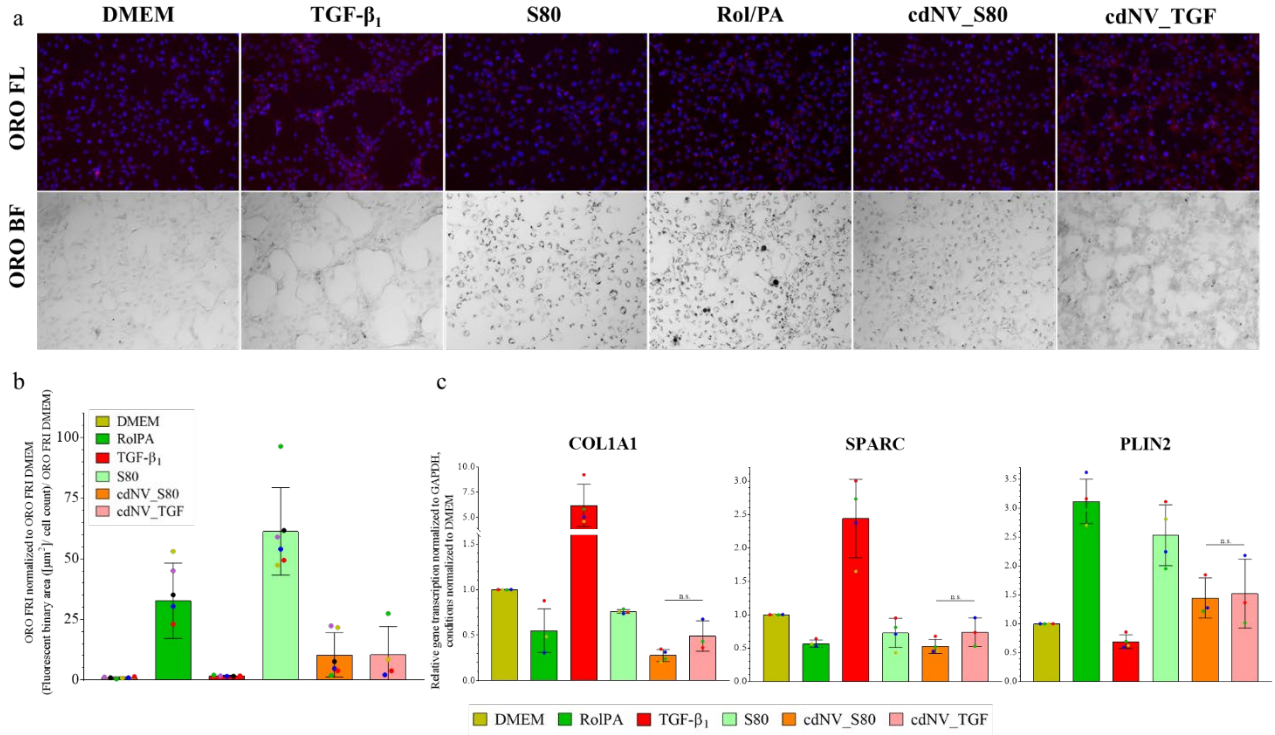

Figure 4.3. Effect of cdNVs on naïve LX-2 cells.
a, Representative 10x microscopy images of lipid droplets stained with Oil red O (ORO) in differently treated naïve LX-2 cells. Lipid droplets in fluorescence (ORO FL) show in red (nuclei counterstained with DAPI (blue)) and in bright field (ORO BF) show in brown. **b,** Graph showing the ORO fluorescence normalized to the cell count in the DAPI field (FRI) and normalized to the ORO FRI of DMEM (mean ± SD, n ≤ 3) (p-values from ordinary one-way ANOVA with post post-hoc Tukey test in supplementary table S2). **c,** Relative mRNA transcription in naïve LX-2 cells of three fibrosis markers (COL1A1, SPARC, PLIN2) normalized to GAPDH mRNA transcription and normalized to the DMEM condition after treatment with 4.5 x 10^{10} cell-derived nanovesicles (cdNVs)/mL derived from S80 or TGF-β_1 treated LX-2 cells and the corresponding controls (mean ± SD, n ≤ 3) (p-values from ordinary one-way ANOVA with post post-hoc Tukey test in supplementary tables S3/4/5).

4.3.3. Treatment of TGF-β_1 activated LX-2 cells with cell-derived nanovesicles derived from LX-2 cells treated with DMEM, RolPA, S80, or TGF-β_1

HSCs release TGF-β_1 in fibrosis development which leads to a strong activation of neighbouring HSCs.[168] Therefore, the effect of cdNVs derived from untreated, RolPA, TGF-β_1, and S80 treated LX-2 cells on TGF-β_1 activated LX-2 cell viability was tested in a dose-dependent manner with three different concentrations (A = 1.5 x 10^{10} cdNVs/mL; B = 3.0 x 10^{09} cdNVs/mL; C = 6.0 x 10^{08} cdNVs/mL) and compared to the direct treatments with DMEM, RolPA, TGF-β_1, and S80, as well as the sn collected during cdNV production diluted to the same protein amount as in the cdNV samples (A = 20 µg/mL; B = 4.0 µg/mL, C = 0.8 µg/mL) (**Table A4.1.**). The cells treated with the highest concentration of cdNVs showed a higher cell viability compared to the direct treatments DMEM, RolPA, TGF-β_1, and S80 (111% vs 100% for cdNV_DMEM_A; 121% vs 92% for cdNV_RolPA_A; 133% vs 95% for cdNV_ TGF_A; 109% vs 80% for cdNV_S80_A), whereas only cdNV_ TGF_A was significantly different from its direct treatment with TGF-β_1 (Ordinary one-way ANOVA, p-value = 0.0006) (**Figure 4.4a**). The induced cell proliferation was observed to be dose-dependent in all cdNV samples, wherein lower concentrations led to a smaller increase and in case of cdNV_DMEM_B, cdNV_DMEM_C and cdNV_S80_C even a decrease in cell viability was observed (88%, 92%, and 84%, respectively). The difference in cell viability increases of cdNV_RolPA and cdNV_TGF compared to cdNV_DMEM and cdNV_S80 were not significant and might be explained due to general biological variations obtained in cell culture experiments. Treatment with sn samples barely had an influence on the cell metabolism sn_DMEM and sn_S80 increase the metabolism by 10% in a concentration dependent manner, whereas sn_RolPA had no effect at all an sn_TGF decreased the viability by 10% for all tested concentrations.

To further investigate the effect of cdNVs derived from differently pre-treated LX-2 cells on TGF-β_1-activated LX-2 cells, we compared their influence on the translation of the same three genes. Proliferated LX-2 cells showed a 6-fold and 2.5-fold increase in COL1A1 and SPARC

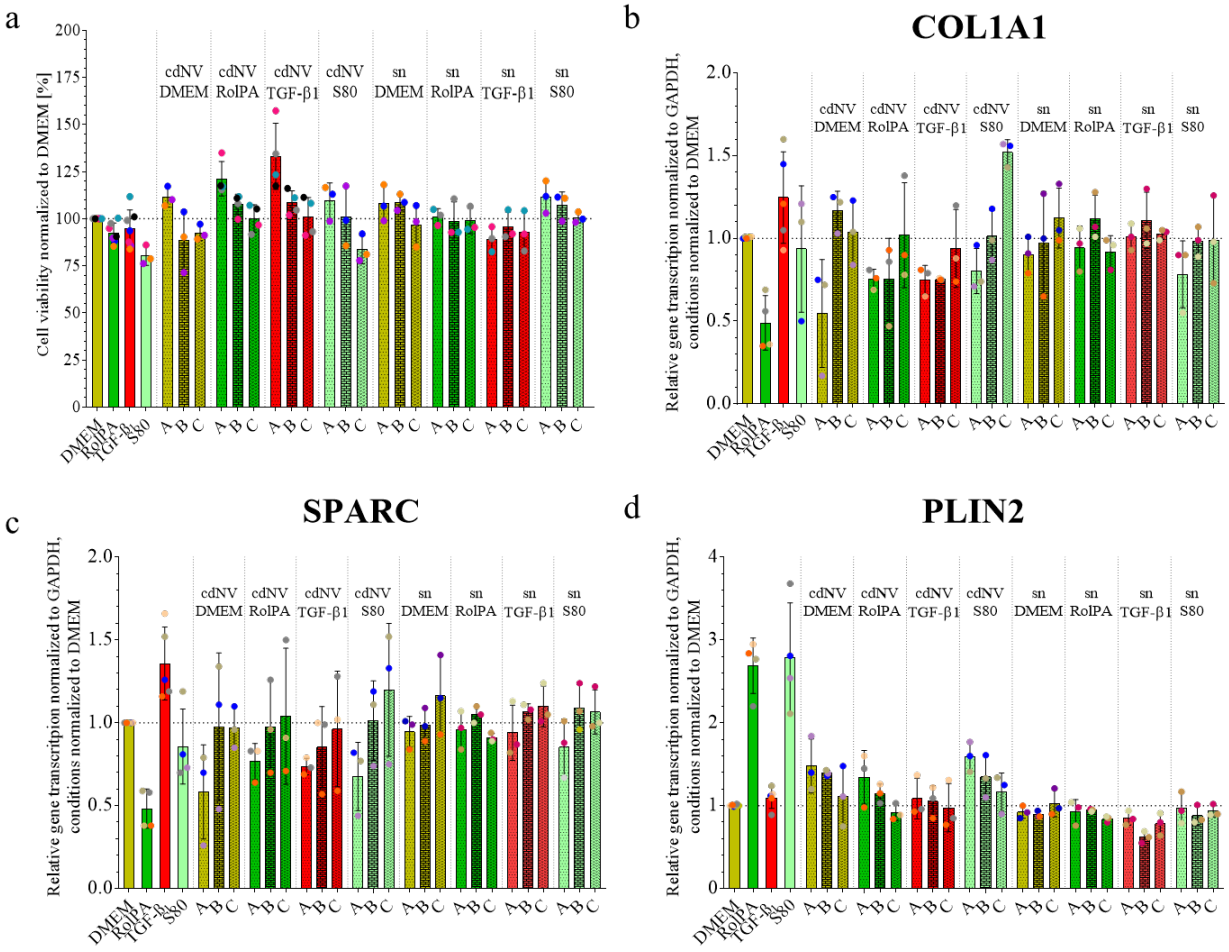

Figure 4.4. Effect of cdNVs and sn on TGF-β1 activated LX-2 cells.
a, Cell viability of activated LX-2 cells treated with three different cell-derived nanovesicles (cdNVs) concentrations (A = 1.5 x 10^{10} cdNVs/mL; B = 3.0 x 10^{09} cdNVs/mL; C = 6.0 x 10^{08} cdNVs/mL) derived from DMEM, RolPA, TGF-β_1, or S80 treated LX-2 cells (mean ± SD, n ≤ 3) and treated with the sn control kept during cdNV production (p-values from ordinary one-way ANOVA with post post-hoc Tukey test in supplementary table S6). **b, c, d,** Relative mRNA transcription in TGF-β_1 activated LX-2 cells of three fibrosis markers (COL1A1 (**b**), SPARC (**c**), PLIN2 (**d**)) normalized to GAPDH mRNA transcription and normalized to the DMEM condition after treatment with three different cdNV concentrations (A = 1.5 x 10^{10} cdNVs/mL; B = 3.0 x 10^{09} cdNVs/mL; C = 6.0 x 10^{08} cdNVs/mL) and three different sn protein concentrations (A = 20 µg/mL; B = 4.0 µg/mL, C = 0.8 µg/mL) derived from DMEM, RolPA, TGF-β_1, or S80 treated LX-2 cells (mean ± SD, n ≤ 3) (p-values from ordinary one-way ANOVA with post post-hoc Tukey test in supplementary tables S7/8/9).

mRNA levels respectively compared to DMEM treated naïve LX-2 cells (**Figure 4.3c**). PLIN2 mRNA levels barely changed, consistently with a study performed by O'Mahony et al. in 2015 showing that PLIN2 levels remain constant upon LX-2 activation.[169] The results show a dose-dependent translational change of all tested fibrosis-specific genes for cdNVs derived from all differently treated LX-2 cells (**Figure 4.4b, c, d**). The response is weakened upon dilution of cdNVs till to the C dilution that drove no change in translation of the three investigated markers, except for the lowest dose of cdNV_S80, which led to further perpetuation of the TGF-β_1 activated LX-2 cells by increasing COL1A1 mRNA translation 50% and increasing SPARC mRNA translation 20% (no significant difference to other cdNV_C samples by ordinary one-way ANOVA). The most pronounced effect of all tested cdNV samples was observed in cdNV_DMEM_A, however with a big standard deviation making it not significantly different from the other cdNV_A treatments. All cdNV samples led to a smaller change in translation of the three tested markers compared to direct RolPA treatment with the biggest difference in PLIN2 mRNA transcription. On the other hand, treatment with 1.5 x 10^{10} cdNVs/mL (cdNV_A) led to a more pronounced decrease in SPARC and COL1A1 mRNA expression compared to direct S80 treatment. Even the PLIN2 mRNA transcription of perpetuated LX-2 cells after treatment with S80 liposomes was not more enhanced than treatment with cdNVs if the same particle concentration was administered (**Figure A4.4.**), except for cdNV_TGF which did not lead to an increase in PLIN2 mRNA transcription. No investigation in the translation of PLIN2 mRNA to ADRP protein was done, still those results suggest that the anti-fibrotic effect of cdNVs on LX-2 cells is not or only partially driven by ADRP and lipid droplet formation, which was shown by Friedman et al. in 2010 to be an important driver in fibrosis resolution of HSCs[54]

Direct S80 treatment, as well as direct RolPA treatment led to a 2.7-fold increase in PLIN2 mRNA translation. Still, RolPA treatment led to a bigger decreased in COL1A1 and SPARC mRNA level compared to S80 treatment (51% vs 4% for COL1A1 mRNA and 52% vs 14% for SPARC mRNA). Those results suggest different mechanisms responsible for fibrosis resolution after RolPA or S80 treatments respectively. While direct RolPA treatment induced the same relative change in mRNA translation of COL1A1, SPARC and PLIN2 in naïve and TGF-β_1 activated LX-2 cells, direct S80 treatment did show a smaller effect on TGF-β_1 activated LX-2 cells (24% to 4% decrease for COL1A1 mRNA and 27% to 14% decrease for SPARC mRNA) (**Figure 4.3c and Figure 4.4b**) suggesting that the anti-fibrotic response of S80 is lower in perpetuated LX-2 cells compared to naïve LX-2 cells. However, over 150 HSC markers[170] are involved in fibrosis and therefore only looking at the full transcriptome and proteome could give a clear answer on the activity of S80 liposomes in liver fibrosis.

The sn samples showed a very small transcriptional change on the three tested markers in activated LX-2 cells for the highest tested concentration, which tended to turn in a pro-fibrotic direction upon dilution, proving the presence of active molecules in the sn. Only on PLIN2 mRNA expression no beneficial effect was observed after treatment with the highest tested sn concentration. This indicates that the addition of specific lipids through the cdNV membrane had an influence on the PLIN2 expression, whereas the decrease of COL1A1 and SPARC could have been triggered more by the non-lipidic fraction present in the sn and in the cdNV sample. To test if this hypothesis is correct, extracted lipids from cdNVs with the Bligh and Dyer total lipid extraction protocol (see Material and Methods).

4.3.4. Treatment of TGF-β_1 activated LX-2 cells with liposomes composed of lipids extracted from cell-derived nanovesicles derived from DMEM, RolPA, S80 or TGF-β_1 treated LX-2 cells

After extracting lipids from cdNVs, lipid films were formed by evaporating the organic solvent under nitrogen gas. Liposomes were formed by simple rehydration of the lipid films in 10 mM HEPES for characterization experiment and in FBS-free high glucose DMEM for activity studies and named cdNV-liposomes (cdNV-L). The formed cdNV-L showed a more negative zeta potential, suggesting a charge masking effect on cdNVs through its membrane composition and surface corona (**Figure 4.5a**). During lipid extraction, 93.5% ± 8.7% of all protein was removed indicating cdNV-Ls that are almost purely composed of lipids (**Figure 4.5b**). As the rehydrated lipids were neither freeze/thawed nor extruded but simply sterile filtered, they displayed an increase in hydrodynamic diameter compared to cdNVs (**Figure 4.5c**), explaining the average PDI increased from 0.15 ± 0.03 for cdNVs to 0.26 ± 0.05 for the liposomes.

The effect of the cdNV-L on TGF-β_1 activated LX-2 cell viability was evaluated in a dose-dependent manner using the same three concentrations A, B, and C (A = 1.5 x 10^{10} cdNV-L/mL; B = 3.0 x 10^{09} cdNV-L/mL; C = 6.0 x 10^{08} cdNV-L/mL) used above. The treated LX-2 cells hardly showed a change in cell viability after treatment with all cdNV-L tested conditions (**Figure 4.5d**), proving that the increase in cell metabolism after treatment with the highest cdNV concentration depended not only on the lipids but on the entire cdNV corona, cdNV content and cdNV membrane composition. Further the potency of cdNV-Ls was studied by investigating the expression of the same three qPCR targets (COL1A1, SPARC, PLIN2) upon treatment of proliferated LX-2 cells.

The tested cdNV-L conditions did not influence the COL1A1 mRNA transcription, except for cdNV-RolPA-L which led to a slight increase (not significantly different to DMEM control or

other cdNV-L treatments (Ordinary one-way ANOVA)) (**Figure 4.5e**). The SPARC mRNA translation was increased by 20% after all cdNV-L treatments. However, no concentration dependence was observed, suggesting that low amounts of extracted lipids led to a SPARC transcription increase which plateaus at an increase of roughly 20%. Only the PLIN2 mRNA transcription suggested that the treatment with cdNV-L could result in a genotype with reduced fibrotic features. The cdNV-Ls led to a concentration-dependent increase in PLIN2 mRNA levels, similar to what observed with cdNVs. The difference in PLIN2 mRNA increase observed between the different treatments (cdNV-DMEM-L/cdNV-S80-L ~20% increase, cdNV-RolPA-L/cdNV-TGF-L ~50% increase) might be explained by the LX-2 cells used for the specific experiments, as not all treatments were performed on the same set of cells. Direct S80 treatment showed highest PLIN2 mRNA transcription in the replicate which represents the cells used for cdNV-RolPA-L and cdNV-TGF-L treatments, and less high PLIN2 levels in the replicates which represents the cells used for cdNV-DMEM-L and cdNV-S80-L treatments.

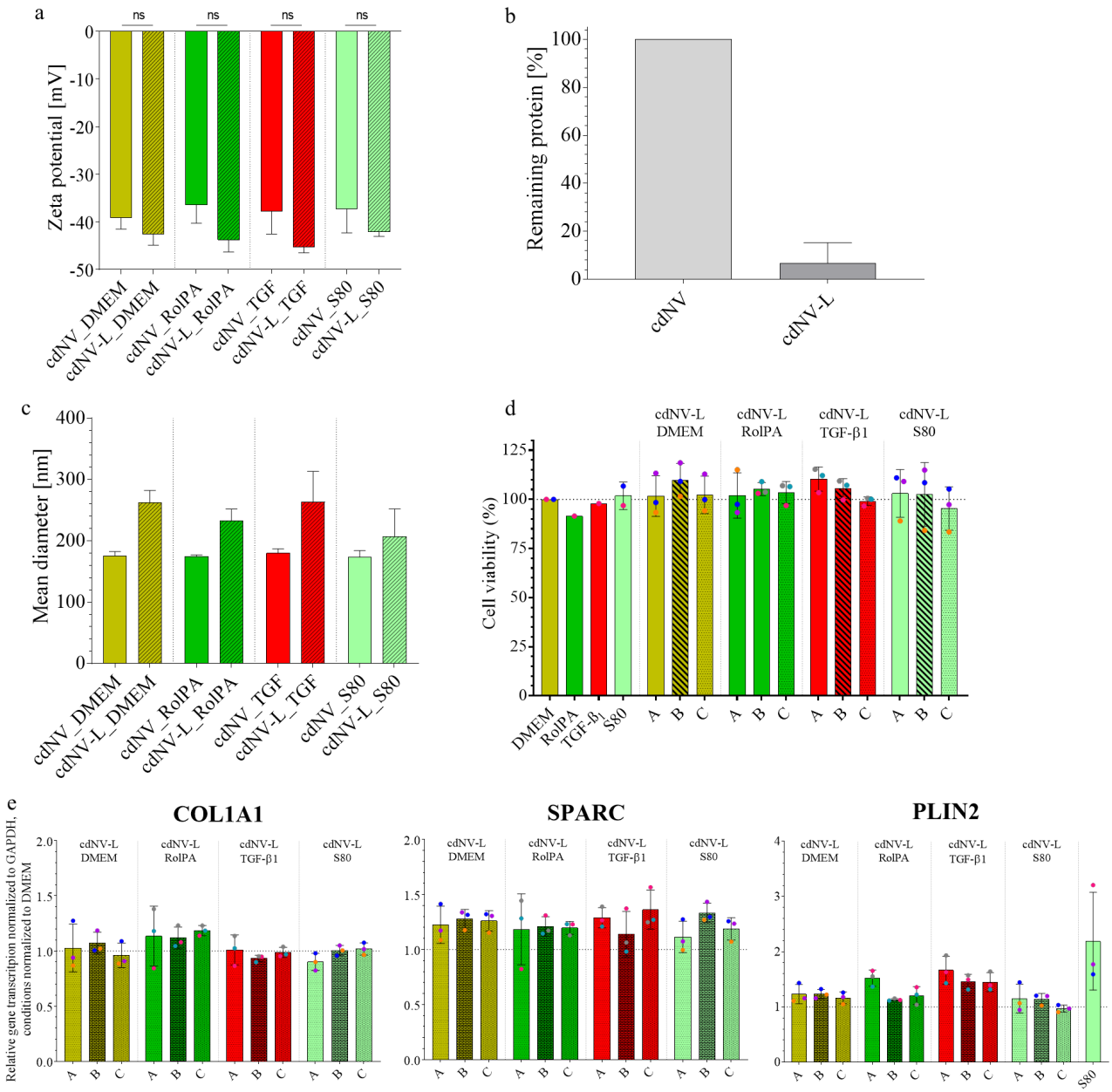

Figure 4.5. Characterization and activity of liposomes derived from cdNV extracted lipids. **a,** Zetapotential of cell-derived nanovesicle (cdNV) liposomes (cdNV-L) compared to cdNVs (mean ± SD, n = 3). **b,** Protein removal during the lipid extraction procedure (mean ± SD, n = 6). **c,** Hydrodynamic diameter comparison of cdNVs with cdNV-L (mean ± SD, n ≤ 3). **d,** Cell viability of activated LX-2 cells treated with three different cdNV-L concentrations (A = 1.5 x 10^{10} cdNV-L/mL; B = 3.0 x 10^{09} cdNV-L/mL; C = 6.0 x 10^{08} cdNV-L/mL) (mean ± SD, n = 3) **e,** Relative mRNA transcription in TGF-β_1 activated LX-2 cells of three fibrosis markers (COL1A1, SPARC, PLIN2) normalized to GAPDH mRNA transcription and normalized to the DMEM condition after treatment with three cdNV extracted lipid liposome concentrations (A = 1.5 x 10^{10} cdNV-L/mL; B = 3.0 x 10^{09} cdNV-L/mL; C = 6.0 x 10^{08} cdNV-L/mL) (mean ± SD, n = 3).

Taken together, the results from treatments with extracted lipids from cdNV suggest that the lipid component of the vesicles only exerts an effect on lipid droplets formation, as proven by the increase in PLIN2 mRNA. We cannot exclude that the increase in PLIN2 mRNA upon cdNV-L treatment was not enough to raise the ADRP to a level where it induces, according to a mechanism still to be understood, a decrease in ECM as described by Friedman et al. in 2010.[54] Hence, the non-lipid membrane components, such as membrane proteins, the membrane structure, as well as potentially the cdNV content, play an important role in the modulation of trans-differentiation of HSCs induced by cdNVs. Additionally, the cdNV might be beneficial by simply offering a membrane surface for soluble factors, as well as hydrophobic molecules, to form a functional corona, which leads to functional changes in a recipient cell, as described in previous studies.[171, 172]

4.3.5. Treatment of TGF-β_1 activated LX-2 cells with proteoliposomes formed through reconstitution of soluble factors on the cdNV-Liposome surface

To address the effect of protein corona on the activity of cdNVs, reconstituted the soluble factors of the sn on cdNV-Ls by incubation for 1 h at 37 °C in FBS-free DMEM medium. The sn and cdNV-L were derived from DMEM treated LX-2 cells and the formed particles were termed proteoliposomes (PL). The sn and cdNV-L concentrations were chosen to form PLs with the same protein amount per particle as for cdNVs (**Table A4.1.**). Also tested proteoliposomes with 200 µg/mL of protein on 1.5 x 10^{10} cdNV-L/mL termed PL_200. A concentration of 200 µg/mL protein was used, as an increase of the protein amount in sn led to an increased fibrosis resolving activity, even though the linear correlation was not as high as for cdNVs high (**Figure A4.5a, b**). Physicochemical characterization of the PL and PL_200 samples by NTA did not show a difference in the size distribution compared to cdNV-Ls (**Figure A4.6.**). On the other hand,

addition of soluble factors on the cdNV-L surface lowered the surface charge (**Figure 4.6a**). The zeta potential of PLs was less negative compared to cdNV-L, even though not significant (Ordinary one-way ANOVA), restoring the surface charge values measured for cdNVs (~-40 mV). Addition of more proteins further decreased the surface charge to -22 mV for PL_200 (Ordinary one-way ANOVA, p-value = 0.0001 vs cdNV-L, p-value = 0.0005 vs PL).

Cell viability studies showed that none of the tested protein and particle concentrations in the sn and PL samples had an influence on the cell metabolism (**Figure 4.6b**). Hence, the observed concentration dependent increase in cell viability after treatment with cdNVs (**Figure 4.6a**) must be influenced not just by a corona but by its composition and structure, as well as other membrane components which are not present in the sn. Addition of sn or PL did not significantly change the expression of COL1A1, SPARC and PLIN2 mRNA transcription in perpetuated LX-2 cells compared to DMEM treatment (**Figure 4.6c**). However, the increase in SPARC mRNA transcription that was observed after cdNV-L treatment was not observed in PL, hinting to a beneficial effect coming from the protein corona. PL did not show the same increase in PLIN2 mRNA transcription as observed after cdNV-L treatment.

On the other hand, sn_200, as well as PL_200 did lead to an anti-fibrotic response of perpetuated LX-2 cells upon treatment (**Figure 4.6d**). COL1A1 mRNA transcription was decreased by 20% after PL_200 treatment which was almost as much as observed after cdNV treatment. The treatment with sn_200 did not change the COL1A1 mRNA transcription. Howbeit, SPARC mRNA transcription was decreased by 40% after PL_200 and sn_200 treatment, which was a more enhanced decreased than obtained after cdNV treatment (Ordinary one-way ANOVA, PL_200 vs. cdNV_A p-value = 0.0486; sn_200 vs. cdNV_A p-value = 0.0566). The PLIN2 mRNA did not increase after sn_200 treatment but almost 30% after PL_200 treatment because of the addition of

lipids through the cdNV-L in PL_200. Hence, the anti-fibrotic potential in the sn can be enhanced with the presence of lipid particles due to the formation of a protein corona on the particles leading to a synergistic effect of proteins and vesicles.

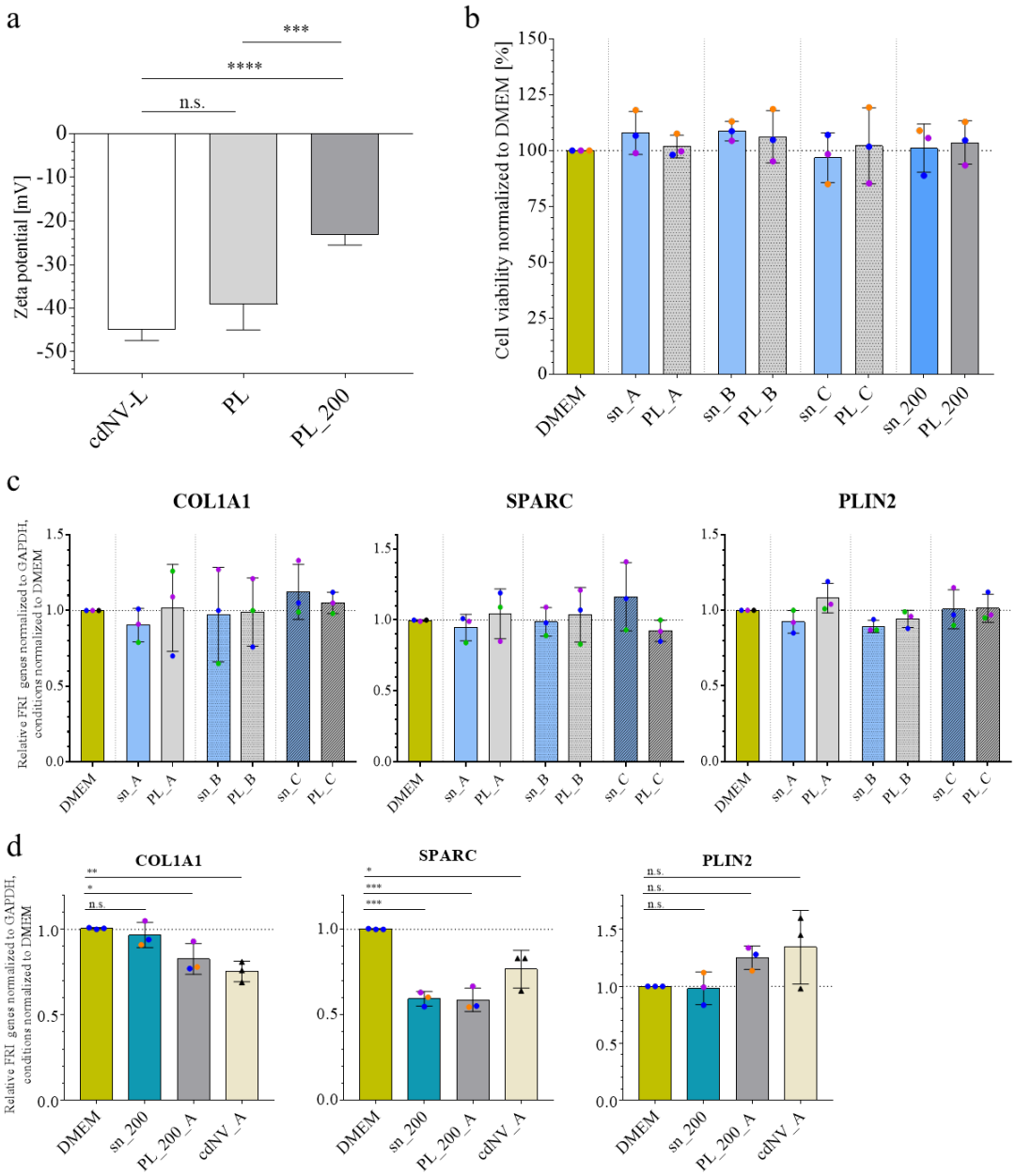

Figure 4.6. Characterization and activity of proteoliposomes.
a, Zeta potential of cdNV-L compared to PL and PL_200 (mean ± SD, n = 6) (p-values from ordinary one-way ANOVA with post post-hoc Tukey test in supplementary table S10). **b,** Cell viability of activated LX-2 cells treated with three different PL concentrations and the corresponding sn (A = 1.5 x 10^{10} cdNV-L/mL + 20 µg/mL; B = 3.0 x 10^{09} cdNV-L/mL + 4.0 µg/mL; C = 6.0 x 10^{08} cdNV-L/mL + 0.8 µg/mL) and PL_200 and the corresponding sn (A = 1.5 x 10^{10} cdNV-L/mL + 200 µg/mL) (mean ± SD, n = 3) **c,** Relative mRNA transcription in TGF-β_1 activated LX-2 cells of three fibrosis markers (COL1A1, SPARC, PLIN2) normalized to GAPDH mRNA transcription and normalized to the DMEM condition after treatment with the same three PL concentrations and the corresponding sn (mean ± SD, n = 3). **d,** Relative mRNA transcription in TGF-β_1 activated LX-2 cells after treatment with PL_200 and the corresponding sn (mean ± SD, n = 3) (p-values from ordinary one-way ANOVA with post post-hoc Tukey test in supplementary tables S11/12).

4.3.6. Cellular uptake of particles

Even though controversial, there is evidence of homing function in EVs due to their natural tropism.[77, 173, 174] Artificial EVs have been previously described to preserve the targeting capacity of natural EVs.[88, 90] To evaluate if cdNVs show an enhanced uptake in LX-2 cells and to determine whether it is attributed to the membrane components and structure, a comparison was made between the uptake of cell-derived nanovesicles (cdNV), liposomes formed from cdNV extracted lipids (cdNV-L), proteoliposomes formed by incubation of cdNV-L with sn (PL), and proteoliposomes with 200 μg/mL proteins (PL_200) by LX-2 cells after 24 h. The particles were labelled with the hydrophobic nonexchangeable dye DiR and the uptake was measured via flow cytometry. The labelling efficiency with the hydrophobic dye was similar between cdNV and cdNV-L with encapsulation efficiencies of 65-70% (**Figure 4.7a**). After 24 h cdNV showed an almost 3-fold higher uptake in naïve LX-2 cells compared to cdNV-L (**Figure 4.7b**).

Addition of proteins on the cdNV-L surface did not increase the particle uptake. Hence, the increased particle uptake observed in cdNVs must be due to a specific surface corona and membrane proteins. Glycosylation of the cdNV membrane should not be neglected as it might play an important role in the enhanced uptake. Glycosylation was shown to be involved in interactions of EVs with cell surfaces and represent the first contact points of cells with particles.[175] If the LX-2 cells were perpetuated with TGF-β_1 prior cellular uptake experiments, an enhanced uptake was observed for all particles even though it was not significantly different compared to naïve cells (**Figure 4.7b**). The reason for the observed enhancement of uptake in highly active LX-2 cells compared to mildly activated naïve cells remains unknown. Since all particles demonstrated an increased uptake, it is possible that this may not be a specific mechanism and therefore could be due to a slight increase in membrane fluidity after TGF-β_1 treatment.[45] Additionally, flow

cytometry cannot discriminate between internalized particles and particles adsorbed to the cell surface. Addition of proteins to the cdNV-L surface initially decreased the cellular uptake in perpetuated LX-2 cells before increasing it again. Those observed uptake results correlate with the observed increase in PLIN2 mRNA transcription after treatment of perpetuated LX-2 cells (**Figure A4.1b**). Even though the PLIN2 mRNA expression changes were not significant and not as enhanced as the cellular uptake changes, it shows that for lipid droplet formation lipids have to be taken up and internalized.

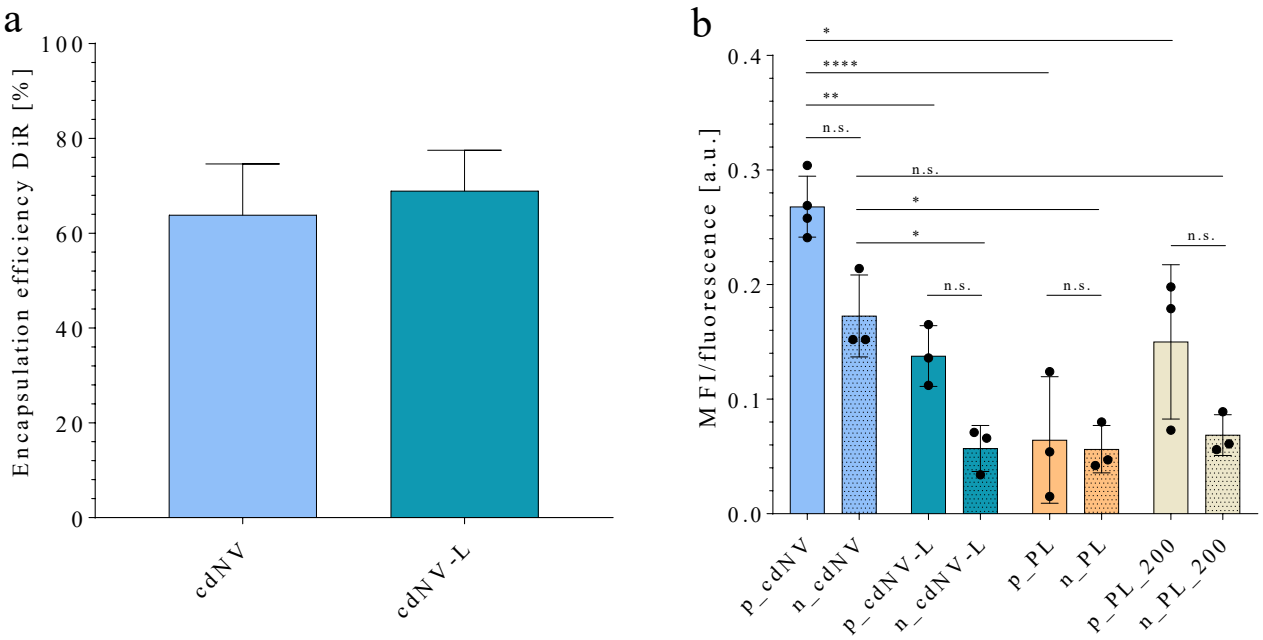

Figure 4.7. Cellular particle uptake.
a, Encapsulation efficiency of the hydrophobic DiR-dye in cell-derived nanovesicles (cdNVs) and cdNV liposomes (cdNV-L) (mean ± SD, n = 6). The encapsulation efficiency was calculated by division of the fluorescent intensity of the particles after removal of free drug by size exclusion chromatography (SEC) by the fluorescent intensity of the particles prior SEC. **b,** Cellular uptake of cdNVs, cdNV-Ls, proteoliposomes with low protein amount (PL), and proteoliposomes with high protein amounts (PL_200) in naïve (n) and perpetuated (p) LX-2 cells analysed by flow cytometry. LX-2 cells were seeded on 12-well plates at 1.2×10^5 cells/well. DiR-labelled particles were added to the cells at 4.2×10^4 particles/cell concentration and incubated at 37 °C for 24 h. The fluorescence intensity was measured using a flow cytometer to determine the uptake efficiency and the mean of all positive cells was normalized to the fluorescence of the particles (MFI/fluorescence) (mean ± SD, n ≤ 3) (p-values from ordinary one-way ANOVA with post post-hoc Tukey test in supplementary table S13).

4.4. Discussion and Conclusion

We described a method to generate and purify cell-derived nanovesicles from untreated, quiescent, and fibrotic LX-2 cells. The purification, involving density-gradient ultracentrifugation on an iodixanol cushion followed by ultracentrifugation removed over 95% of the proteins while preserving 40% of all cdNV particles. Still a big variation in particle yield was observed which originated from the variability obtained after extrusion showing an improvement potential at the formation step. Introduction of a pre-lysis, such as through sonication or freeze/thawing could be beneficial to facilitate extrusion. Also, the addition of more extrusion cycles, as well as extrusion through membranes with smaller pores should be considered, as it has already successfully been done by other groups.[90, 99, 101] TEM microscopy, as well as physicochemical characterization, revealed a spherical shape of the particles with a nano ranged diameter and narrow size distribution. The cdNVs derived from all tested conditions induced a concentration-dependent phenotypical change in naïve and TGF-β_1 activated LX-2 cells, restoring parts of the lost lipid droplets, and decreasing COL1A1, as well as SPARC mRNA transcription, whereas no pre-treatment specificity was observed. This led us to believe that the de-activation of LX-2 may be induced from molecules that are unaffected by the pre-treatment and not from nucleic acids or proteins/peptides that are expressed only after a specific pre-treatment.

Liposomes formed with extracted lipids from cdNV (cdNV-L) revealed that the lipids were not the reason for the decrease in COL1A1 and SPARC mRNA expression, but that they play an important role, through a mechanism yet to be understood, in the formation of new lipid droplets and the increase in PLIN2 mRNA transcription. Proteoliposomes were successfully formed by incubation of the supernatant, containing soluble factors, with cdNV-L, as shown by the decrease in zeta potential. Restoring the same number of proteins on cdNV-L as present in cdNV did not

restore any anti-fibrotic activity. However, increasing the protein amount further up to 200 µg/mL recovered fibrosis-resolving potential, showing a synergistic effect of particles and soluble factors. Further studies are needed to fully understand the role of lipids and proteins in the trans-differentiation of activated LX-2 cells to a less active state, as the proteins in the sn and the proteins in/on the cdNV membrane are not necessarily the same. Additionally, the membrane composition and structure might also play an important role in the activity of cdNVs which is totally lost upon cdNV-L formation. Therefore, the purification process needs to be selected wisely, as it has an influence on the soft particle corona.[171] There needs to be a prioritization of functionality over purity, as discussed by the International Society of Extracellular Vesicles in 2022, as long as safety guidelines on GMP by the FDA and efficacy can be guaranteed.[176] Additionally, a switch from harsh purification techniques such as ultracentrifugation to more gentle and scalable techniques, such as tangential flow filtration (TFF) needs to progress, which already started in the EV and EV-mimetic field.[90, 177, 178]

Cellular uptake studies revealed that the cdNV membrane composition plays an integral role. Forming cdNV-Ls showed an almost 50% decreased uptake in perpetuated LX-2 cells compared to cdNVs, reflecting the different response observed on the expression of PLIN2 mRNA. Addition of proteins on the cdNV-L surface did not increase the particle uptake, but even decreased it with small protein concentrations. The particles were preferentially internalized by highly active HSCs, providing an advantage as these cells are the primary target for fibrosis resolution.

Our results show the possibility to form, out of LX-2 cells, nanoparticles with antifibrotic potential and enhanced uptake in fibrotic LX-2 cells. The vesicles are presenting a functional corona to the perpetuated cells proving a synergistic effect of lipid particles and corona. However, to achieve a complete and thorough comprehension of the cdNVs further investigations will be

needed on the treated cells, nanoparticles as well as sn, which should mostly reflect the LX-2 cytosol. One important aspect is to assess if cdNV-treated LX-2 cells remain less active over time and if they can be further deactivated by repeated doses. To understand if the cdNVs would show an increased uptake in activated LX-2 cells in presence of other cell types, especially hepatocytes and Kupffer cells, co-culture models and/or *in vivo* models need to be considered. *In vivo* tests do not only reveal if a homing effect is preserved in cdNVs but if a low immunogenicity, and therefore an extended half-life in circulation is observed.

In conclusion, we believe that our research, helps understanding bio-derived vesicles and contributes to the field of personalized medicine against liver diseases, which we believe is an important approach against liver fibrosis with the potential to positively impact millions of individuals globally and alleviate the rising demand for liver transplantation procedures.

4.5. Experimental Section

4.5.1. Liposome preparation

Liposomal formulations with soybean phospholipids with 75% phosphatidylcholine (S80; Lipoid, Germany) were prepared by the thin film hydration method. The calculated amount of lipids was weighed and dissolved with chloroform (Biosolve, Netherlands) in a round bottom glass flask. The organic solvent was evaporated under N_2 stream and the lipid film was dried overnight in a desiccator. The lipid film was then rehydrated with 10 mM HEPES (Carl Roth, Germany) and extruded 10 times through a 0.2 µm polycarbonate membrane (Sterlitech, USA) with a LIPEX extruder (Evonik, Canada). The particles' size distribution (polydispersity index, PDI) and hydrodynamic diameter were measured using a Litesizer 500 (Anton Paar, Austria).

4.5.2. Cell culture

LX-2 cells were cultured in high glucose (4.5 g/L) DMEM (Carl Roth, Germany) supplemented with 10'000 units/L of penicillin and streptomycin (P/S; Gibco, USA), 200 mM L-Glutamine (Sigma, USA), and 2% (v/v) of sterile filtered (0.2 µm, cellulose acetate membrane) fetal bovine serum (FBS; Merck Millipore, USA) at 37 °C in a humidified atmosphere containing 5% CO2. The cells were treated with 10 µM retinol (Merck Millipore, USA) and 300 µM palmitic acid (RolPA; Merck Millipore, USA), 10 ng/mL TGF-β_1 (BioVendor, USA), or 5 mM S80 liposomes in serum-free DMEM for 24 h. After treatment, the cells were detached with 2 mL Accutase® (Merck Millipore, USA) per flask and incubated for 4 min at 37 °C.

4.5.3. Cell-derived nanovesicle formation

(Pre-treated) LX-2 cells were washed with pre-heated (37 °C) PBS (Carl Roth, Germany) and were detached as described above. The total cell amount was counted mixing a small aliquot 1:1 with trypan blue (Thermo Fisher Scientific, USA) and a 0.100 mm Neubauer chamber (Hecht Assistant, Germany). LX-2 cells were washed by discarding the supernatant after centrifugation for 3 min at 500 g. The pellets were resuspended to reach a desired concentration between 1 – 10 x 10^6 LX-2/mL with fresh PBS. LX-2 cells were extruded serially 5 times through a 10 µM, 5 µM and 1 µM polycarbonate membrane (Sterlitech, USA) with a LIPEX extruder. The formed cdNVs were stored on ice till further procedure.

4.5.4. Cell-derived nanovesicle purification

In a thick wall 10 mL PC centrifugal tube (Beckman Coulter, USA), 1 mL of cold (4 °C) 10% (w/v) iodixanol (Alere Technologies AS, Norway) was stacked on top of 1 mL cold 50% (w/v) iodixanol. Then, a cdNV solution (5 mL) was carefully pipetted on top of the iodixanol sandwich by holding the tube almost flat (75°) while pipetting. The tubes were centrifuged for 1 h at 4 °C

and 100’000 g in an Optima L-90K Ultracentrifuge (Beckman Coulter, USA), and 1 mL fractions were collected in pre-cooled Axygen reaction tubes (Corning, USA). The cdNV fractions were mixed, diluted to 8 mL with PBS, and ultracentrifuged for 2.5 h at 4 °C with a speed of 140’000 g. The supernatant (sn) was enriched using a 10’000 MWCO Amicon Ultra-4 Centrifugal Filter Unit (Merck Millipore, USA), and the pellet was resuspended in FBS-free DMEM and sterilized by filtration through a 0.22 µm regenerated cellulose (RC) syringe filter (ThermoFisher, USA) after being vigorously vortexed and pipetted. Nanoparticle tracking analysis (NTA, ZetaView 8.05.05 SP2, Particle Metrix, Germany; Sensitivity: 70.0; Shutter: 100) was used to determine size distribution, yield, and zeta potential of cdNVs. The protein content was measured using a micro-BCA protein assay kit (ThermoFisher, USA) following the manufacturer’s instructions, and RNA content was measured using a Nanodrop (ThermoFisher, USA).

4.5.5. Transmission electron microscopy (TEM)

TEM was performed by the Microscopy Imaging Centre (MIC) of the University of Bern. Briefly, for imaging of negatively stained samples, 5 µL of the vesicle suspension was adsorbed on glow discharged and carbon coated 400 mesh copper grids (Plano, Germany) for 3 minutes. Grids were washed and stained with 2% uranyl acetate in water (Electron Microscopy Science, Switzerland) for 45 s. The excess fluid was removed by gently pushing them sideways to filter paper. Samples were then examined with a transmission electron microscope (Tecnai Spirit; FEI, USA) at 80 kV and equipped with a digital camera (Veleta; Olympus Life Science, Germany).

4.5.6. General design of cell assays

LX-2 cells were seeded in cell culture plates in high glucose DMEM supplemented with 10’000 units/L of P/S, 200 mM L-Glutamine, and 2% (v/v) FBS. After 18 h the medium was discarded and cells were washed with PBS. Either treatments were performed for 24 h directly on naïve LX-

2 cells in FBS-free medium, or the fibrotic LX-2 cells were perpetuated with 10 ng/mL TGF-β_1 for 24 h prior the treatments.[179]

4.5.7. Quantitation of viable cell number in cytotoxicity assays

10'000 LX-2 cells were seeded in a 96-well plate (Faust, Switzerland). The CCK-8 assay (Merck Millipore, USA) was used to determine cell viability following the manufacturer's instructions. Briefly, the cells were washed after treatment with PBS and 90 µL FBS-free medium + 10 µL CCK-8 solution was added to each well. After further 2 h of incubation at 37 °C and 5% CO_2, the absorbance at 450 nm was measured with a plate reader (Infinite MNanof; Tecan, Switzerland). The cell viability was calculated with following equation:

$$Cell\ viability\ [\%] = \frac{OD_{treatment}}{OD_{DMEM}} * 100$$

where "OD treatment" refers to the optical density of the LX-2 cells treated with the specific treatment and "OD DMEM" refers to the optical density of LX-2 cells treated with the vehicle (FBS-free DMEM).

4.5.8. Lipid droplet content analysis

30'000 LX-2 cells were seeded in a 48-well plate (Faust, Switzerland) and the lipid droplet analysis was performed as described before with slight adjustments[45]. Briefly, the treated cells were washed and fixed with 200 µL/well Roti®-Histofix 4% (Carl Roth, Germany) for 10 min at RT, and washed once with 1 mL/well deionized MilliQ water. LX-2 cells were stained with 200 µL/well of a filtered (0.45 µm, PVDF; Merck Millipore, USA) Oil Red O (ORO, 0.5% w/v; Merck Millipore, USA) solution in propylene glycol for 15 min at RT. The remaining ORO was removed and cells were washed twice with PBS. Nuclei were counterstained with 200 µL/well of a 4 µM DAPI solution (ThermoFisher, USA) in PBS for 5 min at RT. Afterwards, cells were rinsed with

PBS and acquired phase contrast (bright field, BF) as well as fluorescent images using an inverted Nikon Ti-U microscope (Nikon Instruments, Japan) equipped with a Plan Fluor DL WD 15.2 10x, with a numerical aperture of 0.3 (Nikon instruments, Japan), DAPI filter (ex 360, em 460, 100 ms exposure) and Texas Red filter (ex 560, em 645, 300 ms exposure).

The fluorescent binary area and the cell count were performed with the open-source FIJI software using a script. The fluorescent binary area was then divided by the cell count to analyse how much lipid droplets [μm^2] per cell are present.

4.5.9. mRNA transcription

In a 24-well plate (Faust, Switzerland) 60'000 LX-2 cells were seeded. After treatment total RNA was isolated using TRIzol reagent (ThermoFisher, USA) following the manufacturer's instructions. Briefly, cells were lysed with TRIzol (ThermoFisher, USA) directly in the plate and transferred them to Axygen reaction tubes (Corning, USA). A volume of chloroform equivalent to one-fifth of the total TRIzol volume was added to the samples. The tube was vortexed vigorously for 10 sec and was incubated at room temperature for 10 min., before being centrifuged for 20 min at 4°C and 16'000 g with a Hermle Z 366 K centrifuge (Faust, Switzerland). The upper phase was transferred to a new reaction tube and 1 µL glycogen (Merck Millipore, USA) as well as 1 volume of isopropanol (Biosolve, Netherlands) was added, prior RNA precipitation on ice for 10 min. the RNA was pelleted by centrifugation for 10 min at 4 °C and 24'000 g. The supernatant was discarded, and the pellet was washed with 1 mL 70% EtOH in DEPC-treated MilliQ-water (Carl Roth, Germany). The centrifugation was repeated twice and the final pellet was resuspended in DEPC-treated MilliQ-water. The RNA concentration was measured with a NanoDrop (ThermoFisher, USA).

The isolated RNA was reverse transcribed into cDNA. Briefly, 1000 ng of RNA were diluted in DEPC-treated MilliQ-water and were incubated for 5 min at 65 °C after addition of 3 µL of a 150 ng/µL random hexamer (Microsynth, Switzerland). After 10 min incubation at RT 13.5 µL of pre-mixed master mix was added (**Table 4.1.**) and the samples were incubated for another 10 min at RT, followed by a 1 h incubation at 50 °C and 20 min incubation at 75 °C. DEPC-treated MilliQ-water was added to reach a theoretical concentration of 8 ng/µL cDNA.

Table 4.1. Reverse transcription master mix composition.

1x master mix			
reverse transcriptase buffer 10x	Agilent	5	µL
DTT 100 mM	Stratagene	5	µL
dNTPs 10 mM	ThermoFisher	2	µL
40 U/µL RiboLock RNase inhibitor	Fermentas	0.5	µL
reverse transcriptase 200 rxn	Agilent	1	µL
total volume		13.5	µL

Table 4.2. *Overview of the used primer pairs for qPCR.*

Primer	**Source**	**Sequence**
fwd GAPDH	Mühlemann	5'-GAG TCA ACG GAT TTG GTC G-3'
rev GAPDH	Mühlemann	5'-GAG GTC AAT GAA GGG GTC AT-3'
fwd PLIN2	OriGene, HP205000	5'-GAT GGC AGA GAA CGG TGT GAA G-3'
rev PLIN2	OriGene, HP205000	5'-CAG GCA TAG GTA TTG GCA ACT GC-3'
fwd COL1A1	Thermo, Hs00521314_CE	5'-GTT CAG TTT GGG TTG CTT GTC T-3'
rev COL1A1	Thermo, Hs00521314_CE	5'-CCT GCC CAT CAT CGA TGT G-3'

fwd SPARC	OriGene, NM_003118	5'-TGC CTG ATG AGA CAG AGG TGG T-3'
rev SPARC	OriGene, NM_003118	5'-CTT CGG TTT CCT CTG CAC CAT C-3'

The primers (**Table 4.2.**) were diluted in MilliQ to a primer pair solution of 2.5 µM of forward and reverse primer each. The remaining molecules (polymerase, nucleotides, buffer, fluorophore) for qPCR were in the Brilliant III Ultra-fast SYBR Green qPCR master mix (MM; Agilent, USA). The cDNA samples were measured in triplicates or duplicate for each gene and cDNA dilution. A water control was added to see potential contaminations of the reagents. A pipetting robot (Qiagen, Germany) was used to pipette the samples (3 µL cDNA, 7.5 µL 2x MM, 3 µL primer mix, 1.5 µL water). After the samples were ready, they were transferred into the qPCR analyser centrifuge (Qiagen, Germany) which performed 40 cycles of amplification at 95 °C and 60 °C, whereas the fluorescence was always measured at 60 °C (ex.: 470 nm, em.: 510 nm). After the 40 cycles a melting curve of each sample was measured. The data were analysed using the Rotor Gene Q software and excel. The qPCR data was analysed using the delta delta CT method[180]. GAPDH was used as a normalizer gene.

4.5.10. Lipid extraction

The LX-2 cells were pelleted and resuspended in 0.8 mL PBS before being transferred to a glass centrifuge tube with a Teflon cap. Ice-cold 1:2 (v/v) chloroform/methanol (Biosolve, Netherlands) was added (3 mL) and the tube was vigorously vortexed. After a 5 min incubation on ice, 1 mL of chloroform and 1 mL of PBS were added to the tube, mixed well, and centrifuged for 2 min at 1'000 g to induce phase separation. The lower phase was then collected with a Pasteur pipette and transferred into a round bottom glass flask. The organic solvent was evaporated under an N_2 stream and the lipid film was dried overnight in a desiccator. The lipid film was rehydrated in FBS-free

DMEM medium and the formed liposomes (cdNV-L) were sterilized by filtration through a 0.22 µm RC syringe filter. The cells were then treated with cdNV-Ls as described above. The size distribution and hydrodynamic diameter of the particles were measured using a Litesizer 500 (Anton Paar, Austria).

4.5.11. Protein corona reconstitution

Proteoliposomes (PL) with the same protein amount per particle as cdNVs or 10x more (PL_200) were formed by incubating cdNV-Ls with enriched supernatant collected during cdNV purification in PBS for 1 h at 37 °C. The formed PLs were then diluted in FBS-free DMEM medium to reach the desired particle concentrations. To determine the size distribution and zeta potential of PLs, nanoparticle tracking analysis (NTA, ZetaView 8.05.05 SP2-; Particle Metrix, Germany; Sensitivity: 70.0; Shutter: 100) was performed.

4.5.12. Cellular particle uptake

In the uptake studies, 120'000 LX-2 cells were seeded in a 12-well plate (Faust, Switzerland). DiR-labelled cdNVs and cdNV-Ls were prepared by incubating 5.0 x 10^{10} particles with 10 µM DiR (ThermoFisher Scientific, USA) in 2% (v/v) EtOH for 1 h at 37 °C. For the activated cells, the seeded cells were treated with 10 ng/mL of TGF-β_1 for 24 h before particle administration. Control particles were incubated with 2% (v/v) EtOH for 1 h at 37 °C. The labelled particles were purified from free drug using a PD MiniTrap Sephadex G-25 resin desalting column (Cytiva, USA) and normalized to their concentration using nanoparticle tracking analysis (Sensitivity: 70.0; Shutter: 100). PL and PL_200 were generated as described above and LX-2 cells were treated for 24 h in FBS-free DMEM medium with 4.2 x 10^4 particles/cell. The cells were detached with 100 µL Accutase/well for 5 min at 37 °C, and cell viability was determined with Pi staining. The fluorescent intensity of the cells was analyzed using FACS LSR II (BD, USA) and the mean of all

APC-Cy7 positive cells was normalized to the fluorescence of the particles that was measured with an Infinite® 200 PRO MNano plate reader (Tecan, Switzerland) after the particles were diluted 1:1 in MeOH (excitation 750 nm, emission 780 nm). The cells were washed with FACS buffer (PBS + 2% (v/v) FBS) before analysis. The results were analyzed with FlowJo software (version 10.8; BD, USA) and at least 20'000 events were recorded per sample using FCS (370 volt), SSC (240 volt), Pi (410 volt), and APC-Cy7 (360 volt) filters. The gating strategy used is described in the Supplementary information (**Figure A4.1a**).

4.5.13. Statistical analysis

Statistics were made with the software GraphPad Prism v. 7.05. If not stated otherwise, performed an ordinary one-way ANOVA test. If a significant difference was observed performed a post-hoc Tukey test comparing all groups. All p-values of post-hoc Tukey tests can be found under https://doi.org/10.5281/zenodo.7794261 (* represents p-value < 0.05; ** represents p-value < 0.01; *** represent p-value < 0.001; **** represents p-value < 0.0001).

Chapter 5.

Novel Liposomal Drug Delivery System for Peritoneal Disease: Entrapping Liposomes in hydrogel Beads to Control Release and Improve Efficacy

This chapter has been submitted for publication.

Remo Eugster, Aymar Abel Ganguin, Amirmohammad Seidi, Simone Aleandri, Paola Luciani

Pharmaceutical Technology Research Group, Department of Chemistry, Biochemistry and Pharmaceutical Sciences, University of Bern, Bern, Switzerland

Author's contribution

RE: Conceptualization; Investigation; Validation and Visualization; Formal analysis; Data curation; Writing of the original draft. AG: Conceptualization; Investigation; Visualization; Formal analysis; Data curation; Writing of the original draft. AS: Investigation; Validation. SA: Methodology. PL: Conceptualization; Supervision; Project administration; Funding acquisition.

All authors contributed to the interpretation of the data and to drafting and revising the manuscript.

5.1. Abstract

This study presents a method for reproducible production of biodegradable and biorthogonal hydrogel microbeads for intraperitoneal (IP) drug delivery, to overcome current limitations of fast clearance of small molecules and pharmacokinetic which have limited the utilization of IP administration. The system presented here uses additive manufacturing to entrap multilamellar vesicles (MLVs) and small unilamellar vesicles from synthetic and extracted phospholipids, avoiding rapid clearance of the lipid system. Gefitinib, a small hydrophobic anti-cancer pharmaceutical, was used as a model drug and was successfully encapsulated into MLVs entrapped into microbeads. A sustained release of gefitinib from microbeads for up to 3 days was demonstrated, and the microbeads induced concentration-dependent cell death in Huh-7 cells, an immortalized human hepatic cancer cell line, *in vitro*. These results demonstrate the potential of 3D-printed alginate microbeads for delivering a wide range of small hydrophilic and hydrophobic drug compounds into the peritoneum, overcoming previous limitations of IP injection.

Key words: intraperitoneal drug delivery, additive manufacturing, hydrogel microbeads, sustained drug release

5.2. Introduction

The peritoneal cavity is a space within the abdomen, bound by thin membranes, that contains the liver, the spleen, the stomach, and the intestines and therefore offers an attractive administration route to target diseases such as peritoneal carcinomatosis, endometriosis, and peritoneal fibrosis, which are challenging to treat with current drug delivery approaches[181]. However, it is hard to achieve a uniform drug distribution throughout the entire peritoneal space which potentially leads to subtherapeutic drug levels in target tissues[182]. This is mainly due to the high clearance observed in the peritoneum. Small drug compounds, as well as drug carriers such as liposomes with a size

below 1 µm are cleared very efficiently from the peritoneum through the lymph- and blood system[183]. More frequent dosage or higher dosage to overcome the limited drug distribution and high clearance rate only increases the risk of undesired side effects. Hence, new drug delivery approaches are needed for peritoneal administration, improving drug distribution, reducing side effects, and providing new therapeutic options for patients with peritoneal diseases.

When developing new drug delivery systems for the treatment of peritoneal diseases, several properties can enhance effectiveness and convenience for patients. Among these, a sustained drug release is of particular importance, as it enables long-lasting drug release, reducing the need for frequent or repeated administrations. Slowing down clearance is another crucial feature, as it allows for a higher concentration of the drug to remain in the peritoneal cavity, thereby improving treatment efficacy. A third important factor is a patient centric administration of the drug delivery system, such as delivery through a peritoneal port, injection, or post-surgery before suturing, to name a few.

Gefitinib is a small hydrophobic tyrosine kinase inhibitor that interrupts signaling through the epidermal growth factor receptor (EGFR), which is overexpressed in many types of cancer[184]. By binding EGFR, gefitinib can inhibit cancer cell proliferation and cancer survival. Hence, the drug has been approved for the treatment of non-small cell lung cancer (NSCLC) that show specific mutations in the EGFR gene[185]. Recent studies have shown the treatment potential of gefitinib for peritoneal metastasis from various cancer types, such as ovarian and gastric cancer, as well as the potential against peritoneal adhesions that are a common complication occurring after abdominal surgery[186]. Due to its hydrophobicity, small size, and relative long half-life gefitinib shows suitable properties for encapsulation into lipidic systems, enabling a sustained drug-

release[187]. Additionally, gefitinib has been shown to be well-tolerated barely leading to serious side effect according to clinical trials[188]. Because of those properties, as well as the fact that peritoneal metastasis and post-surgical adhesions are common complications of several types of cancer, gefitinib is a perfect drug candidate for the development of a new drug delivery platform in the peritoneum[104].

An extension of gefitinib presence in the peritoneum can be achieved by entrapping it into a gel scaffold. Among all available polymers alginate can be cross-linked with divalent cations, such as Ca2+ or Mg2+, which are both present in the peritoneal fluid at a concentration high enough to stabilize the biodegradable alginate-based hydrogels[189, 190].

Moreover, 3D printing has been identified as a suitable approach for formulating alginate hydrogels, due to its ability to create complex and precise structures with ease. It offers several advantages in drug development, including the ability to create customized drug delivery systems, faster prototyping, and reduced cost. With 3D printing, drug prototypes can be developed more quickly and efficiently, allowing for faster iterations and improvements to the drug design. The technology also enables the creation of complex drug delivery systems, such as microbeads which can improve, ultimately leading to better patient outcomes.

To produce a drug delivery platform for peritoneal applications, encapsulated gefitinib in several liposome types were mixed with an alginate solution to form an ink. This ink was used for the formation of micro-size hydrogel beads by 3D printing using an electromagnetic droplet (EMD) printhead which enables drop-on-demand formation. Additive manufacturing enables reproducible and scalable hydrogel production. The formed hydrogel beads entrapping gefitinib liposomes allow for a sustained gefitinib release. The liposomes and microbeads were physiochemically

characterized. Additionally, the drug and lipid release from the hydrogel beads was measured in peritoneal simulation fluid (PSF). Optimized gefitinib-loaded hydrogel beads were further tested in an *in vitro* cell culture assay to correlate the *in vitro* release of gefitinib with its anti-cancer function of inducing cell death in Huh-7 cells, an immortalized human hepatocarcinoma cell line.

5.3. Material and methods

5.3.1. Liposome preparation

Liposomal formulations were prepared by the thin film hydration method. Briefly, a proper amount of S80 (Lipoid, Germany) or DPPC (Lipoid, Germany) lipids was weighed and dissolved with chloroform (Biosolve, Netherlands) in a glass flask. The organic solvent was evaporated under N_2 stream, and the lipid film was dried overnight in a desiccator. The lipid film was then rehydrated with an aqueous buffer (pH 7.1, 50 mM HEPES (Merck Millipore, USA), 110 mM NaCl (Carl Roth, Germany)) forming multilamellar vesicles (MLVs). For the formation of small unilamellar vesicles (SUVs), the MLVs were freeze/thawed 6x with liquid nitrogen (1 min) and a room temperature waterbath (5 min) and extruded 10x through a 0.2 µm polycarbonate membrane (Sterlitech, USA) with a LIPEX extruder (Evonik, Canada). The particles' size distribution (polydispersity index, PDI) and hydrodynamic diameter were measured using a Litesizer 500 (Anton Paar, Austria).

5.3.2. Gefitinib stock preparation

Different Gefitinib stocks were prepared depending on the experiments. For liposome preparation, gefitinib free base (LC Laboratories, USA) was dissolved in chloroform (Biosolve, Netherlands) at 100 mM. To assess the kinetic solubility of gefitinib in peritoneal simulation fluid (PSF, pH 7.1, 50 mM HEPES (Merck Millipore, USA), 110 mM NaCl (Carl Roth, Germany), 5

mM Glucose (Carl Roth, Germany) and 1.68 mM $CaCl_2$ (Carl Roth, Germany)) incl. 20% DMSO (Carl Roth, Germany) gefitinib was dissolved in DMSO (Carl Roth, Germany) at 25 mM. Kinetic solubility was assessed by adding an excessive amount of gefitinib (10 µL) to PSF incl. 20% DMSO (990 µL). The mixture was further vortexed for 2 h, at 37 °C allowing the exceeding gefitinib to precipitate. After reaching an equilibrium, the samples were centrifuged (Hermle, Germany) at 12'000 g. A volume of 200 µL of supernatant was measured on a plate reader (Infinite MNano; Tecan, Switzerland) at an absorbance of 334 nm. While kinetic solubility refers to the maximum amount of a solid substance that can dissolve PSF incl. 20% DMSO under conditions where the dissolution rate is determined by the rate of mass transfer (diffusion) thermodynamic solubility determines dissolution by the equilibrium solubility. Thermodynamic solubility measurement method was derived from USP 1236 – Solubility measurements. In brief, an excess of gefitinib loaded microbeads were added to PSF incl. 20% DMSO. To facilitate dissolution of gefitinib, the suspension was actively mixed and incubated at 37 °C for 24 h. Equilibration time (± 5%) was verified after another 24 h. The samples were centrifuged at 12'000 g. A volume of 200 µL of supernatant was measured on a plate reader at an absorbance of 334 nm.

5.3.3. Gefitinib encapsulation into MLVs

Different lipid-to-drug ratios were tested keeping the gefitinib concentration constant (0.5 mM). Briefly, appropriate amounts of gefitinib stock dissolved in chloroform were added to the dissolved lipids. Liposomes were formed as described and the particles were purified from free drug using a PD MiniTrap Sephadex G-25 resin desalting column (Cytiva, USA). The purified particles were destroyed in DMSO and the drug concentration was measured with a plate reader at an absorbance of 334 nm. The encapsulation efficiency (EE) was calculated with following equation:

$$\text{EE } \% = \frac{A_{334}(\text{purified})}{A_{334}(\text{preG25})} * 100\%$$

where "A_{334}(purified)" refers to the optical density of the drug after purification with the G-25 column and "A_{334}(preG25)" refers to the optical density of the drug before free drug removal by the G-25 column.

5.3.4. Additive manufacturing of microbeads

Alginate (Carl Roth, Germany) was dissolved in an aqueous solution (pH 7.1, 50 mM HEPES, 110 mM NaCl) overnight under stirring to reach a homogenous solution with 6% (w/V) alginate. Gefitinib liposomes and alginate solution were mixed in a ratio of 1:1 using two syringes (B. Braun, Germany) connected with a female-female combifix adapter (B. Braun, Germany) by pushing the solution back and forth. The freshly formed ink was loaded into a cartridge (Cellink, Sweden) and was printed for crosslinking, using a Bio X Bioprinter (Cellink, Sweden) equipped with an Electro-Magnetic Droplet (EMD) printhead (Cellink, Sweden), which enables contactless jetting (drop-on-demand) into a 135 mM calcium chloride solution (+ 50 mM HEPES, 110 mM NaCl) in which the microbeads were stored upon further usage. The formed microbeads were characterized by size, shape and morphology using light microscopy (Zeiss, Germany) and scanning electron microscopy (Gemini 450, Zeiss, Germany).

5.3.5. Lipid entrapment and cumulative release from microbeads

Liposomes were formed as described before with the addition of 0.05 mol% DiD (ThermoFisher, USA). To calculate the entrapment efficiency of the lipids into the microbeads, the lipid content before and after crosslinking the alginate ink was measured by fluorescence of DiD with a plate reader at an emission of 672 nm after the dye was excited at 630 nm. Therefore, the hydrogel beads were dissolved in extraction buffer (100 mM EDTA (Carl Roth, Germany) and 200 mM sodium citrate (Merck Millipore, USA)). The extracted solution was further dissolved in DMSO to destroy the liposomes and then DiD fluorescence was measured as described above. Cumulative lipid

release was measured by horizontal incubation of DiD-liposome loaded microbeads into a 15 mL tube containing 10 mL PSF at 37 °C and 200 rpm. At different time points, 1 mL was sampled and replaced with 1 mL fresh PSF. The fluorescence of the collected sample was measured with a plate reader as described above. The cumulative release was normalized to the total retrieved DiD amount in the microbeads.

5.3.6. Cumulative gefitinib release from microbeads

Microbeads containing either gefitinib loaded MLVs or just gefitinib were formed as described above. Cumulative gefitinib release was measured by horizontal incubation of the loaded microbeads into a 15 mL tube containing 10 mL PSF at 37 °C and 200 rpm. At different time points, 1 mL was sampled and replaced with 1 mL fresh PSF. The drug concentration was measured as described. The cumulative drug release was normalized to the total amount of drug in microbeads at t_0. Therefore, the drug was extracted following an established extraction protocol. In brief, extraction buffer was added to microbeads and vortexed for 20 min. To facilitate the dissolution of the microbeads the suspension was exposed to a water bath at 65 °C for 5 min. Dissolved beads were diluted (DF: 5) with DMSO:Chloroform (9:1) and once again vortexed for 15 min. After sonication for 10 min in a 65 °C water bath, samples were centrifuged at 12'000 g and the supernatant was measured as described.

5.3.7. Stability

Lipid stability and drug encapsulation was assessed over a period of 7 days. To assess the stability of the respective lipids, liposome aliquots (250 µL) were taken after purification form free drug for analysis using an HPLC equipped with a charged aerosol detector (CAD, Ultimate 3000, Thermo Fisher Scientific, USA) at t_0 and t_7. Lipid content and chromatograms were compared to detect potential degradation. Phosphatidic acid (Merck Millipore, USA) was used as internal

standard to evaluate lipid contents. Microbeads were prepared and gefitinib extracted and analysed as described above at t_0 and t_7 respectively using the same liposome stock hydrated at t_0. Gefitinib content retrieved at t_0 and t_7 were compared to evaluate drug degradation or diffusion into aqueous phase of the hydrated liposomes during storage at 4°C.

5.3.8. Cell culture

Huh-7 cells (RRID:CVCL_0336) were cultured in low glucose (1.0 g/L) DMEM (Carl Roth, Germany) supplemented with 10'000 units/L of penicillin and streptomycin (P/S; Gibco, USA), 200 mM L-Glutamine (Sigma, USA), and 10% (V/V) of sterile filtered (0.2 µm, cellulose acetate membrane) fetal bovine serum (FBS; Merck Millipore, USA) at 37 °C in a humidified atmosphere containing 5% CO_2. For cell splits, the cells were washed with PBS, detached with 2 mL Trypsin-EDTA (0.25%) (Thermo Fisher, USA) per flask and incubated for 4 min at 37 °C.

5.3.9. Quantitation of viable cell number in cytotoxicity assays

Huh-7 cells were seeded at a density of 25'000 cells in a 48-well plate (Faust, Switzerland). Inserts for 48-well plates (CellCrown, Merck-Millipore, USA) were combined with polyamide membranes with 50 µm pores (A. Hartenstein, Germany). Cells were treated with free gefitinib (5, 20, 50, 100 µM), different amounts of gefitinib beads (corresponding to 5, 20, 50, and 100 µM gefitinib), and empty alginate beads for 24 h at 37 °C in a humidified atmosphere containing 5% CO_2. To solubilize the free drug, 0.5% (V/V) of DMSO was added. The CCK-8 assay (Merck Millipore, USA) was used to determine cell viability following the manufacturer's instructions. Briefly, the inserts were removed, the cells were washed with PBS and 180 µL medium + 20 µL CCK-8 solution was added to each well. After further 2 h of incubation at 37 °C and 5% CO_2, the absorbance at 450 nm was measured with a plate reader. The cell viability was calculated with following equation:

$$\text{Cell viability } \% = \frac{\text{OD}_{\text{treatment}}}{\text{OD}_{\text{DMEM}}} * 100\%$$

where “OD treatment” refers to the optical density of the Huh-7 cells treated with the specific treatment and “OD DMEM” refers to the optical density of Huh-7 cells treated with the vehicle (DMEM).

5.4. Results

Hydrogel microbeads with two different lipid formulations encapsulating the drug gefitinib were prepared and evaluated for their suitability for IP administration. Hydrogel microbeads containing free drug were used as a comparison. Different alginate concentrations were screened and combined with different lipid formulations. The microbeads were characterized for their physiochemical characteristics. To determine drug release, peritoneal simulant fluid (PSF) was used. Proof of concept was performed using Huh-7 cells, an immortalized human hepatic carcinoma cell line, to determine the dose-dependent cell viability for the drug delivery system.

5.4.1. Microbeads synthesis and physiochemical characterization

Liposomes are often used in the delivery of poorly soluble compounds such as gefitinib. While these systems are beneficial carriers for poorly soluble drugs the nano scale of said systems is not suited for an environment with high clearance such as the peritoneal space[183]. To reduce the clearance, larger depot systems within the peritoneum can be used. Alginate hydrogels are bioorthogonal and biodegradable built by a cross-linked mesh allowing entrapment of liposomal systems which makes them a suitable candidate. The preparation of these microbeads is presented in scheme 5.1.

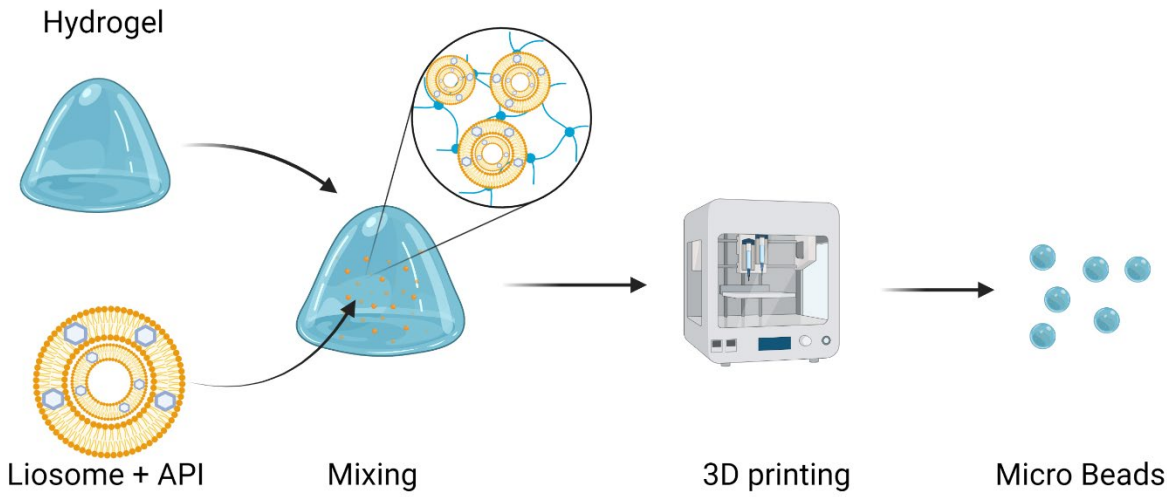

Scheme 5.1. Preparation of microbeads by mixing alginate hydrogel with liposomes encapsulating gefitinib and 3D printing the formulation.

Liposomes encapsulating the hydrophobic drug were prepared using thin-film method. After hydration, excessive gefitinib was removed from liposomes using SEC. The main fraction containing the liposomes was used for further processing (**Figure A5.1.**). Liposomes were characterized in terms of their size, PDI, zeta potential and EE%, whereas PDI values indicate a broad size distribution. This is due to the fact that MLVs are prepared. While size and PDI could have been more closely controlled by producing SUVs following F/T cycles and extrusion, MLVs have advantageous characteristics. For one, due to the hydrophobic nature of the drug, low drug:lipid ratios yield high EE% since MLV systems offer many hydrophobic areas to encapsulate the lipophilic drug within their lamellas. Further, the large size of the MLVs is potentially beneficial considering the entrapment of the particles within the hydrogel. With the hydrogel having an average mesh size ranging from 10-100 nm[191] particles with bigger diameters should be tighter entrapped within the gel. In addition to DPPC, MLVs were also formed from S80, an essential phospholipid extract from soybean containing 73-79% phosphatidylcholine, for drug

encapsulation. The reason for using S80 was its cost-effectiveness compared to DPPC, as well as its fibrosis resolving features, which may be advantageous, particularly following abdominal surgery[45]. Different lipid:drug ratios were evaluated for S80 and DPPC respectively of which low drug-to-lipid ratios manifested better EE% for the hydrophobic agent as indicated in Figure 5.1A. Further, comparing the EE% of the different lipids the results indicate a more efficient encapsulation of the drug for S80 at lower drug:lipid ratios. Hence, the drug-to-lipid ratio had a bigger influence on the gefitinib encapsulation, compared to the choice of lipids. Nevertheless, S80 MLVs encapsulated 90% of gefitinib for the 1:30 ratio which is higher than the 75% encapsulation efficiency obtained with DPPC MLVs. The reason for the better encapsulation efficiency in S80 MLVs might be due to the presence of non-saturated phospholipids in the mixture, which make the lipid bilayers more fluid. Hence, a stronger interaction between the drug and the S80 lipid bilayer might be facilitated leading to an enhanced EE%. Even though, smaller drug-to-lipid ratios than 1:30 would likely lead to higher encapsulations of gefitinib it would also hinder the scaling potential, as increasing the gefitinib concentration in the MLVs would lead to huge lipid amounts rending the liposome formation harder and eventually lead to printing issues due to the high viscosity. Drug-loaded liposomes were mixed with alginate (3% w/V) after a screening of different alginate concentrations identified a 3% w/V concentration as most suited for 3D printing. The entrapment efficiency of gefitinib-loaded liposomes in alginate beads is close to 100% for both, S80 and DPPC, as displayed in Figure 5.1B. This indicates that a neglectable amount of gefitinib was lost during the production process and the entire drug amount was retrieved. The low entrapment efficiency for free drug (FD) in alginate is most likely due to the hydrophobicity of the drug. Making it challenging to prepare a hydrophobic agent in a hydrogel without any suitable carrier. However, this once more indicates the importance of a suitable carrier

to enable delivery of hydrophobic drugs such as gefitinib. Further, the stability of the lipids, the drug, and its encapsulation over a period of 7 days was investigated, although liposomes used for production were always prepared freshly. Regarding lipid stability for DPPC and S80, no lipid degradation was identified over the studied period of 7 days for both lipids respectively (**Figure A5.2.**). Also, considering the stability of gefitinib and its encapsulation no drug degradation nor loss in encapsulation within 7 days was detected (**Figure A5.2C**).

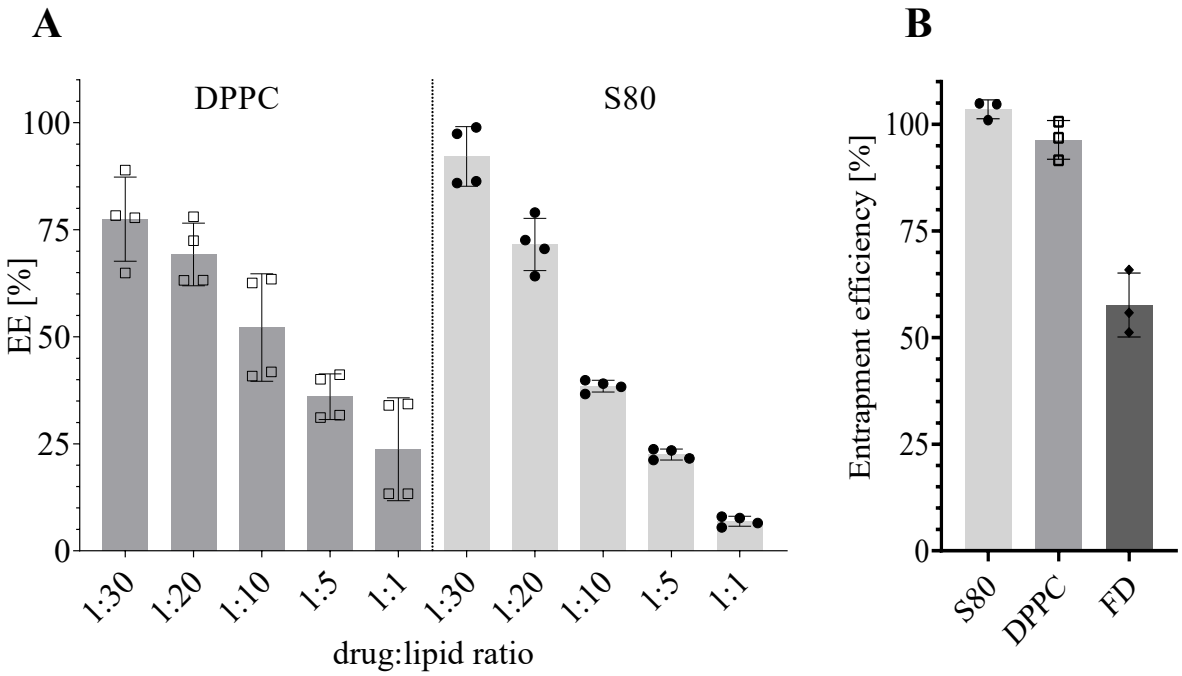

Figure 5.1. A: 1Encapsulation efficiency (EE%) of gefitinib in DPPC or S80 MLVs with different drug-to-lipid ratios (mean ± SD, n = 4). **B:** Entrapment efficiency of gefitinib loaded beads (mean ± SD, n = 3).

Further, microbeads were characterized in size, shape, and appearance. Microscopic measurements of the microbead´s diameter revealed the size distribution as visualized in Figure 5.2. and Table 5.1. The distribution suggests homogeneous distribution during the production and a favourable reproducibility which is promising considering scaling up the process. Nevertheless,

the presence of different lipids has an influence on the printability and hence on the size of the microbeads. This is potentially due to the lipid´s influence on the rheological properties of the ink. The surface-to-volume ratio (SVR) provides a measure of surface per amount of volume. For a system with a large SVR such as for S80 microbeads, one would expect a higher surface area and hence potentially faster release while systems with lower SVR such as DPPC microbeads are potentially capable to sustain the drug longer. This is mainly due to the exposed surface area and the diffusion distance a drug needs to travel before reaching the release media.

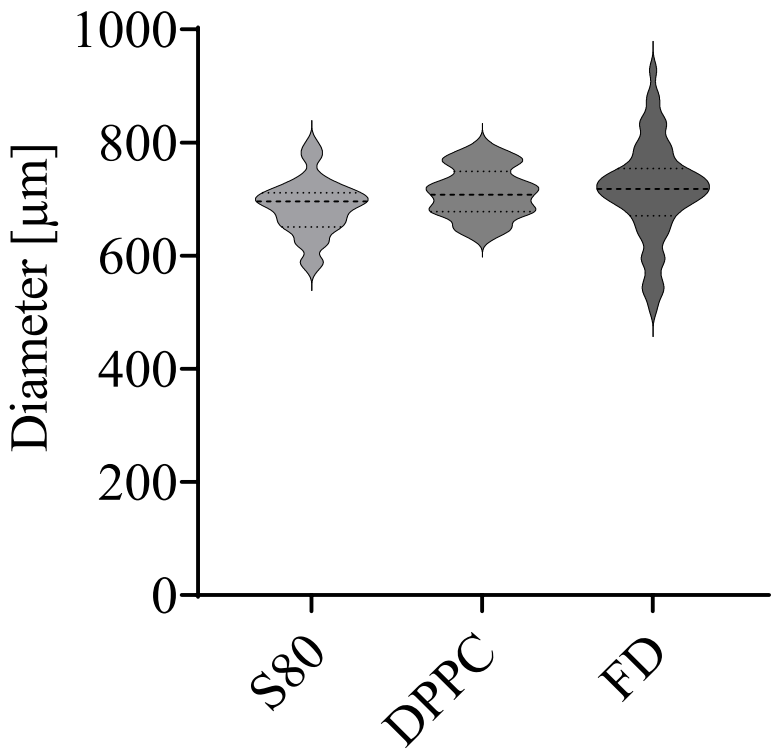

Figure 5.2. 2 Microbead diameter for assessed formulations used to calculate the surface to volume ratio with following formula: $SVR = 1/r^2V$. Data represented in as a violin plot (n=60).

Table 5.1. Dimensional characteristics of microbeads.

Bead	Diameter [µm]	SVR [μm^{-1}]

S80	686 ±49	8743 ±71
DPPC	712 ±43	8424 ±61
Empty	714 ±86	8404 ±20

The morphological difference of the prepared formulation can be observed in Figure 5.3. It is apparent that S80 and DPPC microbeads have a spherical shape while the shape of the FD microbeads has minor misshaped areas. Further, the colour of the beads seems to be influenced by the lipid formulation used. Also, for a minor amount of microbeads air bubbles were entrapped into the beads as seen in Figure 5.3B. All irregularities on the surface of the microbeads influences the SVR and thereby potentially the release of the drug since a different amount of surface is exposed to the release media. Beads were further quantitatively assessed visually for injectability through an 18G needle within which no differences or irregularities were observed indicating that the system is suitable for injections (**Figure A5.3.**). While it is undeniable that injectability is a favourable feature for such a system one needs to keep in mind that the microbeads can also be administered directly after necessary surgical removal of metastasis before suturing the wound or via a peritoneal port ID>10 mm that is introduced after many surgeries of this kind[192]. For such routes of administration, the sheer stress to which the microbeads are exposed can be estimated as low as to be neglectable.

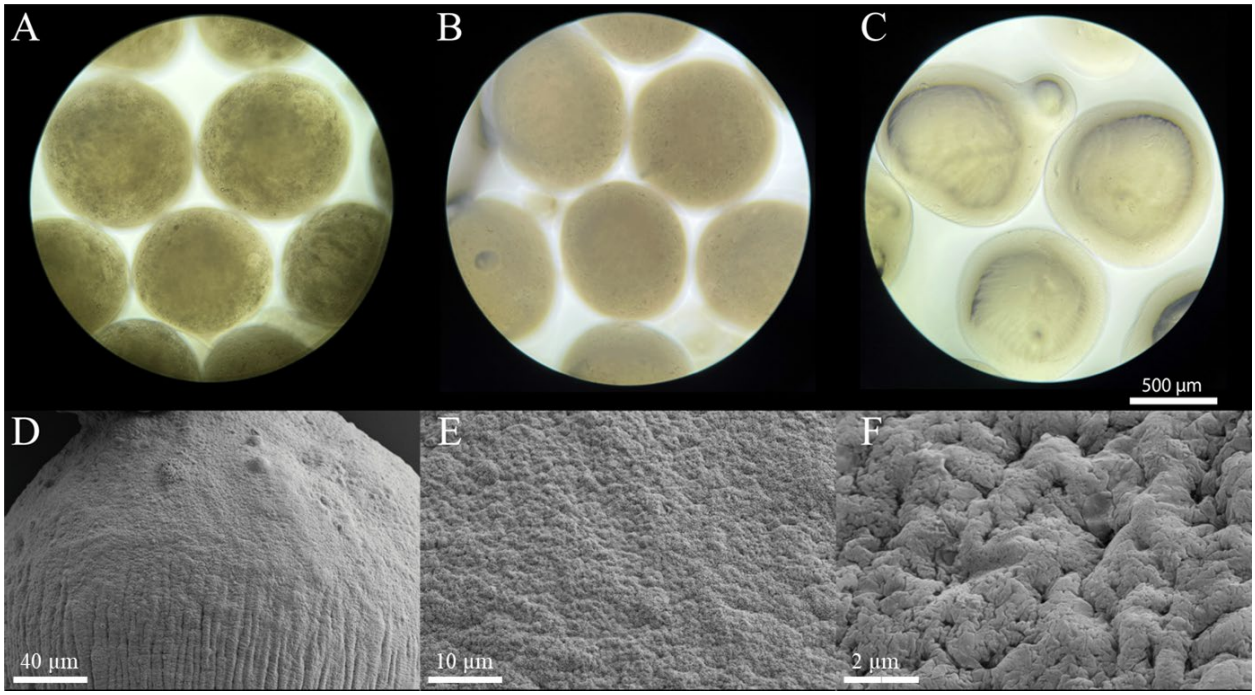

Figure 5.3.3 Images of microbeads after 3D printing. **A:** S80 microbeads (15 mM S80; 3% Alg; 0.5 mM gefitinib). **B:** DPPC microbeads (15 mM DPPC; 3% Alg; 0.5 mM gefitinib). **C:** FD microbeads (3% Alg; 0.5 mM gefitinib). SEM images of dried microbead (15 mM S80; 3% Alg; 0.5 mM gefitinib). **D:** Surface image of microbeads at a macro scale. **E:** Micro scale of surface area shows homogeneous distribution of pores over surface area. **F:** Pores with a diameter of ~100nm on the surface.

SEM images of the microbeads as shown in Figure 5.3. provide detailed impressions of the microbead´s surface. While the beads show minor irregularities at the macroscale (D) which might be caused during printing, the surface at a microlevel (E) seems homogeneous. Zooming in on the surface area of the beads pores were identified with a diameter of approximately 100 nm (F) which is in line with previous reporting[193]. It is assumed that said pores are small enough to allow surrounding release media to enter the beads, further increasing the exposed surface area of the bead. But at the same time, pores of 100 nm are likely capable to entrap larger MLVs and thereby hinder the lipids to be directly released for the system[194].

5.4.2. Drug solubility

The solubility of gefitinib in peritoneal simulation fluid (PSF) provides information on the limitations of drug release from the delivery system. Commonly, liberation from liposomes is governed by the availability of suitable binding partners that solubilize the drug in its microenvironment[195, 196]. Hence, 20% DMSO was added to PSF used to measure the solubility of gefitinib at physiological temperature (37°C) following a kinetic and a thermodynamic approach (**Table 5.2.**). The PSF simulates the peritoneal fluid of a healthy individual regarding, pH, buffer capacity, glucose, $MgCl_2$ and $CaCl_2$ content[190]. Considering the nature of gefitinib, pH and glucose content are drivers of solubility, besides DMSO, as preliminary studies indicated. Further, it was observed that highest solubilities were achieved when using an excessive amount of gefitinib that was first encapsulated in liposomes and entrapped in microbeads rather than dissolving an excessive amount of free gefitinib powder.

Table 5.2. Kinetic solubility of gefitinib vs. Thermodynamic solubility of gefitinib obtained from release system (Microbeads; 15 mM S80; 3% Alg; 0.5 mM gefitinib). Solubility assessments were conducted in PSF with or without 20% DMSO (mean ± SD, n ≥ 3).

Media	Procedure	pH	Gefitinib solubility [$\frac{mg}{mL}$]
PSF + 20% DMSO	Thermodynamic	7.1	23.53 ±1.25
PSF + 20% DMSO	Thermodynamic	7.8	9.22 ±2.03
PSF	Thermodynamic	7.1	5.20 ±0.12
PSF + 20% DMSO	Kinetic	7.1	13.89 ±1.07
PSF	Kinetic	7.1	0.58 ±0.25

5.4.3. Release

To study the microbead's capability to entrap the loaded liposomes, the lipid release of the system was measured. DiD, a dye with similar lipophilic characteristics as the evaluated drug, was encapsulated in liposomes and entrapped in microbeads. Due to the hydrophobic nature of DiD, said dye remains entrapped in the lipid bilayer and is hence an indicator of lipid release. Figure 5.4. indicates neglectable amounts (<0.1%) of lipid release for both assessed lipids over a period of 9 days. Similar results were obtained with microbeads filled with 200 nm SUVs, showing a neglectable liposome release (**Figure A5.4.**). This finding provides further evidence supporting the previously proposed assumption that the nanopores, which are approximately 100 nm in size, on the surface of the microbeads are capable of effectively retaining the MLVs within the alginate beads. As previously discussed, the retention of liposomes within the microbeads is advantageous due to the high clearance rate small particles (<1 μm) face within the peritoneum.

Drug release from microbeads was studied in PSF with 20% DMSO at physiological temperature of 37°C and horizontal shaking to simulate the movement within the peritoneum. Microbeads entrapping DPPC and S80 liposomes each encapsulating gefitinib were tested. As a control, FD entrapped in microbeads was used. FD microbeads manifest a burst release of the drug within the first 4-5 h as indicated in Figure 5.4C. The gefitinib release from DPPC microbeads was sustained over 3 days, with reaching ~100% and ~80% drug release for DPPC and S80 respectively, after an initial burst release of approximately 70% within the first 3 h. The retention of gefitinib in the S80 system might be caused by a stronger interaction between the drug and the S80 lipid bilayer and was not overcome through the slightly bigger SVR compared to DPPC. This would be congruent with the trend observed in EE%. When comparing the drug release results to the lipid release

results it is undeniable that the drug leaves the lipidic environment and diffuses through the alginate into the release media.

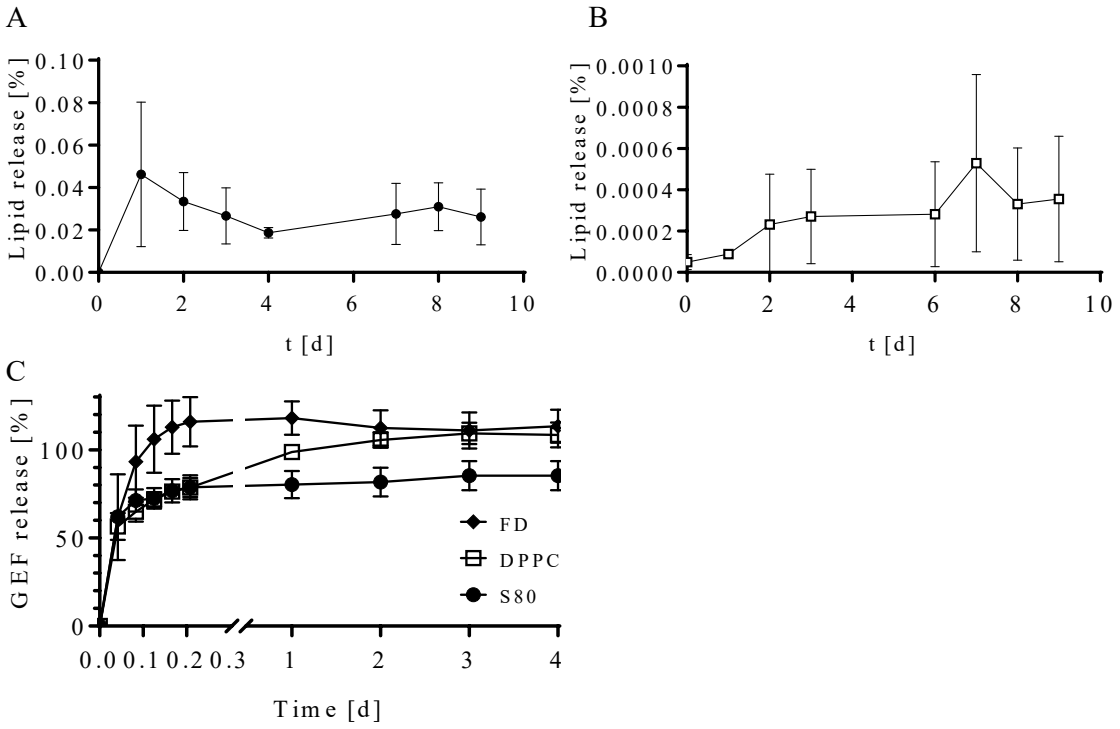

Figure 5.44. A: S80 MLV release from microbeads measured by DiD fluorescence (15 mM S80; 3% Alg; 5 nM DiD). **B:** DPPC MLV release from microbeads measured by DiD fluorescence (15 mM S80; 3% Alg; 5 nM DiD). Results normalized to cumulative content after recovery of the lipids (mean ± SD, n ≥ 3). **C:** Drug release from 3D printed microbeads (15 mM Lipid; 3% Alg; 0.5 mM gefitinib) in PSF (mean ± SD, n ≥ 3).

Surgical and locoregional treatment of peritoneal metastasis, such as those originating from colorectal cancer, has gained widespread acceptance following the publication of favourable patient outcomes by various groups worldwide[104]. However, the peritoneum can become damaged due to various factors such as surgical trauma, infection, or exposure to peritoneal dialysis fluid following said surgical interventions treating peritoneal metastasis[197, 198]. Under such circumstances, fibroblasts may attach to the fibrin and produce collagen, leading to the formation of adhesive fibrotic tissue[197, 198]. Hence, the use of S80 is further beneficial due to its

antifibrotic behaviour as reported by our group[45]. Further, the high availability and low cost of S80 make it a desirable candidate for further drug development and scale-up.

5.4.4. In vitro

Different concentrations of gefitinib were applied to Huh-7 cells, an immortalized human hepatic carcinoma cell line, either as free drug in DMEM + 0.5% (V/V) DMSO, or encapsulated in MLVs entrapped in alginate microbeads without DMSO addition. Hence, for experiments in DMEM, the solubility did not allow the testing under sink conditions. Further, the presence of Ca^{2+} in all release media should be highlighted. Considering the crosslinking capabilities of said divalent cation its presence contributes to the stability of the sodium alginate microbeads within the release media. Therefore, fast solvation of alginate and thereby burst release of the liposomes was avoided. Thereby, the integrity of the system was ensured during its lifecycle providing controlled release and avoiding fast clearance. The cells were treated for 24 h and their viability was measured after removal of the beads. To avoid unwanted toxicity due to contact between beads and cells inserts were used to physically separate the beads from the cells, while still ensuring gefitinib to pass through the insert membrane and be absorbed by the Huh-7 cells.

Concentration-dependent Huh-7 cell death was observed with the gefitinib, both when in its free form and when released from the microbeads (**Figure 5.5.**). Higher cell death was obtained if the drug was released from the microbeads, which can be explained due to cytotoxicity of the beads themselves, but also due to the solubility of the drug as discussed previously. No DMSO was needed to help gefitinib be released from the microbeads and transported to the Huh-7 cells. The sustained released might be enough to avoid having an excessive high free gefitinib concentration which would lead to precipitation, whereas albumin, the main component of FBS, probably

facilitated gefitinib transport due to its ability of binding small hydrophobic compounds[199, 200]. Those results lay the foundation for *in vivo* studies with gefitinib-loaded microbeads, as these results demonstrate that drug release can induce cell death without the use of an organic solvent to aid in the solubilization of gefitinib.

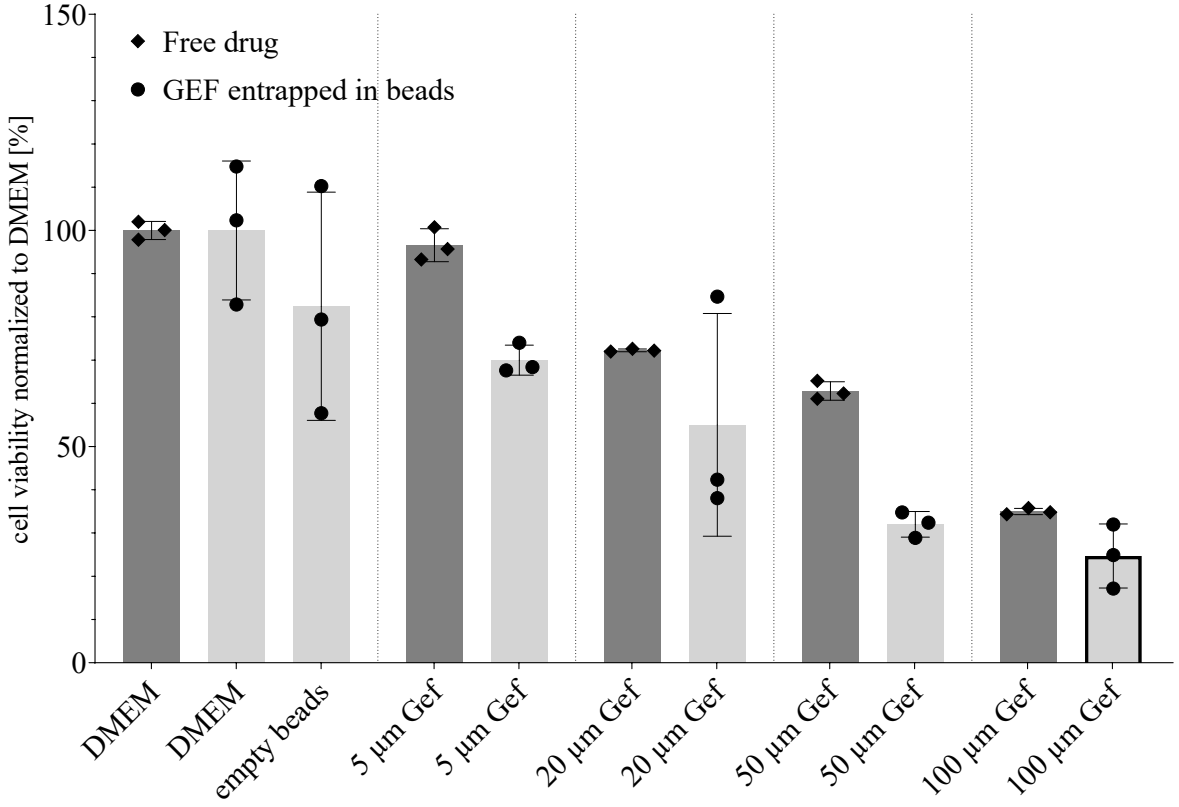

Figure 5.5. 5Cell toxicity of different gefitinib (Gef) concentration on Huh-7 cells (mean ± SD, n = 3). Gefitinib was either administered as free drug in presence of 0.5% (V/V) DMSO, or encapsulated in MLVs entrapped in microbeads, where no DMSO had to be added.

5.5. Conclusion

This study describes a scalable, reproducible, and affordable manufacturing of microbeads entrapping liposomes loaded with a hydrophobic anti-cancer drug gefitinib. Further, the microbeads were characterized and found to have nanopores on their surface, which allowed for drug release while effectively entrapping MLVs. Drug release was assessed in peritoneal

simulation fluid for two lipids respectively which controlled drug release over a period of 3 days. Also, the system was tested on relevant cancer cells, potentially present in the peritoneal space. Test revealed dose dependent cell viability indicating the systems potential to be used as secondary treatment against adhesion after surgical removal of peritoneal carcinoma and as primary treatment against cancer and metastasis within the peritoneal space. Hence, microbeads encapsulating gefitinib-loaded liposomes are a potential alternative to current treatment methods since a sustained gefitinib release can be achieved in the peritoneum. Furthermore, the liposome-loaded microbeads are a potential delivery platform for a variety of different drugs or drug combinations, potentially reducing the cost and time required for drug development and clinical trials. This is especially relevant considering drugs with challenging physiochemical characteristics such as hydrophobicity. In conclusion, this study demonstrates the potential of microbeads encapsulating liposomes loaded with gefitinib as an alternative to current treatment methods, and a versatile platform for various drugs or drug combinations, ultimately benefiting cancer patients worldwide.

Chapter 6.

Final Remarks and Future Perspectives

In our fast-paced society, it is common to experience long and stressful days that leave us tired and exhausted. As a result, many of us may turn to highly processed foods like fast food or reach for a glass of wine or beer to relax. While this may not seem like a big issue, if done on a regular basis, these habits can have significant long-term consequences for our health. The impact of Western lifestyle and diet on health has been significantly associated with the incidence of chronic inflammation, obesity, and diabetes[201]. All these, together with viral infections, autoimmune diseases, and metabolic disorders are part of the reasons why chronic liver diseases affect over 1.5 billion people worldwide (any stage of disease severity) ending deadly in almost 2 million cases per year with an increasing tendency[23, 202-204].

Non-resolved chronic liver injuries lead to liver fibrosis. While early-stage liver fibrosis has been described to be reversible, there is still a lack of effective treatments available. If left unresolved, liver fibrosis progresses to liver cirrhosis, liver failure, or even liver cancer, where only a liver transplantation can save the patient. Hence, there is an urgent need for novel and effective therapies for fibrosis resolution.

Hepatic stellate cells have been identified as the key player in fibrosis progression due to their excessive production of extracellular matrix upon activation. This makes them interesting from both a therapeutic and a diagnostic perspective. Our group developed polyenephosphatidylcholine-rich formulations (S80-based) that showed beneficial effect in fibrosis resolution in an *in vitro* model of human liver fibrosis[45]. Building upon those finding, our group demonstrated differently released EVs from LX-2 cells (immortalized human HSCs) and fibrosis-resolving potential in EVs released from S80 treated HSCs[205].

We aimed with the present work to create a feasible bioderived therapeutic for chronic liver diseases inspired by EVs. Therefore, we formed artificial EVs, termed cell-derived nanovesicles

(cdNVs) from differently pre-treated LX-2 cells and checked if they preserve the fibrosis-resolving features as observed for EVs.

In **Chapter 2** we established, through systematically testing different cell lysis methods, an upstream pipeline for the formation of cdNVs. Characterization by DLS and NTA revealed the formation of nanosized particles with a homogenous size distribution and a negative surface charge. The upstream process was applicable on differently pre-treated LX-2 cells resulting in particles with the same physical characteristics. Generated particle amount could be increased by increasing the starting cell concentration pre-lysis. Genotypical assessing of cdNV treated LX-2 cells revealed the formation of lipid droplets, hinting a quiescent-like transformation, implying preserved activity after formation. Dilution experiments showed a moderate correlation between lipid droplet formation and particle concentration. However, anti-fibrotic pre-treatment of LX-2 cells prior cdNV formation did not seem to enhance fibrosis resolving potential. But before further activity investigations could be performed, a downstream pipeline for the purification of cdNVs had to be established.

Chapter 3 describes the establishment of a purification and enrichment procedure of freshly formed cdNVs. The process resulted in retainment of 40% of freshly formed cdNVs, while removing over 95% of the proteins, and sterilize the particles. Additionally, pelleting the cdNVs did allow to rehydrate them in the medium/buffer of choice with different volumes, depending on the targeted final concentration. Transmission electron microscopy confirmed a round morphology of the particles. Physicochemical characterization showed a homogenous nano-sized population and the presence of particle associated proteins and nucleic acids. The purification process was reproducible with cdNVs derived from differently pre-treated LX-2 cells yielding approximately 10’000 cdNVs/LX-2 cells in all tested conditions. Together with **Chapter 2, Chapter 3** laid the

foundation required for more comprehensive and in-depth activity studies on cdNV treated LX-2 cells.

Built upon the formation and purification of cdNVs, in **Chapter 4** we were able to genotypically and phenotypically assess fibrosis resolving potential of cdNVs from differently pre-treated LX-2 sources. Naïve LX-2 cells restored lipid droplets upon treatment with cdNVs. The quiescent-like genotype was confirmed phenotypically by qPCR, observing an increase in PLIN2 mRNA transcription, which codes for the adipose differentiation-related protein involved in the storage of lipid droplets. Additionally, a decreased expression in the two fibrotic mRNA markers COL1A1 and SPARC was detected. The change in fibrotic markers was also observed upon cdNV treatment of perpetuated LX-2 cells. The activity was found to be concentration dependent with a bigger effect for higher cdNV doses.

Treatment of perpetuated LX-2 cells with sn after normalizing the protein concentration in the soluble factors, collected during purification, to the protein concentration in the used cdNV doses did not result in transcriptional change of the selected markers. However, we measured a concentration-dependent change in fibrotic markers when testing higher amounts of soluble factors, indicating the presence of biologically active molecules in the sn.

We evaluated the role of the cdNV lipids in the fibrosis resolving activity. Therefore, we formed cdNV-liposomes (cdNV-L) from cdNV extracted lipids which showed (almost) no protein content. Treatment of perpetuated LX-2 cells with cdNV-Ls did lead to a small increase in PLIN2 mRNA. However, this was not enough to trigger an anti-fibrotic response, even though it was described as a fibrosis resolving driver by Friedman in 2010[54]. On the contrary, while the COL1A1 mRNA expression was not affected, an increase in SPARC mRNA transcription was observed for all tested cdNV-L concentrations. Moreover, cdNV-L showed a significantly lower uptake into LX-2 cells

compared to cdNVs, proving the importance of the membrane composition for particle uptake making a strong case for a preserved homing effect in cdNVs. Particle uptake was increased upon perpetuation of LX-2 cells which might be related to a slight increase in cell membrane fluidity compared to naïve cells[45].

Restoring a surface corona on cdNV-Ls by incubating them with the soluble factors of the sn did not increase the particle uptake, but if a high protein concentration (~10x higher than on cdNVs) was used, anti-fibrotic properties were restored underlined by a decrease in COL1A1 and SPARC mRNA transcription. Thereby, a synergistic effect of soluble factors and particles was detected, as the fibrosis-resolving properties of the sn were enhanced in presence of the particles. Hence, it seems that the surface corona is mainly responsible for the transcriptional changes in perpetuated LX-2 cells, whereas the vesicles are important for the presentation of this surface corona, as the soluble factors in absence of particles lead to a smaller effect. Further, the lipids of the cdNVs have a beneficial effect by enhancing the PLIN2 mRNA expression in treated LX-2 cells.

LX-2 cells display different expression profiles of fibrotic markers upon treatments with DMEM, RolPA, S80, or TGF-β_1. However, despite the different cdNV conditions tested, the transcriptional changes measured in LX-2 cells upon administration were similar. Although there were minor differences between the treatments, these variations were likely due to the inherent biological variability of the treated cells rather than the origin of the cdNVs. The reason for this is unclear, still, it highlights the importance of comprehending the underlying factors responsible for the fibrosis-resolving activity.

Our results unveil promise in using cdNVs for chronic liver diseases, linking their activity to a functional corona, contributing to the research on artificial EVs for regenerative medicine.

Nevertheless, there are various needs of follow-ups of this work to understand the full potential of cdNVs for chronic liver diseases.

Aggregation and variability of cdNV formation indicate that the upstream process can be optimized. Performing the extrusion at 4 °C, as well as introducing smaller pore sizes during serial extrusion might increase the yield. Besides, the effect of freeze/thawing and sonication on the activity of cdNVs should be explored to understand if the activity is altered, as those two techniques proved to enhance the formation procedure. Due to the limitations of simple 2D cell culture, such as insufficient cell expansion, a scalable upstream pipeline for cdNV production requires investment in bioreactors. Optimization of the downstream purification procedure can be considered as well. Almost all proteins were removed, however observing the importance of the surface corona for cdNV activity calls for gentle purification techniques, as well as potentially the use of less pure samples. Understanding which proteins are crucial for the activity would help optimize a purification protocol, trying to ensure that those proteins remain on the particle. Further, UC as well as DGC are not very suitable for up-scaling to an industrial level. Continuous flow ultracentrifugation can improve the scalability, but the most suitable technique for a gentle and scalable purification allowing the process of thousands of litres is TFF.

However, most of the follow-ups are needed in the activity studies of cdNVs. We do not know for how long the transcriptional changes remain in LX-2 cells and to which extent resolution can be achieved. Also, we looked at lipid droplets and three fibrotic markers to assess the cell state, but in reality, more than 150 genes are altered in HSCs upon fibrosis formation[170, 177]. Hence, to really understand the state in which LX-2 cells are upon treatment with cdNVs transcriptomics, as well as proteomics would be needed. This should also answer the question if cdNVs from differently pre-treated LX-2 cells lead to different outcomes in treated LX-2 cells.

Further characterization of cdNVs is needed to understand what the active molecule(s) are. Lipidomics, transcriptomics, proteomics, and glycomics would help identify active compounds which could be enriched by adjusting the upstream and downstream procedures accordingly.

The observed homing effect would have to be confirmed by *in vivo* studies which can also reveal if other beneficial properties of EVs, such as low immunogenicity and increased bioavailability, are preserved.

Although a high cdNV concentration was necessary to induce a translational change, making it unsuitable for human therapy, cdNVs' potential homing effect makes them an interesting carrier for transporting potent drugs, siRNAs, miRNA, or other beneficial molecules in fibrosis resolution to HSCs. As a result, further experiments into the use of cdNVs as a drug delivery system could help the development of effective anti-fibrotic therapies. The particles can be loaded with drugs post purification, such as performed with DiR in this study, if very hydrophobic molecules are used. Passive encapsulation of small molecules during the serial extrusion procedure or, more complicated, engineering of the originating LX-2 cell leading to the overexpression of specific molecules, can be performed. Loading of small RNAs could be achieved e.g., by electroporation as already performed for EVs[206]. The negative surface charge of cdNVs could also be exploited for encapsulation, as it is usually easier to incorporate drugs, nucleic acids, and proteins into liposomes, which if positively charged can be fused with the cdNVs leading to hybrid particles. Of course, additional studies would be needed to see how those particles behave *in vivo*.

Even though, still at a very early research state, I believe that artificially created extracellular vesicles will play an important role in personalized regenerative medicine. Gaining more and more knowledge on EVs, which are able to functionally transport a variety of molecules throughout the

body, coupled with decades of research on synthetic nanoparticles, holds great promise for the creation of hybrid particles with the potential to cure various diseases.

A very promising study for future usage of cell-derived nanoparticles in medicine was published on December 25, 2022. In this study, a scalable and GMP-compliant pipeline was established for the formation of cdNVs from mesenchymal stem cells using serial extrusion and TFF[90]. This kind of publication will drive the field in the right direction enabling more and more clinical studies to be started involving artificial EVs and hybrid particles with the goal to cure patients from various diseases.

Additionally, we created a platform for the delivery of various compounds to the peritoneum using adaptive manufacturing, which enables a scalable, fast, and highly reproducible production. The printed bioorthogonal and biodegradable microbeads did not release any liposomes, no matter which size was tested, but still allowed for a sustainable drug release. Gefitinib was used as a model drug and concentration-dependent cell death in the hepatocarcinoma cell line Huh-7 could be shown. Varying the alginate concentration could be used to change the release profile of lipids and drugs, but further testing is needed to fully understand the influence of the alginate concentration on the release and stability. The platform can be used to target the liver via the peritoneum with different compounds. For example, while HSCs are targeted by cdNVs through the systemic circulation other compounds could be released in the peritoneum targeting e.g., hepatocytes leading to a simultaneous fibrosis-resolving effect in several cell types involved in fibrosis. But the potential of this platform is not only suitable for liver fibrosis, but generally for peritoneal fibrosis and all other diseases, such as endometriosis and metastatic cancer, that can be targeted through the peritoneum.

Appendix

Supplementary information per chapter

Chapter 2 supplementary information

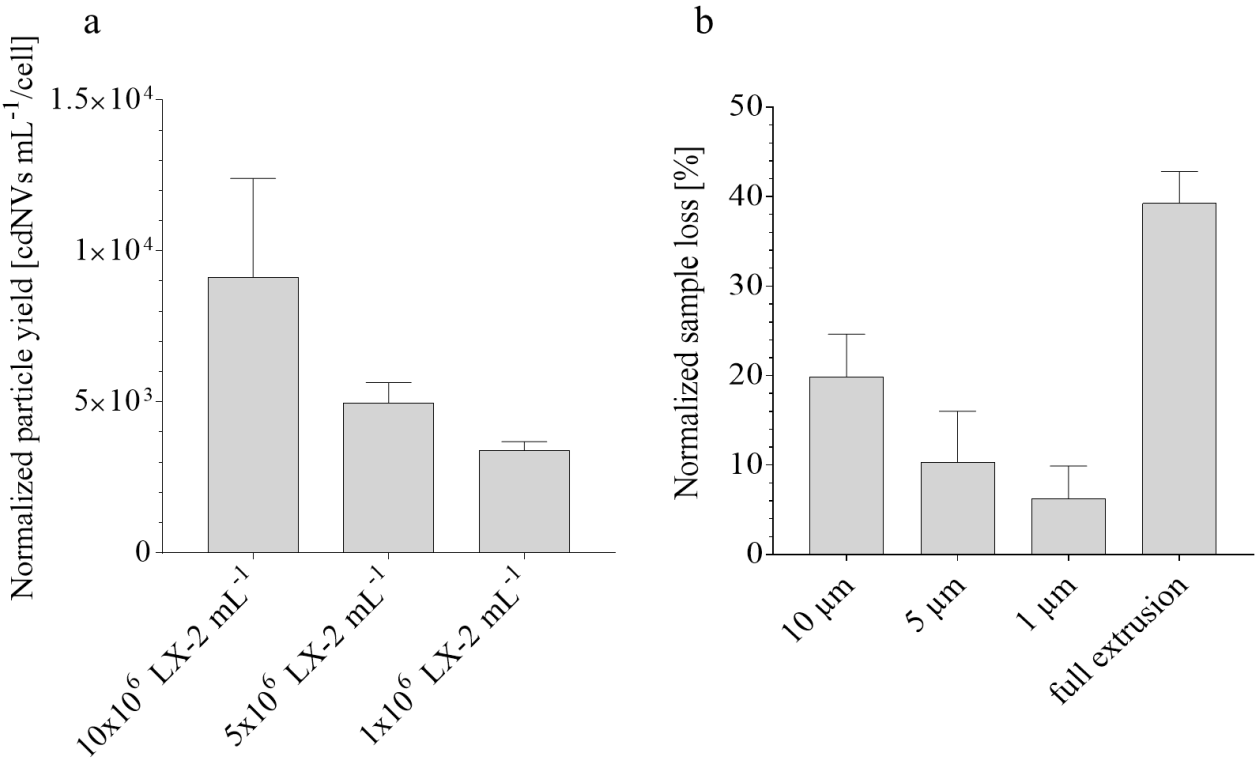

Figure A2.1. Cell-derived nanovesicles (cdNVs) formed through serial extrusion.

a, Particle concentration obtained after serial extrusion (5x 10 µm, 5x 5µm, 5x 1 µm) normalized to the starting amount of LX-2 cells (mean ± SD, n ≥ 2). For this experiment the Lipex extruder was used, as it was almost impossible to extrude more than $5x10^6$ cells/mL by hand. Even with the Lipex extruder the pressure increased almost to 50 bar for the extrusion of $10x10^6$ cells/mL, therefore observed a bigger variation in particle yield. **b,** Sample weight loss during serial extrusion with the hand extruder normalized to the starting weight of the non-lysed sample (mean ± SD, n = 4). For this experiment 5.0 x 10^6 cells/mL were used.

Microscopy image analysis

Microscopy images were analysed using the open-source FIJI software with scripts programmed with Java language. First, the images obtained from the Nikon Ti-U microscope were split into the three separate channels (DAPI, TxRED, Bright Field (BF)) and saved separately as Tiff using following script:

```
input_path = getDir("choose directory"); //raw image files
locationDAPI = getDir("choose directory"); //folder to save channel 1 (DAPI)
locationTxRED = getDir("choose directory"); //folder to save channel 2 (TxRED)
locationBF = getDir("choose directory"); //folder to save channel 3 (BF)
fileList = getFileList(input_path);


for (i = 0; i < fileList.length ; i++) {
        complete_path = input_path + fileList[i];
        run("Bio-Formats", "open=[complete_path] autoscale color_mode=Default rois_import=[ROI manager] view=Hyperstack stack_order=XYCZT");
        title = getTitle(); //gets the name of the image
        print("title: " + title);
        run("Split Channels"); // splits image into separate channels
        selectWindow("C1-"+ title);
        saveAs("Tiff",locationDAPI + title + "_DAPI"); //adds "_DAPI" to the name of the image for channel 1
        selectWindow("C2-"+ title);
        saveAs("Tiff",locationTxRED + title + "_TxRED"); //adds "_TxRED" to the name of the image for ch. 2
        selectWindow("C3-"+ title);
        saveAs("Tiff",locationBF + title+ "_BF"); //adds "_BF" to the name of the image for ch. 3
        run("Close All"); //closes all windows opened by Fiji
}
```

After the images were separated into each channel, the histogram of every single TxRED image was checked. To get all histograms and save them as csv files following script was used:

```
nBins = 256;
input_path = getDir("choose directory"); //folder with the images of the corresponding channel
locationHistogram = getDir("choose directory"); //folder were all the histogram files should be saved (csv)
fileList = getFileList(input_path);

for (a = 0; a < fileList.length ; a++) {
        complete_path = input_path + fileList[a];
        open(complete_path);
        title = getTitle();
        print("title: " + title);

run("Clear Results");
row = 0;
getHistogram(values, counts, nBins); //Histograms for all images are gathered
for (i=0; i<nBins; i++) {
   setResult("Value", row, values[i]);
   setResult("Count", row, counts[i]);
   row++;
 }
updateResults();
saveAs("Results", locationHistogram + fileList[a] + "_histogram.csv"); //histograms are saved as csv
}
run("Close All");
```

The collected histograms were used to normalize the images by setting the max value (always background) to the value of 1300 [a.u.] (only for 10x images). Afterwards, the normalized images were used to analyse the total area of lipid droplets using following script:

```
title2 = "NVAXXX"; //name of experiment
```

```
input_path = getDir("choose directory"); // Folder with the normalized TxRED images
location = getDir("choose outputDir"); // Folder to save the result file (single images, as well as summary) (csv)
location1 = getDir("choose outputDir"); // Folder to save the mask created out of the image by Fiji
fileList = getFileList(input_path);
min_value = 1800; //min value of Threshold
max_value = 60000; //max value of Threshold

for (i = 0; i < fileList.length; i++) {
        complete_path = input_path + fileList[i];
        open(complete_path);
title = getTitle();
print("title: " + title);
setAutoThreshold("Default");
run("Threshold...");
setThreshold(min_value, max_value);
setOption("BlackBackground", false);
run("Convert to Mask"); //creates a mask to measure the average of the surface that is included in the threshold
selectWindow(title);
run("Analyze Particles...", "size=12-3000 pixel show=Outlines display clear summarize");
selectWindow(title);
saveAs("Tiff",location1 + title);
saveAs("results", location + fileList[i] + "_results.csv"); //saves the area of lipid droplets for each single image as csv
run("Close All");
}
Table.rename("Summary", "results");
saveAs("results", location + title2 + "_summary.csv"); //saves the area of lipid droplets for each single image in one summary csv file
```

The cell number was counted by using the DAPI channel images with following script:

```
title2 = "NVAXXX"; //name of experiment
input_path = getDir("choose directory"); // Folder with the DAPI images
location = getDir("choose outputDir"); // Folder to save the result file (single masks, as well as summary) (tif/csv)
```

```
location1 = getDir("choose outputDir"); // Folder to save the drawings created out of the image by Fiji
fileList = getFileList(input_path);


for (i = 0; i < fileList.length; i++) {
        complete_path = input_path + fileList[i];
        open(complete_path);
title = getTitle();
print("title: " + title);
setAutoThreshold("Huang dark");
setOption("BlackBackground", false);
run("Convert to Mask");
run("Fill Holes");
run("Watershed");
run("Analyze Particles...", "size=12-Infinity pixel show=Outlines display clear summarize");
saveAs("Tiff",location1 + title + "_drawing");
close();
selectWindow(title);
saveAs("Tiff",location + title);
close();
}
Table.rename("Summary", "results");
saveAs("results", location + title2 + "_summary.csv");
```

Finally, to calculate to analyse how much lipid droplets [μm^2] per cell was present (ORO FRI), the total area of lipid droplets was divided by the cell count of each single image. By using scripts, the image analysis could be scaled without losing time through manual processing.

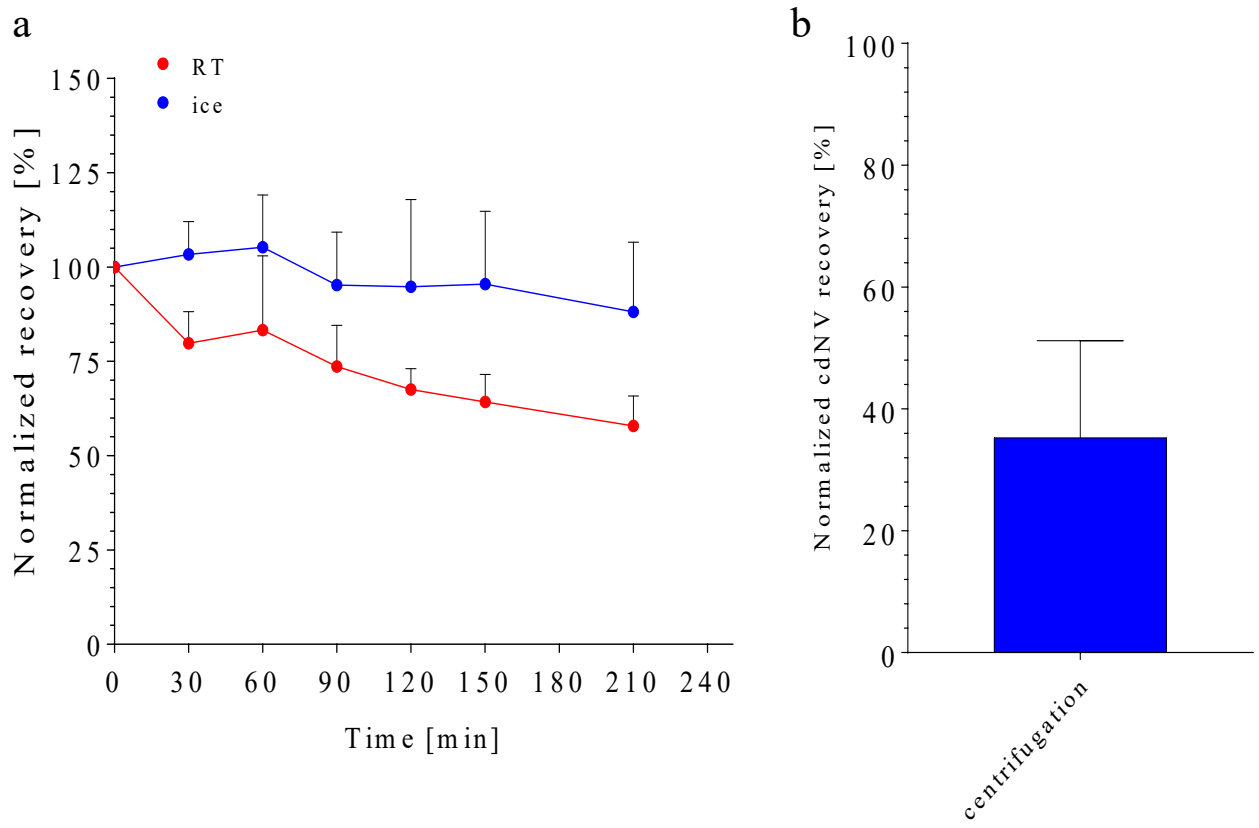

Figure A3.1. cell-derived nanovesicles (cdNV)stability and recovery after high-speed centrifugation.

a, Freshly extruded cdNVs were filtered (0.22 µm, regenerated cellulose) and stored in Axygen reaction tubes on ice or at room temperature (RT). The cdNV concentration was measured every 30 min and normalized to the starting amount. Particles are more stable on ice than at RT (mean ± SD, n = 2). **b,** cdNVs were centrifuged at 9'000 g for 30 min to remove aggregates. The pellet concentration was normalized to the starting amount (mean ± SD, n = 10). The particle recovery was very low, this could have several reasons such as coprecipitation during centrifugation. Also, the centrifuge could not be cooled and had to be performed at RT. Hence, after 30 min at least 25% particle removal was to be expected.

Table A3.1. Particle and protein recovery after size exclusion chromatography (SEC).

a

	Average [%]	SD [%]	SD%	n
fr. 6	32.6	15.6	47.8	9
fr. 7	44.4	19.7	44.2	9
fr. 8	8.4	6.7	79.6	9
fr. 6 + 7	77.0	16.7	21.7	9

b

	Average [%]	SD [%]	SD%	n
fr. 6	4.2	1.6	36.8	8
fr. 7	5.1	1.6	32.2	8
fr. 8	2.1	1.0	49.4	8
fr. 6 + 7	8.7	2.5	28.5	8

a, The recovery of cell-derived nanovesicles (cdNVs) after size exclusion chromatography (SEC) in the three primary particle fractions (fractions 6-8) was measured. The average and standard deviation (SD) of nine replicates are presented along with the percentage value of the SD from the average (SD/average * 100%) to illustrate that the SD was small when fractions 6 and 7 were combined, and that the variation in individual fractions was primarily due to manual fraction collection. **b,** The protein recovery was evaluated in the three primary particle fractions (fractions 6-8) after size exclusion chromatography (SEC). The low protein content indicated effective particle purification. The protein levels appeared to be associated with the particles, as they declined and then increased again from fraction 11 onwards.

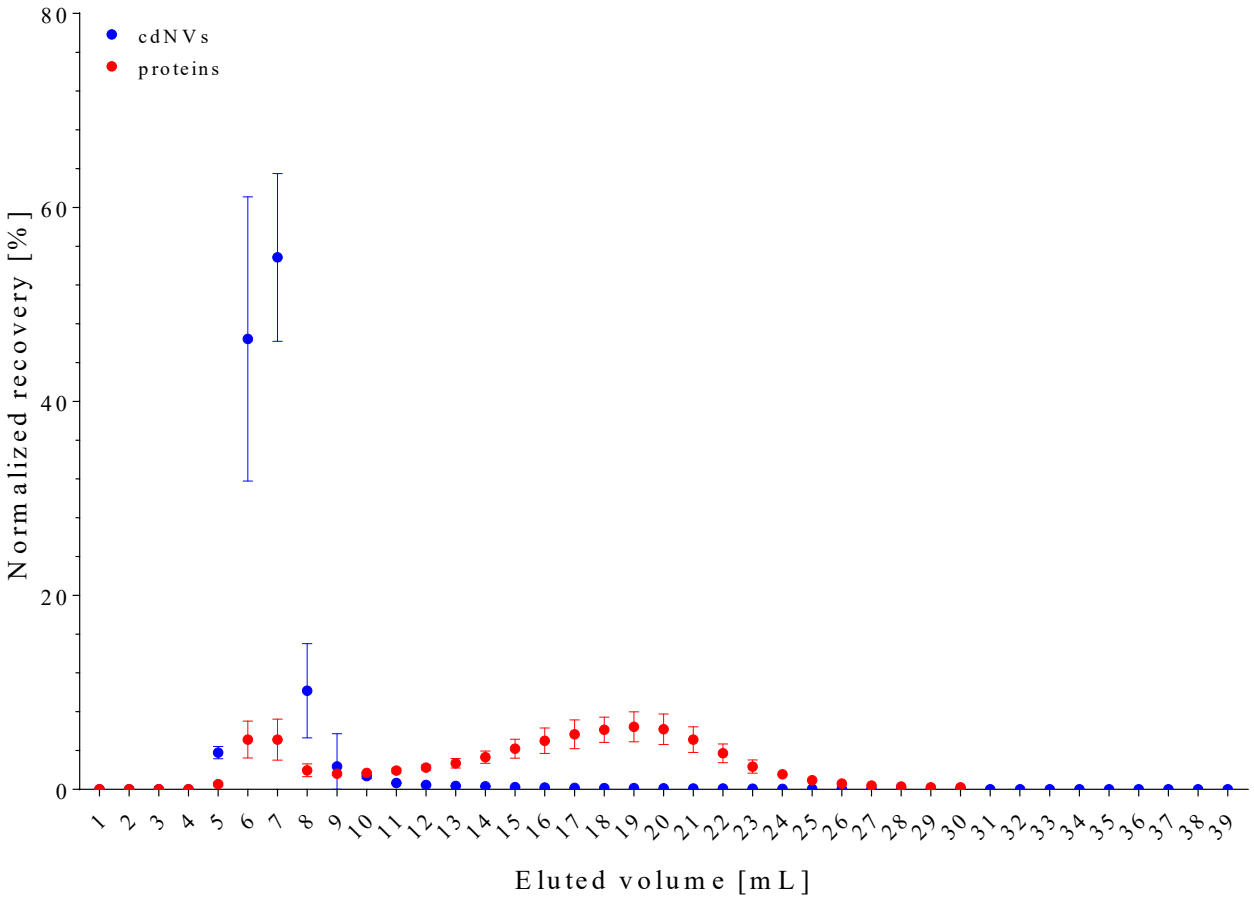

Figure A3.2. Scaling of size exclusion chromatography (SEC).

By maintaining the loading volume at 2 mL, the loaded particle and protein amount was augmented from 2.3 x 10^{11} ± 0.7 x 10^{11} cell-derived nanovesicles (cdNVs) and 1145.00 ± 188.13 µg protein to 8.0 x 10^{11} cdNVs and 2240 µg protein, indicating that SEC can separate soluble proteins from particles even at high concentrations (mean ± SD, n = 2-3).

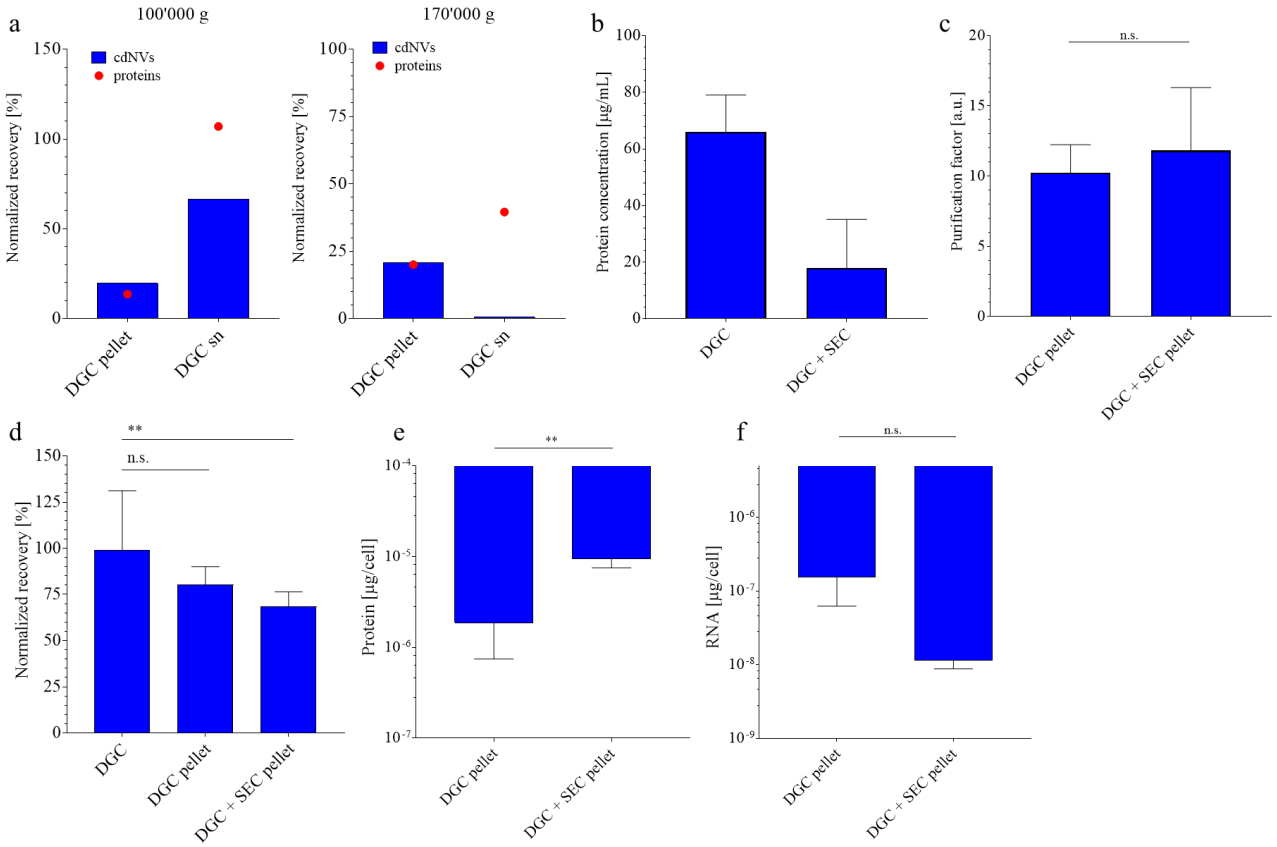

Figure A3.3. Evaluation of ultracentrifugation (UC).

a, Recovery of cell-derived nanovesicles (cdNVs) and proteins in the pellet and supernatant (sn) of samples after UC at two different speeds (100'000 g and 170'000 g) that underwent pre-purification by density gradient ultracentrifugation (DGC) (n = 1). UC with 100'000 g led to most particles remaining in the sn and UC with 170'000 g led to particle bursting. **b,** Protein concentration in the sample after DGC and after DGC + size exclusion chromatography (SEC) prior UC (mean ± SD, n = 3). **c,** The purification factor (pf) was calculated with following formula:

$$pf = \frac{\frac{cdNVs(pre\ purification)}{protein\ (pre\ purification)[\mu g]}}{\frac{cdNVs(post\ purification)}{protein\ (post\ purification)[\mu g]}}$$

With the pf the purification efficiency of the two purification processes could be compared. Including SEC in the purification process barely increased the pf, this was due to the decreased particle yield compared to DGC + UC only (mean ± SD, n ≥ 3) (Welch's t-test). **d,** The stability of cell-derived nanovesicles (cdNVs), which were filtered (0.22 µm regenerated cellulose), was investigated after subjecting them to DGC, DGC + UC (DGC pellet), and DGC + SEC + UC (DGC + SEC pellet) purification processes. The concentration of cdNVs was measured before and after 14 h (overnight) of storage at 4 °C. The results indicate that the purity of cdNVs is inversely proportional to their stability (mean ± SD, n ≥ 4) (Ordinary one-way ANOVA with Tukey post hoc test; ** p- value = 0.0097). **e,** The protein content in the pellet and sn obtained after DGC and UC was measured and normalized to the number of LX-2 cells used. The sn showed a higher protein content compared to the cdNV pellet. (mean ± SD, n = 3) (Ordinary one-way ANOVA with Tukey post hoc test; ** p-value = 0.007). **f,** The RNA content in the pellet and sn obtained after DGC and UC was measured and normalized to the number of LX-2 cells used. The cdNV pellet tends to have a higher RNA content compared to the sn. (mean ± SD, n = 3) (Ordinary one-way ANOVA).

Chapter 4 supplementary information

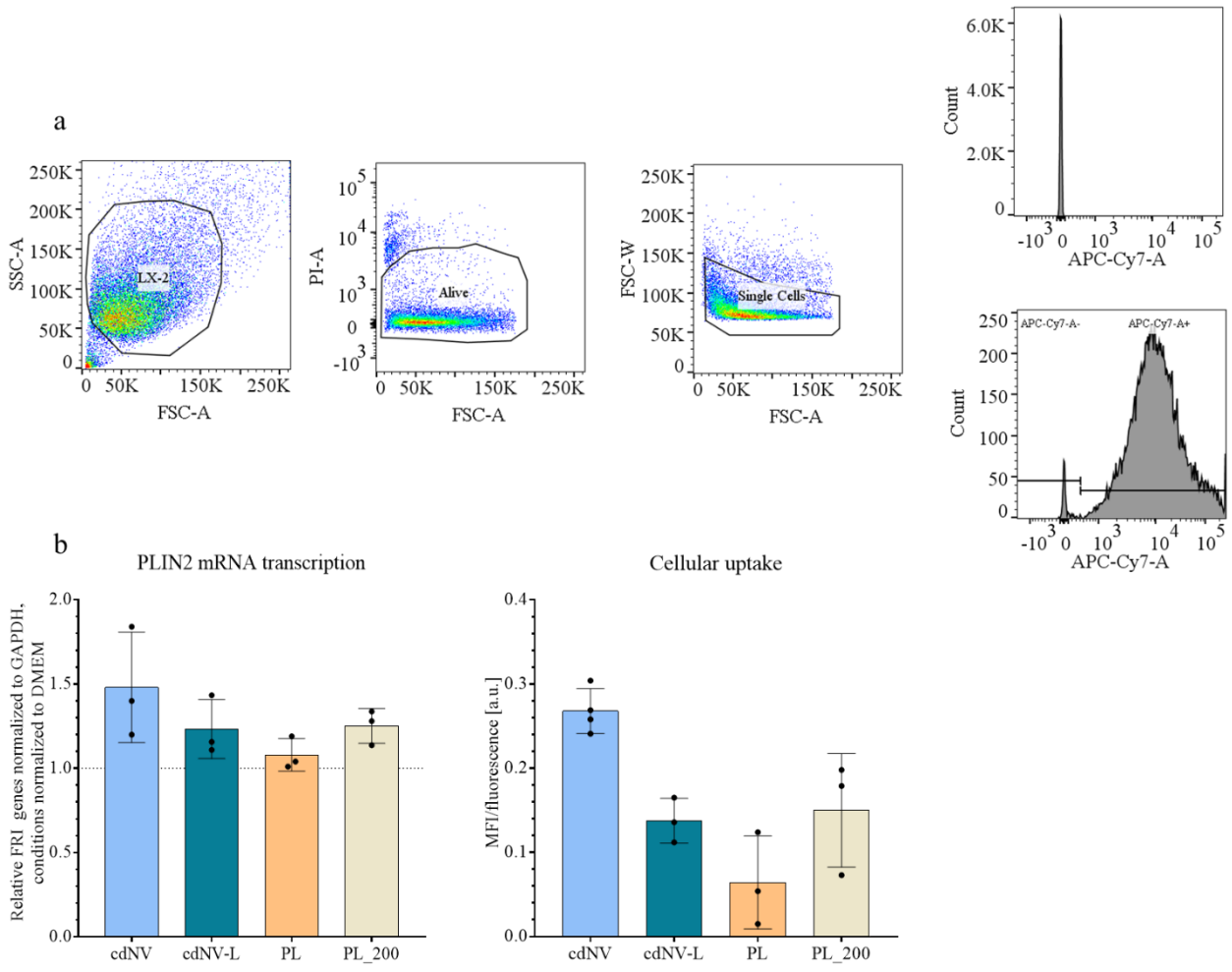

Figure A4.1. Cellular particle uptake.
a, Gating strategy used to analyse the FACS data by FlowJo. First plotted SSC-A vs FSC-A to select the LX-2 cells (in gate: 75.7% ± 4.9% for naïve cells; 73.5% ± 4.5% for perpetuated cells). Secondly, selected the alive cells by plotting PI-A against FSC-A (in gate: 94.0% ± 10.4% for naïve cells; 96.4% ± 4.0% for perpetuated cells) Thirdly excluded all aggregates by selectin only single cells through plotting FSC-W against FSC-A (in gate: 92.0% ± 1.6% for naïve cells; 94.8% ± 1.5% for perpetuated cells). Last, plotted the DiR positive cells in a histogram against APC-Cy7-A. To select the DiR-positive cells, treated LX-2 cells with non-labelled particles and therefore measured no fluorescence with the APC-Cy7 filter. **b,** Comparison of the PLIN2 mRNA transcription change in perpetuated LX-2 cells after treatment with cdNV, cdNV-L, PL, and PL_200 with the cellular particle uptake differences in perpetuated LX-2 cells. Enhanced particle uptake led to bigger PLIN2 mRNA expression increase (mean ± SD, n ≤ 3).

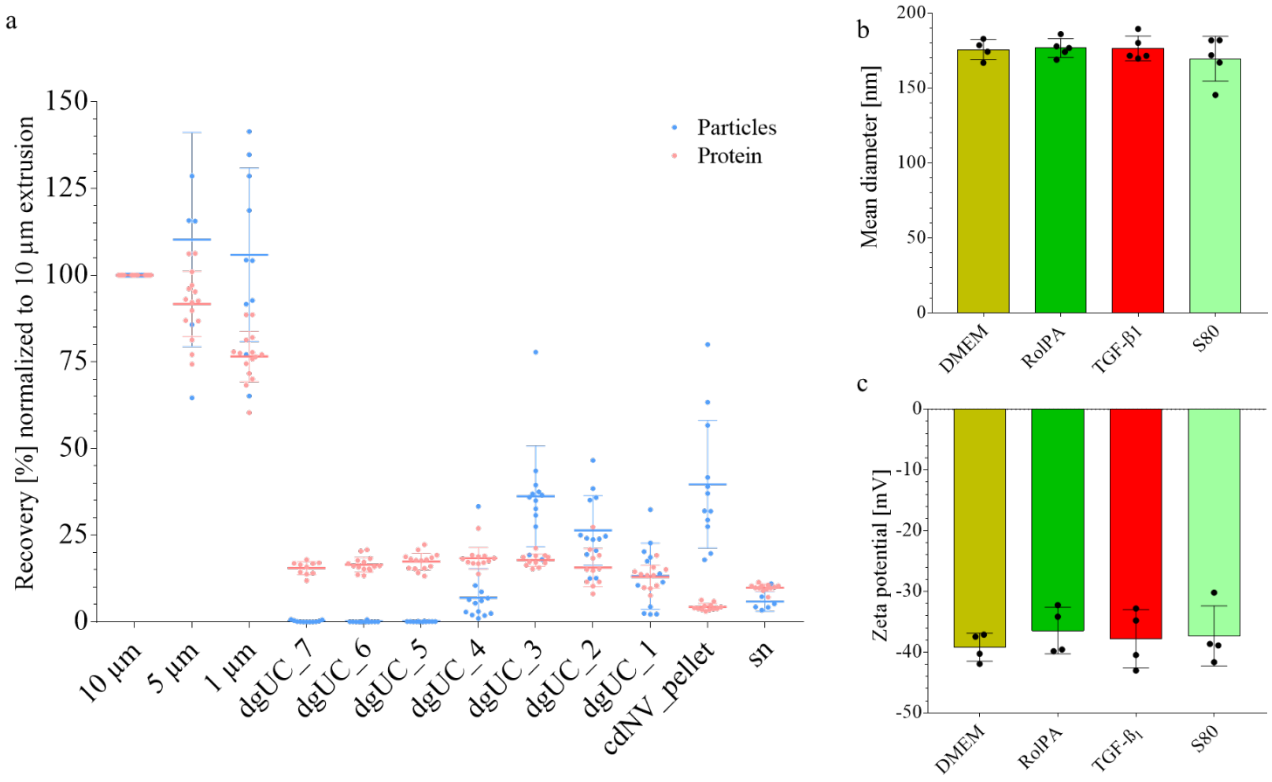

Figure A4.2. Purification and characterization of cdNVs.
a, Particle and protein recovery during purification of cdNVs normalized to values obtained after 10 µm extrusion (dgUC, density-gradient ultracentrifugation fractions) (mean ± SD, n ≤ 6). **b,** Mean diameter of purified cdNVs derived from differently treated LX-2 cells (mean ± SD, n ≤ 4). **c,** Zeta potential of purified cdNVs derived from differently treated LX-2 cells (mean ± SD, n = 4).

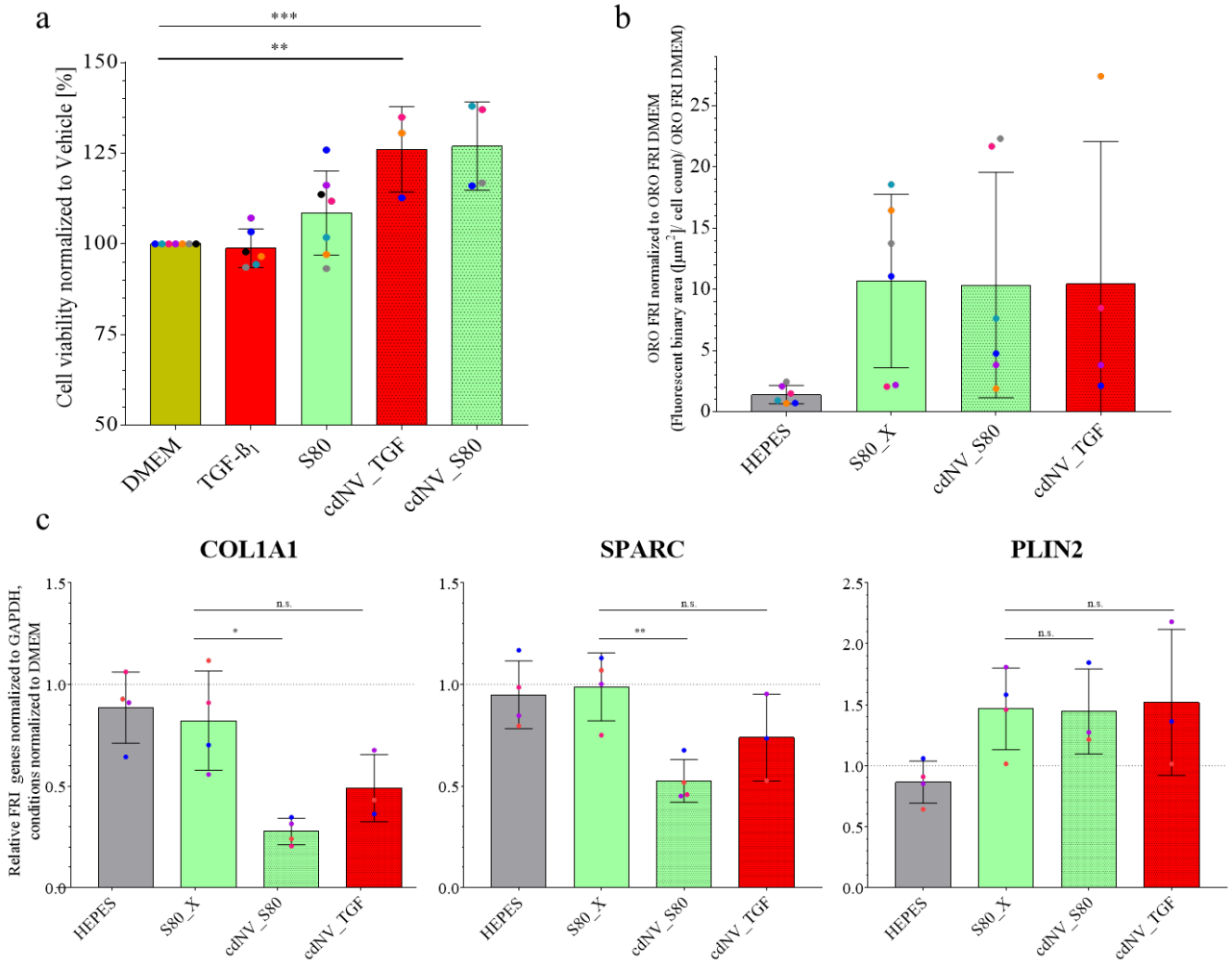

Figure A4.3. Effect of cdNVs on naïve LX-2 cells.
a, Cell viability of naïve LX-2 cells treated with 4.5 x 10^{10} cdNVs/mL derived from TGF-β1 or S80 treated LX-2 cells (mean ± SD, n ≤ 3) (p-values from ordinary one-way ANOVA with post post-hoc Tukey test in supplementary table SY5) **b,** ORO fluorescence normalized to the cell count in the DAPI field (FRI) and normalized to the ORO FRI of DMEM. Comparison of naïve LX-2 cells treated either with 4.5 x 10^{10} S80 liposomes/mL, or with 4.5 x 10^{10} cdNVs/mL (mean ± SD, n ≤ 4) (p-values from ordinary one-way ANOVA with post post-hoc Tukey test in supplementary table SY) **c,** Relative mRNA transcription in naïve LX-2 cells of three fibrosis markers (COL1A1, SPARC, PLIN2) normalized to GAPDH mRNA transcription and normalized to the DMEM condition after treatment with either 4.5 x 10^{10} cdNVs/mL or 4.5 x 10^{10} S80 liposomes/mL (mean ± SD, n ≤ 3) (p-values from ordinary one-way ANOVA with post post-hoc Tukey test in supplementary tables SY2/3/4)

Table A4.1. Protein amount of cdNV particles.

	cdNVs/mL	Protein concentration [µg/mL]	SD [µg/mL]	Protein [µg]	SD [µg]
A	1.5E+10	19.5	6.7	9.8	3.4
B	3.0E+09	3.9	1.3	2.0	0.7
C	6.0E+08	0.8	0.3	0.4	0.1

The amount of protein present in each of the three tested cdNV dosages (mean ± SD, n = 13). Total protein amount of cdNVs, obtained with a micro-BCA assay kit, was divided by the total particle amount of cdNVs, obtained through NTA, and multiplied by the particle amount of the respective dosages A, B, and C.

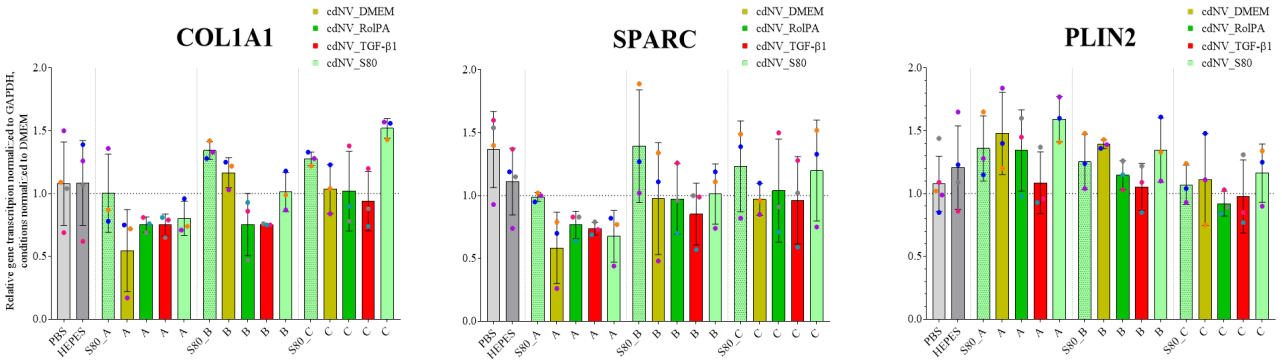

Figure A4.4. Comparison of cdNVs and S80 liposomes induced response in activated LX-2 cells. Relative mRNA transcription in TGF-β1 activated LX-2 cells of three fibrosis markers (COL1A1, SPARC, PLIN2) normalized to GAPDH mRNA transcription and normalized to the DMEM condition after treatment with three different cdNV and S80 liposome concentrations (A = 1.5 x 10^{10} particles/mL; B = 3.0 x 10^{09} particles/mL; C = 6.0 x 10^{08} particles/mL) (mean ± SD, n ≤ 3) (p-values from ordinary one-way ANOVA with post post-hoc Tukey test in supplementary tables SZ2/3/4)
The anti-fibrotic response in activated LX-2 cells is stronger after cdNV treatment compared to S80 liposome treatment.

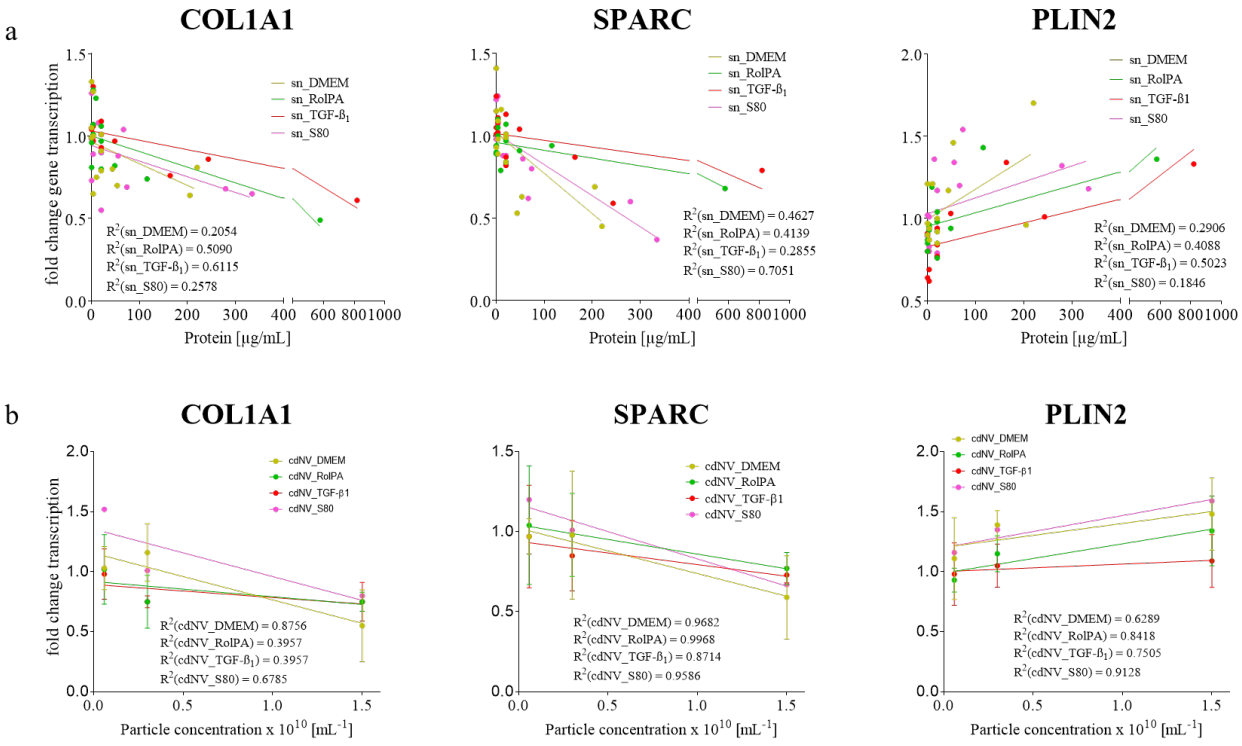

Figure A4.5. Correlation between mRNA expression and sn respectively cdNV concentration.
a, Linear correlation of relative mRNA transcription in TGF-β1 activated LX-2 cells of three fibrosis markers (COL1A1, SPARC, PLIN2) normalized to GAPDH mRNA transcription and normalized to the DMEM condition after treatment with sn containing increasing protein amounts (mean ± SD, n ≤ 3).
b, Linear correlation of relative mRNA transcription in TGF-β1 activated LX-2 cells of three fibrosis markers (COL1A1, SPARC, PLIN2) normalized to GAPDH mRNA transcription and normalized to the DMEM condition after treatment with three different cdNV concentrations (A = 1.5 x 10^{10} cdNVs/mL; B = 3.0 x 10^{09} cdNVs/mL; C = 6.0 x 10^{08} cdNVs/mL) (mean ± SD, n = 3).
Overall, cdNVs show a higher correlation compared to sn. As the mechanism of activity and active substances are unknown a linear correlation based on protein concentration alone might not be the best fit for the sn.

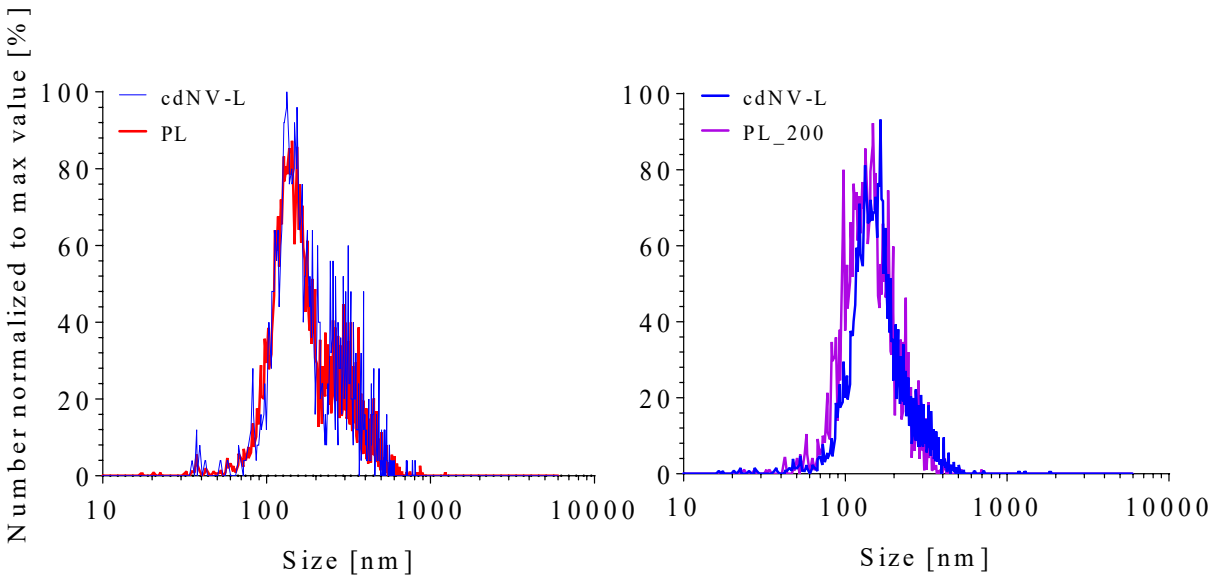

Figure A4.6. Characterization and activity of proteoliposomes.
Size distribution of cell-derived nanovesicle (cdNV) liposomes (cdNV-L) compared to proteoliposomes with low and high protein corona contents (PL and PL_200) (mean ± SD, n = 3).

Statistics

All p-values of post-hoc Tukey tests are found under https://doi.org/10.5281/zenodo.7794261.

Chapter 5 supplementary information

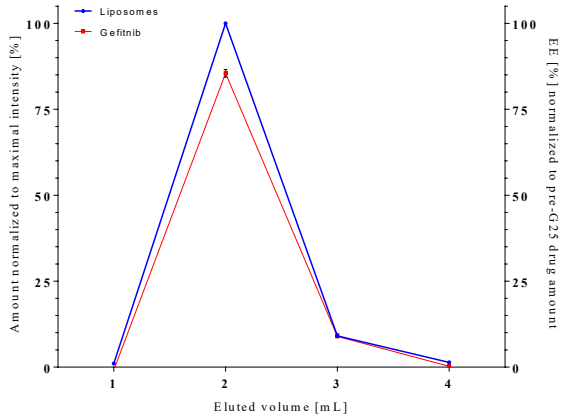

Figure A5.1. Elution profile of Liposomes (MLVs) and gefitinib from G-25 column (mean ± SD, n ≥ 3).

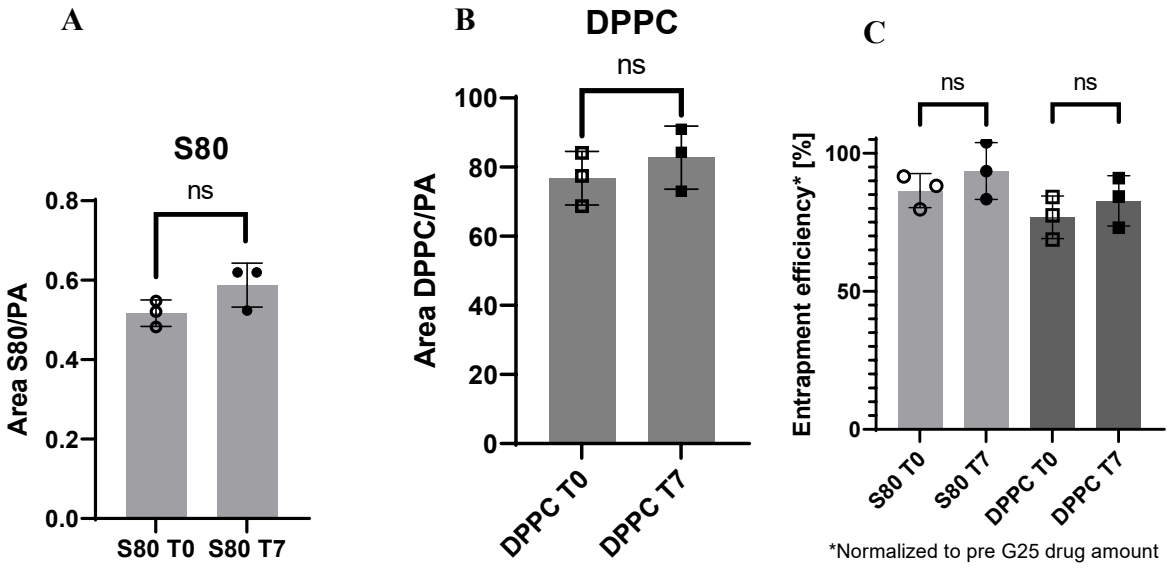

Figure A5.2. A: Stability studies of S80 MLVs. **B:** Stability studies of DPPC MLVs. **C:** Encapsulation efficiency of gefitinib over time.

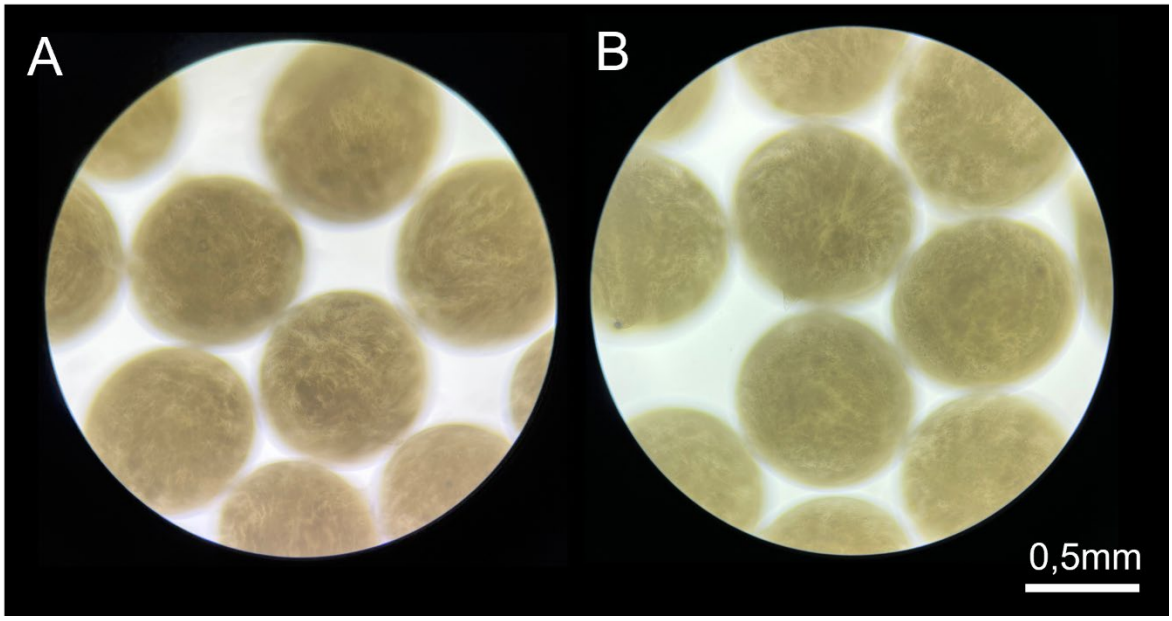

Figure A5.3. 6Injectability of beads, A: 3D printed beads (0.5 mM gefitinib; 15 mM S80; 3% Alg) before injecting. B: 3D printed beads (0.5 mM gefitinib; 15 mM S80; 3% Alg) after injection through an 18G needle.

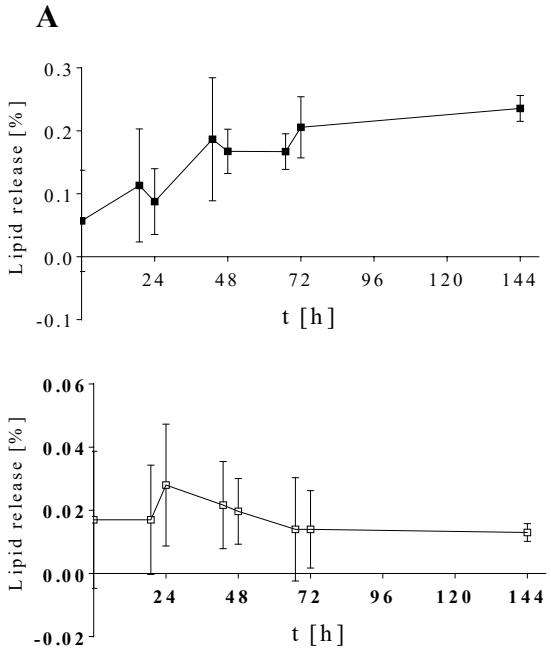

Figure A5.4. A: S80 SUV release from microbeads measured by DiD fluorescence (15 mM S80; 3% Alg; 5 nM DiD). **B:** DPPC MLV release from microbeads measured by DiD fluorescence (15 mM S80; 3% Alg; 5 nM DiD). Results normalized to cumulative content after recovery of the lipids (mean ± SD, $n \geq 3$).

Abbreviations

ADRP	Adipose differentiation-related protein
cdNVs	Cell-derived Nanovesicles
COL1A1	Collagen Type I Alpha 1 Chain
DAPI	4′,6-diamidino-2-phenylindole
DGC	Density gradient ultracentrifugation
DLS	Dynamic light scattering
DPPC	Dipalmitoylphosphatidylcholin
EVs	Extracellular vesicles
FBS	Fetal Bovine serum
GAPDH	Glyceraldehyde 3-phosphate dehydrogenase
HEPES	4-(2-hydroxyethyl)-1-piperazineethanesulfonic acid buffer
HSCs	Hepatic stellate cells
IP	Intraperitoneal
NAFLD	Non-alcoholic fatty liver disease
NASH	Non-alcoholic steatohepatitis
NTA	Nanoparticle tracking analysis
ORO	Oil Red O

PBS	Phosphate buffered saline
PLIN2	Perilipin 2
PSF	Peritoneal simulation fluid
RC	Regenerated cellulose
RolPA	Retinol + palmitic acid
SEC	Size-exclusion chromatography
sn	Supernatant
SPARC	Secreted protein acidic and rich in cysteine
S80	Soybean phospholipid with >75% PC
TGF-β_1	Transforming growth factor beta 1
Treatment: DMEM	Serum free cell culture medium
Treatment: HEPES	HEPES 1 mM in DMEM, negative control to S80
Treatment: PBS	PBS in DMEM, negative control to supernatant
Treatment: RolPA	10/300 μM Rol/PA in DMEM
Treatment: S80	S80 5 mM S80 in DMEM
Treatment: TGF-β_1	10 ng/mL TGF-β_1 in DMEM
UC	Ultracentrifugation

References

1. Wolf DC. **Evaluation of the Size, Shape, and Consistency of the Liver**. In: *Clinical Methods: The History, Physical, and Laboratory Examinations*. Walker HK, Hall WD, Hurst JW (editors). Boston: Butterworths Copyright © 1990, Butterworth Publishers, a division of Reed Publishing.; 1990.

2. Abdel-Misih SR, Bloomston M. **Liver anatomy**. *Surg Clin North Am* 2010; 90(4):643-653.

3. Hermoye L, Laamari-Azjal I, Cao Z, Annet L, Lerut J, Dawant BM, et al. **Liver segmentation in living liver transplant donors: comparison of semiautomatic and manual methods**. *Radiology* 2005; 234(1):171-178.

4. Trefts E, Gannon M, Wasserman DH. **The liver**. *Current Biology* 2017; 27(21):R1147-R1151.

5. Manco R, Leclercq IA, Clerbaux LA. **Liver Regeneration: Different Sub-Populations of Parenchymal Cells at Play Choreographed by an Injury-Specific Microenvironment**. *Int J Mol Sci* 2018; 19(12):4115.

6. Damm G, Pfeiffer E, Burkhardt B, Vermehren J, Nussler AK, Weiss TS. **Human parenchymal and non-parenchymal liver cell isolation, culture and characterization**. *Hepatol Int* 2013; 7(4):951-958.

7. Plumlee KH. **Chapter 11 - Hepatobiliary System**. In: *Clinical Veterinary Toxicology*. Plumlee KH (editor). Saint Louis: Mosby; 2004. pp. 61-68.

8. Carneiro C, Brito J, Bilreiro C, Barros M, Bahia C, Santiago I, et al. **All about portal vein: a pictorial display to anatomy, variants and physiopathology**. *Insights Imaging* 2019; 10(1):38.

9. Gibert-Ramos A, Sanfeliu-Redondo D, Aristu-Zabalza P, Martinez-Alcocer A, Gracia-Sancho J, Guixe-Muntet S, et al. **The Hepatic Sinusoid in Chronic Liver Disease: The Optimal Milieu for Cancer**. *Cancers (Basel)* 2021; 13(22):5719.

10. Rocha FG. **Liver blood flow from Blumgart's Surgery of the Liver, Pancreas and Biliary Tract (fifth edition)**. 2012; 5:74-86.e75.

11. Sera T, Sumii T, Fujita R, Kudo S. **Effect of shear stress on the migration of hepatic stellate cells**. *In Vitro Cell Dev Biol Anim* 2018; 54(1):11-22.

12. Willekens FL, Werre JM, Kruijt JK, Roerdinkholder-Stoelwinder B, Groenen-Dopp YA, van den Bos AG, et al. **Liver Kupffer cells rapidly remove red blood cell-derived vesicles from the circulation by scavenger receptors**. *Blood* 2005; 105(5):2141-2145.

13. Nguyen P, Leray V, Diez M, Serisier S, Le Bloc'h J, Siliart B, et al. **Liver lipid metabolism**. *J Anim Physiol Anim Nutr (Berl)* 2008; 92(3):272-283.

14. Gao B, Jeong WI, Tian Z. **Liver: An organ with predominant innate immunity**. *Hepatology* 2008; 47(2):729-736.

15. Oliva-Vilarnau N, Hankeova S, Vorrink SU, Mkrtchian S, Andersson ER, Lauschke VM. **Calcium Signaling in Liver Injury and Regeneration**. *Front Med (Lausanne)* 2018; 5:192.

16. Gu X, Manautou JE. **Molecular mechanisms underlying chemical liver injury**. *Expert Rev Mol Med* 2012; 14:e4.

17. Klaunig JE, Li X, Wang Z. **Role of xenobiotics in the induction and progression of fatty liver disease**. *Toxicol Res (Camb)* 2018; 7(4):664-680.

18. Scalone L, Fagiuoli S, Ciampichini R, Gardini I, Bruno R, Pasulo L, et al. **The societal burden of chronic liver diseases: results from the COME study**. *BMJ Open Gastroenterol* 2015; 2(1):e000025.

19. Cordero-Espinoza L, Huch M. **The balancing act of the liver: tissue regeneration versus fibrosis**. *J Clin Invest* 2018; 128(1):85-96.

20. Terai S, Tsuchiya A. **Status of and candidates for cell therapy in liver cirrhosis: overcoming the "point of no return" in advanced liver cirrhosis**. *J Gastroenterol* 2017; 52(2):129-140.

21. Bourbonnais E, Raymond VA, Ethier C, Nguyen BN, El-Leil MS, Meloche S, et al. **Liver fibrosis protects mice from acute hepatocellular injury**. *Gastroenterology* 2012; 142(1):130-139 e134.

22. Pellicoro A, Ramachandran P, Iredale JP, Fallowfield JA. **Liver fibrosis and repair: immune**

regulation of wound healing in a solid organ. *Nat Rev Immunol* 2014; 14(3):181-194.
23. Asrani SK, Devarbhavi H, Eaton J, Kamath PS. **Burden of liver diseases in the world**. *J Hepatol* 2019; 70(1):151-171.
24. Poole LG, Dolin CE, Arteel GE. **Organ-Organ Crosstalk and Alcoholic Liver Disease**. *Biomolecules* 2017; 7(3):62.
25. Ching-Yeung Yu B, Kwok D, Wong VW. **Magnitude of Nonalcoholic Fatty Liver Disease: Eastern Perspective**. *J Clin Exp Hepatol* 2019; 9(4):491-496.
26. Trautwein C, Friedman SL, Schuppan D, Pinzani M. **Hepatic fibrosis: Concept to treatment**. *J Hepatol* 2015; 62(1 Suppl):S15-24.
27. Cotter TG, Rinella M. **Nonalcoholic Fatty Liver Disease 2020: The State of the Disease**. *Gastroenterology* 2020; 158(7):1851-1864.
28. Buzzetti E, Pinzani M, Tsochatzis EA. **The multiple-hit pathogenesis of non-alcoholic fatty liver disease (NAFLD)**. *Metabolism* 2016; 65(8):1038-1048.
29. Guarino M, Kumar P, Felser A, Terracciano LM, Guixe-Muntet S, Humar B, et al. **Exercise Attenuates the Transition from Fatty Liver to Steatohepatitis and Reduces Tumor Formation in Mice**. *Cancers (Basel)* 2020; 12(6):1407.
30. Schwabe RF, Tabas I, Pajvani UB. **Mechanisms of Fibrosis Development in Nonalcoholic Steatohepatitis**. *Gastroenterology* 2020; 158(7):1913-1928.
31. Yu S, Wang J, Zheng H, Wang R, Johnson N, Li T, et al. **Pathogenesis from Inflammation to Cancer in NASH-Derived HCC**. *J Hepatocell Carcinoma* 2022; 9:855-867.
32. Hashimoto E, Tokushige K, Ludwig J. **Diagnosis and classification of non-alcoholic fatty liver disease and non-alcoholic steatohepatitis: Current concepts and remaining challenges**. *Hepatol Res* 2015; 45(1):20-28.
33. Ress C, Kaser S. **Mechanisms of intrahepatic triglyceride accumulation**. *World J Gastroenterol* 2016; 22(4):1664-1673.
34. Grossini E, Garhwal DP, Calamita G, Romito R, Rigamonti C, Minisini R, et al. **Exposure to Plasma From Non-alcoholic Fatty Liver Disease Patients Affects Hepatocyte Viability, Generates Mitochondrial Dysfunction, and Modulates Pathways Involved in Fat Accumulation and Inflammation**. *Front Med (Lausanne)* 2021; 8:693997.
35. Smith-Cortinez N, Fagundes RR, Gomez V, Kong D, de Waart DR, Heegsma J, et al. **Collagen release by human hepatic stellate cells requires vitamin C and is efficiently blocked by hydroxylase inhibition**. *FASEB J* 2021; 35(2):e21219.
36. Friedman SL. **Hepatic stellate cells: protean, multifunctional, and enigmatic cells of the liver**. *Physiol Rev* 2008; 88(1):125-172.
37. Trivedi P, Wang S, Friedman SL. **The Power of Plasticity-Metabolic Regulation of Hepatic Stellate Cells**. *Cell Metab* 2021; 33(2):242-257.
38. Lemoinne S, Cadoret A, El Mourabit H, Thabut D, Housset C. **Origins and functions of liver myofibroblasts**. *Biochim Biophys Acta* 2013; 1832(7):948-954.
39. Atzori L, Poli G, Perra A. **Hepatic stellate cell: a star cell in the liver**. *Int J Biochem Cell Biol* 2009; 41(8-9):1639-1642.
40. Puche JE, Saiman Y, Friedman SL. **Hepatic stellate cells and liver fibrosis**. *Compr Physiol* 2013; 3(4):1473-1492.
41. Häussinger D, Kordes C. **Space of Disse: a stem cell niche in the liver**. *Biological Chemistry* 2019; 401(1):81-95.
42. Hernandez-Gea V, Friedman SL. **Pathogenesis of Liver Fibrosis**. *Annual Review of Pathology: Mechanisms of Disease* 2011; 6(1):425-456.
43. Friedman SL. **Evolving challenges in hepatic fibrosis**. *Nature Reviews Gastroenterology & Hepatology* 2010; 7(8):425-436.
44. Lee YA, Wallace MC, Friedman SL. **Pathobiology of liver fibrosis: a translational success story**. *Gut* 2015; 64(5):830-841.
45. Valentino G, Zivko C, Weber F, Brulisauer L, Luciani P. **Synergy of Phospholipid-Drug Formulations Significantly Deactivates Profibrogenic Human Hepatic Stellate Cells**. *Pharmaceutics* 2019; 11(12):676.
46. Kisseleva T, Brenner DA. **Hepatic stellate cells and the reversal of fibrosis**. *J Gastroenterol Hepatol* 2006; 21 Suppl 3:S84-87.

47. Montano-Loza AJ, Thandassery RB, Czaja AJ. **Targeting Hepatic Fibrosis in Autoimmune Hepatitis**. *Dig Dis Sci* 2016; 61(11):3118-3139.
48. Chang TT, Liaw YF, Wu SS, Schiff E, Han KH, Lai CL, et al. **Long-term entecavir therapy results in the reversal of fibrosis/cirrhosis and continued histological improvement in patients with chronic hepatitis B**. *Hepatology* 2010; 52(3):886-893.
49. Gundermann KJ, Gundermann S, Drozdzik M, Mohan Prasad VG. **Essential phospholipids in fatty liver: a scientific update**. *Clin Exp Gastroenterol* 2016; 9:105-117.
50. Fex G. **Metabolism of phosphatidyl choline, phosphatidyl ethanolamine and sphingomyelin in regenerating rat liver.** . *Biochimica et Biophysica Acta (BBA) - Lipids and Lipid Metabolism* 1971; 231(1):161–169.
51. van Hoogevest P, Wendel A. **The use of natural and synthetic phospholipids as pharmaceutical excipients**. *Eur J Lipid Sci Technol* 2014; 116(9):1088-1107.
52. Ikeda R, Ishii K, Hoshikawa Y, Azumi J, Arakaki Y, Yasui T, et al. **Reactive oxygen species and NADPH oxidase 4 induced by transforming growth factor beta1 are the therapeutic targets of polyenylphosphatidylcholine in the suppression of human hepatic stellate cell activation**. *Inflamm Res* 2011; 60(6):597-604.
53. Aleynik SI, Lieber CS. **Polyenylphosphatidylcholine corrects the alcohol-induced hepatic oxidative stress by restoring s-adenosylmethionine**. *Alcohol Alcohol* 2003; 38(3):208-212.
54. Lee TF, Mak KM, Rackovsky O, Lin YL, Kwong AJ, Loke JC, et al. **Downregulation of hepatic stellate cell activation by retinol and palmitate mediated by adipose differentiation-related protein (ADRP)**. *J Cell Physiol* 2010; 223(3):648-657.
55. Xu L, Hui AY, Albanis E, Arthur MJ, O'Byrne SM, Blaner WS, et al. **Human hepatic stellate cell lines, LX-1 and LX-2: new tools for analysis of hepatic fibrosis**. *Gut* 2005; 54(1):142-151.
56. van Niel G, D'Angelo G, Raposo G. **Shedding light on the cell biology of extracellular vesicles**. *Nat Rev Mol Cell Biol* 2018; 19(4):213-228.
57. Tenchov R, Sasso JM, Wang X, Liaw WS, Chen CA, Zhou QA. **Exosomes horizontal line Nature's Lipid Nanoparticles, a Rising Star in Drug Delivery and Diagnostics**. *ACS Nano* 2022; 16(11):17802-17846.
58. Tricarico C, Clancy J, D'Souza-Schorey C. **Biology and biogenesis of shed microvesicles**. *Small GTPases* 2017; 8(4):220-232.
59. Pan BT, Teng K, Wu C, Adam M, Johnstone RM. **Electron microscopic evidence for externalization of the transferrin receptor in vesicular form in sheep reticulocytes**. *J Cell Biol* 1985; 101(3):942-948.
60. Gurung S, Perocheau D, Touramanidou L, Baruteau J. **The exosome journey: from biogenesis to uptake and intracellular signalling**. *Cell Commun Signal* 2021; 19(1):47.
61. Cunnane EM, Weinbaum JS, O'Brien FJ, Vorp DA. **Future Perspectives on the Role of Stem Cells and Extracellular Vesicles in Vascular Tissue Regeneration**. *Frontiers in cardiovascular medicine* 2018; 5:86.
62. Stahl PD, Raposo G. **Extracellular Vesicles: Exosomes and Microvesicles, Integrators of Homeostasis**. *Physiology (Bethesda)* 2019; 34(3):169-177.
63. Herrmann IK, Wood MJA, Fuhrmann G. **Extracellular vesicles as a next-generation drug delivery platform**. *Nat Nanotechnol* 2021; 16(7):748-759.
64. Thery C, Witwer KW, Aikawa E, Alcaraz MJ, Anderson JD, Andriantsitohaina R, et al. **Minimal information for studies of extracellular vesicles 2018 (MISEV2018): a position statement of the International Society for Extracellular Vesicles and update of the MISEV2014 guidelines**. *J Extracell Vesicles* 2018; 7(1):1535750.
65. Pinheiro A, Silva AM, Teixeira JH, Gonçalves RM, Almeida MI, Barbosa MA, et al. **Extracellular vesicles: intelligent delivery strategies for therapeutic applications**. *J Control Release* 2018; 289:56-69.
66. Vader P, Mol EA, Pasterkamp G, Schiffelers RM. **Extracellular vesicles for drug delivery**. *Adv Drug Deliv Rev* 2016; 106(Pt A):148-156.
67. Zhang Y, Liu Y, Liu H, Tang WH. **Exosomes: biogenesis, biologic function and clinical potential**. *Cell Biosci* 2019; 9:19.

68. Hirshman BR, Kras RT, Akers JC, Carter BS, Chen CC. **Chapter Two - Extracellular Vesicles in Molecular Diagnostics: An Overview with a Focus on CNS Diseases**. In: *Advances in Clinical Chemistry*. Makowski GS (editor): Elsevier; 2016. pp. 37-53.
69. Fiore E, Dominguez LM, Bayo J, Malvicini M, Atorrasagasti C, Rodriguez M, et al. **Human umbilical cord perivascular cells-derived extracellular vesicles mediate the transfer of IGF-I to the liver and ameliorate hepatic fibrogenesis in mice**. *Gene Ther* 2019; 27(1-2):62-73.
70. Lv K, Li Q, Zhang L, Wang Y, Zhong Z, Zhao J, et al. **Incorporation of small extracellular vesicles in sodium alginate hydrogel as a novel therapeutic strategy for myocardial infarction**. *Theranostics* 2019; 9(24):7403-7416.
71. Rezaie J, Feghhi M, Etemadi T. **A review on exosomes application in clinical trials: perspective, questions, and challenges**. *Cell Communication and Signaling* 2022; 20(1):145.
72. Osteikoetxea X, Silva A, Lazaro-Ibanez E, Salmond N, Shatnyeva O, Stein J, et al. **Engineered Cas9 extracellular vesicles as a novel gene editing tool**. *J Extracell Vesicles* 2022; 11(5):e12225.
73. Han Y, Jones TW, Dutta S, Zhu Y, Wang X, Narayanan SP, et al. **Overview and Update on Methods for Cargo Loading into Extracellular Vesicles**. *Processes (Basel)* 2021; 9(2).
74. Safdari Y, Ahmadzadeh V, Khalili M, Jaliani HZ, Zarei V, Erfani-Moghadam V. **Use of single chain antibody derivatives for targeted drug delivery**. *Mol Med* 2016; 22:258-270.
75. Chahibi Y, Akyildiz IF, Sang Ok S. **Antibody-based molecular communication for targeted drug delivery systems**. *Annual International Conference of the IEEE Engineering in Medicine and Biology Society IEEE Engineering in Medicine and Biology Society Annual International Conference* 2014; 2014:5707-5710.
76. He F, Wen N, Xiao D, Yan J, Xiong H, Cai S, et al. **Aptamer-Based Targeted Drug Delivery Systems: Current Potential and Challenges**. *Current medicinal chemistry* 2020; 27(13):2189-2219.
77. Edelmann MJ, Kima PE. **Current understanding of extracellular vesicle homing/tropism**. *Zoonoses (Burlingt)* 2022; 2:14.
78. Zahednezhad F, Saadat M, Valizadeh H, Zakeri-Milani P, Baradaran B. **Liposome and immune system interplay: Challenges and potentials**. *Journal of Controlled Release* 2019; 305:194-209.
79. Familtseva A, Jeremic N, Tyagi SC. **Exosomes: cell-created drug delivery systems**. *Molecular and cellular biochemistry* 2019; 459(1-2):1-6.
80. Raghav A, Jeong GB. **A systematic review on the modifications of extracellular vesicles: a revolutionized tool of nano-biotechnology**. *J Nanobiotechnology* 2021; 19(1):459.
81. Kodam SP, Ullah M. **Diagnostic and Therapeutic Potential of Extracellular Vesicles**. *Technol Cancer Res Treat* 2021; 20:15330338211041203.
82. Paolini L, Monguió-Tortajada M, Costa M, Antenucci F, Barilani M, Clos-Sansalvador M, et al. **Large-scale production of extracellular vesicles: Report on the "massivEVs" ISEV workshop**. *Journal of Extracellular Biology* 2022; 1(10):e63.
83. Bazzan E, Tine M, Casara A, Biondini D, Semenzato U, Cocconcelli E, et al. **Critical Review of the Evolution of Extracellular Vesicles' Knowledge: From 1946 to Today**. *Int J Mol Sci* 2021; 22(12):6417.
84. Claridge B, Lozano J, Poh QH, Greening DW. **Development of Extracellular Vesicle Therapeutics: Challenges, Considerations, and Opportunities**. *Front Cell Dev Biol* 2021; 9:734720.
85. Antimisiaris SG, Mourtas S, Marazioti A. **Exosomes and Exosome-Inspired Vesicles for Targeted Drug Delivery**. *Pharmaceutics* 2018; 10(4):218.
86. Li YJ, Wu JY, Liu J, Xu W, Qiu X, Huang S, et al. **Artificial exosomes for translational nanomedicine**. *J Nanobiotechnology* 2021; 19(1):242.
87. Piffoux M, Silva AKA, Gazeau F, Tareste D. **Generation of Hybrid Extracellular Vesicles by Fusion with Functionalized Liposomes**. *Methods Mol Biol* 2022; 2473:385-396.

88. Li Q, Song Y, Wang Q, Chen J, Gao J, Tan H, et al. **Engineering extracellular vesicles with platelet membranes fusion enhanced targeted therapeutic angiogenesis in a mouse model of myocardial ischemia reperfusion**. *Theranostics* 2021; 11(8):3916-3931.
89. Lunavat TR, Jang SC, Nilsson L, Park HT, Repiska G, Lasser C, et al. **RNAi delivery by exosome-mimetic nanovesicles - Implications for targeting c-Myc in cancer**. *Biomaterials* 2016; 102:231-238.
90. Lau HC, Han DW, Park J, Lehner E, Kals C, Arzt C, et al. **GMP-compliant manufacturing of biologically active cell-derived vesicles produced by extrusion technology**. *Journal of Extracellular Biology* 2022; 1(12):e70.
91. Garcia-Manrique P, Matos M, Gutierrez G, Pazos C, Blanco-Lopez MC. **Therapeutic biomaterials based on extracellular vesicles: classification of bio-engineering and mimetic preparation routes**. *J Extracell Vesicles* 2018; 7(1):1422676.
92. Garcia-Manrique P, Gutierrez G, Blanco-Lopez MC. **Fully Artificial Exosomes: Towards New Theranostic Biomaterials**. *Trends Biotechnol* 2018; 36(1):10-14.
93. Martinez-Lostao L, Garcia-Alvarez F, Basanez G, Alegre-Aguaron E, Desportes P, Larrad L, et al. **Liposome-bound APO2L/TRAIL is an effective treatment in a rabbit model of rheumatoid arthritis**. *Arthritis Rheum* 2010; 62(8):2272-2282.
94. Lu L, Ding Y, Zhang Y, Ho RJ, Zhao Y, Zhang T, et al. **Antibody-modified liposomes for tumor-targeting delivery of timosaponin AIII**. *Int J Nanomedicine* 2018; 13:1927-1944.
95. Jo W, Kim J, Yoon J, Jeong D, Cho S, Jeong H, et al. **Large-scale generation of cell-derived nanovesicles**. *Nanoscale* 2014; 6(20):12056-12064.
96. Luan X, Sansanaphongpricha K, Myers I, Chen H, Yuan H, Sun D. **Engineering exosomes as refined biological nanoplatforms for drug delivery**. *Acta Pharmacol Sin* 2017; 38(6):754-763.
97. Mitchell MJ, Billingsley MM, Haley RM, Wechsler ME, Peppas NA, Langer R. **Engineering precision nanoparticles for drug delivery**. *Nat Rev Drug Discov* 2021; 20(2):101-124.
98. Han HS, Lee H, You D, Nguyen VQ, Song DG, Oh BH, et al. **Human adipose stem cell-derived extracellular nanovesicles for treatment of chronic liver fibrosis**. *J Control Release* 2020; 320:328-336.
99. Ilahibaks NF, Lei Z, Mol EA, Deshantri AK, Jiang L, Schiffelers RM, et al. **Biofabrication of Cell-Derived Nanovesicles: A Potential Alternative to Extracellular Vesicles for Regenerative Medicine**. *Cells* 2019; 8(12):1509.
100. Jeong D, Jo W, Yoon J, Kim J, Gianchandani S, Gho YS, et al. **Nanovesicles engineered from ES cells for enhanced cell proliferation**. *Biomaterials* 2014; 35(34):9302-9310.
101. Ko KW, Yoo YI, Kim JY, Choi B, Park SB, Park W, et al. **Attenuation of Tumor Necrosis Factor-alpha Induced Inflammation by Umbilical Cord-Mesenchymal Stem Cell Derived Exosome-Mimetic Nanovesicles in Endothelial Cells**. *Tissue Eng Regen Med* 2020; 17(2):155-162.
102. Nasiri Kenari A, Kastaniegaard K, Greening DW, Shambrook M, Stensballe A, Cheng L, et al. **Proteomic and Post-Translational Modification Profiling of Exosome-Mimetic Nanovesicles Compared to Exosomes**. *Proteomics* 2019; 19(8):e1800161.
103. Al Shoyaib A, Archie SR, Karamyan VT. **Intraperitoneal Route of Drug Administration: Should it Be Used in Experimental Animal Studies?** *Pharmaceutical research* 2019; 37(1):12.
104. Roth L, Russo L, Ulugoel S, Freire Dos Santos R, Breuer E, Gupta A, et al. **Peritoneal Metastasis: Current Status and Treatment Options**. *Cancers (Basel)* 2021; 14(1):60.
105. Flessner MF. **Pharmacokinetic problems in peritoneal drug administration: an update after 20 years**. *Pleura and peritoneum* 2016; 1(4):183-191.
106. Borchers A, Pieler T. **Programming pluripotent precursor cells derived from Xenopus embryos to generate specific tissues and organs**. *Genes (Basel)* 2010; 1(3):413-426.
107. Habibullah CM, Syed IH, Qamar A, Taher-Uz Z. **Human fetal hepatocyte transplantation in**

patients with fulminant hepatic failure. *Transplantation* 1994; 58(8):951-952.
108. Zivko C, Fuhrmann K, Fuhrmann G, Luciani P. **Following the SPARC: tracking Secreted Protein Acidic and Rich in Cysteine associated with LX-2´s extracellular vesicles as a non-destructive modality to evaluate lipid-based antifibrotic treatments**. *Commun Biol* 2021; 5(1):1155.
109. Lee H, Cha H, Park JH. **Derivation of Cell-Engineered Nanovesicles from Human Induced Pluripotent Stem Cells and Their Protective Effect on the Senescence of Dermal Fibroblasts**. *Int J Mol Sci* 2020; 21(1):343.
110. Wu JY, Ji AL, Wang ZX, Qiang GH, Qu Z, Wu JH, et al. **Exosome-Mimetic Nanovesicles from Hepatocytes promote hepatocyte proliferation in vitro and liver regeneration in vivo**. *Sci Rep* 2018; 8(1):2471.
111. Shehadul Islam M, Aryasomayajula A, Selvaganapathy P. **A Review on Macroscale and Microscale Cell Lysis Methods**. *Micromachines* 2017; 8(3):83.
112. Saranya N, Devi P, Nithiyanantham S, Jeyalaxmi R. **Cells Disruption by Ultrasonication**. *BioNanoScience* 2014; 4(4):335-337.
113. Qi X, Sun Y, Xiong S. **A single freeze-thawing cycle for highly efficient solubilization of inclusion body proteins and its refolding into bioactive form**. *Microb Cell Fact* 2015; 14:24.
114. Kakarla R, Hur J, Kim YJ, Kim J, Chwae YJ. **Apoptotic cell-derived exosomes: messages from dying cells**. *Exp Mol Med* 2020; 52(1):1-6.
115. Moore DS, Notz, W. I, & Flinger, M. A. . **The Basic Practice of Statistics**. *W H Freeman and Company* 2013; 6(2).
116. Monguio-Tortajada M, Galvez-Monton C, Bayes-Genis A, Roura S, Borras FE. **Extracellular vesicle isolation methods: rising impact of size-exclusion chromatography**. *Cell Mol Life Sci* 2019; 76(12):2369-2382.
117. Clos-Sansalvador M, Monguio-Tortajada M, Roura S, Franquesa M, Borras FE. **Commonly used methods for extracellular vesicles' enrichment: Implications in downstream analyses and use**. *Eur J Cell Biol* 2022; 101(3):151227.
118. Sharma S, LeClaire M, Wohlschlegel J, Gimzewski J. **Impact of isolation methods on the biophysical heterogeneity of single extracellular vesicles**. *Sci Rep* 2020; 10(1):13327.
119. Mercadal M, Herrero C, Lopez-Rodrigo O, Castells M, de la Fuente A, Vigues F, et al. **Impact of Extracellular Vesicle Isolation Methods on Downstream Mirna Analysis in Semen: A Comparative Study**. *Int J Mol Sci* 2020; 21(17):5949.
120. Cocozza F, Grisard E, Martin-Jaular L, Mathieu M, Thery C. **SnapShot: Extracellular Vesicles**. *Cell* 2020; 182(1):262-262 e261.
121. Brennan K, Martin K, FitzGerald SP, O'Sullivan J, Wu Y, Blanco A, et al. **A comparison of methods for the isolation and separation of extracellular vesicles from protein and lipid particles in human serum**. *Sci Rep* 2020; 10(1):1039.
122. Bano R, Ahmad F, Mohsin M. **A perspective on the isolation and characterization of extracellular vesicles from different biofluids**. *RSC Adv* 2021; 11(32):19598-19615.
123. Yang Y, Wang Y, Wei S, Zhou C, Yu J, Wang G, et al. **Extracellular vesicles isolated by size-exclusion chromatography present suitability for RNomics analysis in plasma**. *J Transl Med* 2021; 19(1):104.
124. Benedikter BJ, Bouwman FG, Vajen T, Heinzmann ACA, Grauls G, Mariman EC, et al. **Ultrafiltration combined with size exclusion chromatography efficiently isolates extracellular vesicles from cell culture media for compositional and functional studies**. *Sci Rep* 2017; 7(1):15297.
125. Kowal J AG, Colombo M, Jouve M, Morath JP, Primdal-Bengtson B, Dingli F, Loew D, Tkach M, Théry C. **Proteomic comparison defines novel markers to characterize heterogeneous populations of extracellular vesicle subtypes**. *Proc Natl Acad Sci U S A* 2016; 113(8):E968-977.
126. Busatto S, Vilanilam G, Ticer T, Lin WL, Dickson DW, Shapiro S, et al. **Tangential Flow Filtration for Highly Efficient Concentration of Extracellular Vesicles from Large Volumes of Fluid**. *Cells* 2018; 7(12):273.
127. Beck S, Hochreiter B, Schmid JA. **Extracellular Vesicles Linking Inflammation,**

Cancer and Thrombotic Risks. *Front Cell Dev Biol* 2022; 10:859863.
128. Karttunen J, Heiskanen M, Navarro-Ferrandis V, Das Gupta S, Lipponen A, Puhakka N, et al. **Precipitation-based extracellular vesicle isolation from rat plasma co-precipitate vesicle-free microRNAs**. *J Extracell Vesicles* 2019; 8(1):1555410.
129. Meggiolaro A, Moccia V, Brun P, Pierno M, Mistura G, Zappulli V, et al. **Microfluidic Strategies for Extracellular Vesicle Isolation: Towards Clinical Applications**. *Biosensors (Basel)* 2022; 13(1):50.
130. Lu J, Pang J, Chen Y, Dong Q, Sheng J, Luo Y, et al. **Application of Microfluidic Chips in Separation and Analysis of Extracellular Vesicles in Liquid Biopsy for Cancer**. *Micromachines (Basel)* 2019; 10(6):390.
131. Guo SC, Tao SC, Dawn H. **Microfluidics-based on-a-chip systems for isolating and analysing extracellular vesicles**. *J Extracell Vesicles* 2018; 7(1):1508271.
132. Visan KS, Lobb RJ, Ham S, Lima LG, Palma C, Edna CPZ, et al. **Comparative analysis of tangential flow filtration and ultracentrifugation, both combined with subsequent size exclusion chromatography, for the isolation of small extracellular vesicles**. *J Extracell Vesicles* 2022; 11(9):e12266.
133. **OptiPrep™ The ideal density gradient medium for isolation of cells**. *Harvard medical school*.
134. Wonju Jo DJ, Junho Kim, Siwoo Cho, Su Chul Jang,, Chungmin Han JYK, Yong Song Gho and Jaesung Park. **Microfluidic fabrication of cell-derived nanovesicles as endogenous RNA carriers**. *Royal Society of Chemistry* 2014; 14:1261-1269.
135. Boing AN, van der Pol E, Grootemaat AE, Coumans FA, Sturk A, Nieuwland R. **Single-step isolation of extracellular vesicles by size-exclusion chromatography**. *J Extracell Vesicles* 2014; 3(1):23430.
136. Muller L, Hong CS, Stolz DB, Watkins SC, Whiteside TL. **Isolation of biologically-active exosomes from human plasma**. *J Immunol Methods* 2014; 411:55-65.
137. Gorgens A, Corso G, Hagey DW, Jawad Wiklander R, Gustafsson MO, Felldin U, et al. **Identification of storage conditions stabilizing extracellular vesicles preparations**. *J Extracell Vesicles* 2022; 11(6):e12238.
138. Ağalar HG. **Chapter 10 - Influence of vitamins (C, B3, D, and E) in liver health**. In: *Influence of Nutrients, Bioactive Compounds, and Plant Extracts in Liver Diseases*. Alavian SM, Nabavi SM, Nabavi SF, Silva AS (editors): Academic Press; 2021. pp. 175-191.
139. Woolbright BL, Jaeschke H. **Chapter Five - Xenobiotic and Endobiotic Mediated Interactions Between the Cytochrome P450 System and the Inflammatory Response in the Liver**. In: *Advances in Pharmacology*. Hardwick JP (editor): Academic Press; 2015. pp. 131-161.
140. Potter BJ. **Liver-Plasma Protein Synthesis**. In: *Reference Module in Biomedical Sciences*: Elsevier; 2014.
141. Speliotes EK, Balakrishnan M, Friedman LS, Corey KE. **Treatment of Dyslipidemia in Common Liver Diseases**. *Clinical Liver Disease* 2019; 14(5):161-162.
142. Kubes P, Jenne C. **Immune Responses in the Liver**. *Annu Rev Immunol* 2018; 36(26):247-277.
143. Bataller R, Brenner DA. **Liver fibrosis**. *Journal of Clinical Investigation* 2005; 115(2):209-218.
144. Shmarakov IO, Jiang H, Liu J, Fernandez EJ, Blaner WS. **Hepatic stellate cell activation: A source for bioactive lipids**. *Biochim Biophys Acta Mol Cell Biol Lipids* 2019; 1864(5):629-642.
145. Scholz N. **Organ donation and transplantation Facts, figures and European Union action**. *EPRS | European Parliamentary Research Service* 2020; PE 646.36.
146. Povero D, Pinatel EM, Leszczynska A, Goyal NP, Nishio T, Kim J, et al. **Human induced pluripotent stem cell-derived extracellular vesicles reduce hepatic stellate cell activation and liver fibrosis**. *JCI Insight* 2019; 5(14):e125652.
147. Takuma Tsuchida SLF. **Mechanisms of hepatic stellate cell activation**. *Nat Rev Gastroenterol Hepatol* 2017 14(7):397-411.
148. Ramón Bataller MD, David A. Brenner, M.D. **Hepatic Stellate Cells as a Target for the**

Treatment of Liver Fibrosis. *Seminars in Liver Disease* 2001; 21(3):437-452.
149. Gandhi CR. **Hepatic stellate cell activation and pro-fibrogenic signals**. *J Hepatol* 2017; 67(5):1104-1105.
150. Collaborators GDaIIaP. **Global, regional, and national incidence, prevalence, and years lived with disability for 354 diseases and injuries for 195 countries and territories, 1990–2017: a systematic analysis for the Global Burden of Disease Study 2017**. *Lancet* 2018; 392:1789-1858.
151. Ng M, Fleming T, Robinson M, Thomson B, Graetz N, Margono C, et al. **Global, regional, and national prevalence of overweight and obesity in children and adults during 1980–2013: a systematic analysis for the Global Burden of Disease Study 2013**. *The Lancet* 2014; 384(9945):766-781.
152. Gamkrelidze I PJ, Lazarus JV, Feld JJ, Zeuzem S, Bao Y, Gabriela Pires Dos Santos A, Sanchez Gonzalez Y, Razavi H. **Progress towards hepatitis C virus elimination in high-income countries: An updated analysis**. *Liver international* 2021; 41(3):456-463.
153. Eun Jeong Park, Onmanee Prajuabjinda,,Zay Yar Soe, Samuel Darkwah, Michael G. Appiah, Eiji Kawamoto, Fumiyasu Momose,, Hiroshi Shiku aMS. **Exosomal regulation of lymphocyte homing to the gut**. *blood advances* 2018; 3(1):1-11.
154. Garofalo M, Villa A, Crescenti D, Marzagalli M, Kuryk L, Limonta P, et al. **Heterologous and cross-species tropism of cancer-derived extracellular vesicles**. *Theranostics* 2019; 9(19):5681-5693.
155. Zhang N, Song Y, Huang Z, Chen J, Tan H, Yang H, et al. **Monocyte mimics improve mesenchymal stem cell-derived extracellular vesicle homing in a mouse MI/RI model**. *Biomaterials* 2020; 255:120168.
156. Chen L, Brenner DA, Kisseleva T. **Combatting Fibrosis: Exosome-Based Therapies in the Regression of Liver Fibrosis**. *Hepatol Commun* 2019; 3(2):180-192.
157. Bruno S, Chiabotto G, Camussi G. **Extracellular Vesicles: A Therapeutic Option for Liver Fibrosis**. *Int J Mol Sci* 2020; 21(12):4255.
158. Chen L, Chen R, Velazquez VM, Brigstock DR. **Fibrogenic Signaling Is Suppressed in Hepatic Stellate Cells through Targeting of Connective Tissue Growth Factor (CCN2) by Cellular or Exosomal MicroRNA-199a-5p**. *Am J Pathol* 2016; 186(11):2921-2933.
159. Lee YS, Kim SY, Ko E, Lee JH, Yi HS, Yoo YJ, et al. **Exosomes derived from palmitic acid-treated hepatocytes induce fibrotic activation of hepatic stellate cells**. *Sci Rep* 2017; 7(1):3710.
160. Borges FT, Melo SA, Ozdemir BC, Kato N, Revuelta I, Miller CA, et al. **TGF-beta1-containing exosomes from injured epithelial cells activate fibroblasts to initiate tissue regenerative responses and fibrosis**. *J Am Soc Nephrol* 2013; 24(3):385-392.
161. Li G, Chen T, Dahlman J, Eniola-Adefeso L, Ghiran IC, Kurre P, et al. **Current challenges and future directions for engineering extracellular vesicles for heart, lung, blood and sleep diseases**. *J Extracell Vesicles* 2023; 12(2):e12305.
162. Kaneti L, Bronshtein T, Malkah Dayan N, Kovregina I, Letko Khait N, Lupu-Haber Y, et al. **Nanoghosts as a Novel Natural Nonviral Gene Delivery Platform Safely Targeting Multiple Cancers**. *Nano Lett* 2016; 16(3):1574-1582.
163. Carson JP, Robinson MW, Ramm GA, Gobert GN. **RNA sequencing of LX-2 cells treated with TGF-beta1 identifies genes associated with hepatic stellate cell activation**. *Mol Biol Rep* 2021; 48(12):7677-7688.
164. El Taghdouini A, Najimi M, Sancho-Bru P, Sokal E, van Grunsven LA. **In vitro reversion of activated primary human hepatic stellate cells**. *Fibrogenesis Tissue Repair* 2015; 8:14.
165. Nakatani K, Seki S, Kawada N, Kitada T, Yamada T, Sakaguchi H, et al. **Expression of SPARC by activated hepatic stellate cells and its correlation with the stages of fibrogenesis in human chronic hepatitis**. *Virchows Arch* 2002; 441(5):466-474.
166. Qi Yan EHS. **SPARC, a Matricellular Glycoprotein with Important Biological Functions**. *Journal of Histochemistry & Cytochemistry* 1999; 47(12):1495-1505.
167. Molenaar MR, Vaandrager AB, Helms JB. **Some Lipid Droplets Are More Equal Than Others: Different Metabolic Lipid Droplet Pools**

in Hepatic Stellate Cells. *Lipid Insights* 2017; 10:1178635317747281.
168. Dewidar B, Meyer C, Dooley S, Meindl-Beinker AN. **TGF-beta in Hepatic Stellate Cell Activation and Liver Fibrogenesis-Updated 2019**. *Cells* 2019; 8(11):1419.
169. O'Mahony F, Wroblewski K, O'Byrne SM, Jiang H, Clerkin K, Benhammou J, et al. **Liver X receptors balance lipid stores in hepatic stellate cells through Rab18, a retinoid responsive lipid droplet protein**. *Hepatology* 2015; 62(2):615-626.
170. He L, Yuan H, Liang J, Hong J, Qu C. **Expression of hepatic stellate cell activation-related genes in HBV-, HCV-, and nonalcoholic fatty liver disease-associated fibrosis**. *PLoS One* 2020; 15(5):e0233702.
171. Wolf M, Poupardin RW, Ebner-Peking P, Andrade AC, Blochl C, Obermayer A, et al. **A functional corona around extracellular vesicles enhances angiogenesis, skin regeneration and immunomodulation**. *J Extracell Vesicles* 2022; 11(4):e12207.
172. Fausto Gueths Gomes ACA, Martin Wolf, Sarah Hochmann, Linda Krisch,, Nicole Maeding CR, Rodolphe Poupardin, Patricia Ebner-Peking, Christian G. Huber,, Nicole Meisner-Kober KSaDS. **Synergy of Human Platelet-Derived Extracellular Vesicles with Secretome Proteins Promotes Regenerative Functions**. *biomedicines* 2022; 2(10):413-426.
173. Cesi G, Walbrecq G, Margue C, Kreis S. **Transferring intercellular signals and traits between cancer cells: extracellular vesicles as "homing pigeons"**. *Cell Commun Signal* 2016; 14(1):13.
174. Park J, Lee H, Youn YS, Oh KT, Lee ES. **Tumor-Homing pH-Sensitive Extracellular Vesicles for Targeting Heterogeneous Tumors**. *Pharmaceutics* 2020; 12(4):372.
175. Williams C, Royo F, Aizpurua-Olaizola O, Pazos R, Boons GJ, Reichardt NC, et al. **Glycosylation of extracellular vesicles: current knowledge, tools and clinical perspectives**. *J Extracell Vesicles* 2018; 7(1):1442985.
176. Paolini L, Monguió-Tortajada M, Costa M, Antenucci F, Barilani M, Clos-Sansalvador M, et al. **Large-scale production of extracellular vesicles: Report on the "massivEVs" ISEV workshop**. *Journal of Extracellular Biology* 2022; 1(10):e63.
177. Shuang Wang KL, Eliana Pickholz , Ross Dobie , Kylie P Matchett , Neil C Henderson , Chris Carrico, Ian Driver , Martin Borch Jensen , Li Chen , Mathieu Petitjean , Dipankar Bhattacharya, Maria I Fiel, Xiao Liu , Tatiana Kisseleva , Uri Alon, Miri Adler , Ruslan Medzhitov , Scott L Friedman **An autocrine signaling circuit in hepatic stellate cells underlies advanced fibrosis in nonalcoholic steatohepatitis**. *Science Translational Medicine* 2023; 15(667):eadd3949.
178. Ng CY, Kee LT, Al-Masawa ME, Lee QH, Subramaniam T, Kok D, et al. **Scalable Production of Extracellular Vesicles and Its Therapeutic Values: A Review**. *Int J Mol Sci* 2022; 23(14):7986.
179. Lee UE, Friedman SL. **Mechanisms of hepatic fibrogenesis**. *Best Pract Res Clin Gastroenterol* 2011; 25(2):195-206.
180. Xiayu Rao XH, Zhicheng Zhou, and Xin Lin. **An improvement of the 2ˆ(–delta delta CT) method for quantitative real-time polymerase chain reaction data analysis**. *Biostat Bioinforma Biomath* 2013; 3(3):71-85.
181. Roy P, Mignet N, Pocard M, Boudy V. **Drug delivery systems to prevent peritoneal metastasis after surgery of digestives or ovarian carcinoma: A review**. *Int J Pharm* 2021; 592:120041.
182. Mohamed F, Sugarbaker PH. **Carrier solutions for intraperitoneal chemotherapy**. *Surgical oncology clinics of North America* 2003; 12(3):813-824.
183. Mirahmadi N, Babaei MH, Vali AM, Dadashzadeh S. **Effect of liposome size on peritoneal retention and organ distribution after intraperitoneal injection in mice**. *Int J Pharm* 2010; 383(1-2):7-13.
184. Kumar P, Mangla B, Javed S, Ahsan W, Musyuni P, Ahsan A, et al. **Gefitinib: An Updated Review of its Role in the Cancer Management, its Nanotechnological Interventions, Recent Patents and Clinical Trials**. *Recent patents on anti-cancer drug discovery* 2023; 18(4):448-469.

185. Kazandjian D, Blumenthal GM, Yuan W, He K, Keegan P, Pazdur R. **FDA Approval of Gefitinib for the Treatment of Patients with Metastatic EGFR Mutation–Positive Non–Small Cell Lung Cancer**. *Clinical Cancer Research* 2016; 22(6):1307-1312.
186. Zindel J, Mittner J, Bayer J, April-Monn SL, Kohler A, Nusse Y, et al. **Intraperitoneal microbial contamination drives post-surgical peritoneal adhesions by mesothelial EGFR-signaling**. *Nat Commun* 2021; 12(1):7316.
187. Hu Y, Zhang J, Hu H, Xu S, Xu L, Chen E. **Gefitinib encapsulation based on nano-liposomes for enhancing the curative effect of lung cancer**. *Cell Cycle* 2020; 19(24):3581-3594.
188. van Zandwijk N. **Tolerability of gefitinib in patients receiving treatment in everyday clinical practice**. *British journal of cancer* 2003; 89 Suppl 2(Suppl 2):S9-14.
189. Farshidfar N, Iravani S, Varma RS. **Alginate-Based Biomaterials in Tissue Engineering and Regenerative Medicine**. *Marine Drugs* 2023; 21(3):189.
190. Posiseeva LV, Gerasimov AM, Shokhina MN, Kuz'menko GN. **[Magnesium and calcium ion levels in peritoneal fluid of healthy fertile women]**. *Klinicheskaia laboratornaia diagnostika* 2001; (8):21-23.
191. Grassi M, Sandolo C, Perin D, Coviello T, Lapasin R, Grassi G. **Structural Characterization of Calcium Alginate Matrices by Means of Mechanical and Release Tests**. *Molecules (Basel, Switzerland)* 2009; 14(8):3003-3017.
192. Kitayama J, Ishigami H, Yamaguchi H, Sakuma Y, Horie H, Hosoya Y, et al. **Treatment of patients with peritoneal metastases from gastric cancer**. *Annals of gastroenterological surgery* 2018; 2(2):116-123.
193. Wen H, Xiao W, Biswas S, Cong ZQ, Liu XM, Lam KS, et al. **Alginate Hydrogel Modified with a Ligand Interacting with α3β1 Integrin Receptor Promotes the Differentiation of 3D Neural Spheroids toward Oligodendrocytes in Vitro**. *ACS Appl Mater Interfaces* 2019; 11(6):5821-5833.
194. Bansal D, Gulbake A, Tiwari J, Jain SK. **Development of liposomes entrapped in alginate beads for the treatment of colorectal cancer**. *International Journal of Biological Macromolecules* 2016; 82:687-695.
195. Rahnfeld L, Luciani P. **Injectable Lipid-Based Depot Formulations: Where Do We Stand?** *Pharmaceutics* 2020; 12(6):567.
196. Rahnfeld L, Thamm J, Steiniger F, van Hoogevest P, Luciani P. **Study on the in situ aggregation of liposomes with negatively charged phospholipids for use as injectable depot formulation**. *Colloids and surfaces B, Biointerfaces* 2018; 168:10-17.
197. Herrick SE, Wilm B. **Post-Surgical Peritoneal Scarring and Key Molecular Mechanisms**. *Biomolecules* 2021; 11(5):692.
198. Wang R, Guo T, Li J. **Mechanisms of Peritoneal Mesothelial Cells in Peritoneal Adhesion**. *Biomolecules* 2022; 12(10):1498.
199. Takehara K, Yuki K, Shirasawa M, Yamasaki S, Yamada S. **Binding properties of hydrophobic molecules to human serum albumin studied by fluorescence titration**. *Analytical sciences : the international journal of the Japan Society for Analytical Chemistry* 2009; 25(1):115-120.
200. van de Wouw J, Joles JA. **Albumin is an interface between blood plasma and cell membrane, and not just a sponge**. *Clinical Kidney Journal* 2021; 15(4):624-634.
201. Kopp W. **How Western Diet And Lifestyle Drive The Pandemic Of Obesity And Civilization Diseases**. *Diabetes Metab Syndr Obes* 2019; 12:2221-2236.
202. Moon AM, Singal AG, Tapper EB. **Contemporary Epidemiology of Chronic Liver Disease and Cirrhosis**. *Clinical Gastroenterology and Hepatology* 2020; 18(12):2650-2666.
203. Kim D, Touros A, Kim WR. **Nonalcoholic Fatty Liver Disease and Metabolic Syndrome**. *Clinics in liver disease* 2018; 22(1):133-140.
204. Devarbhavi H, Asrani SK, Arab JP, Nartey YA, Pose E, Kamath PS. **Global burden of Liver Disease: 2023 Update**. *Journal of Hepatology* 2023.
205. Zivko C, Witt F, Koeberle A, Fuhrmann G, Luciani P. **Formulating elafibranor and obeticholic acid with phospholipids decreases drug-induced association of SPARC to extracellular vesicles from LX-2 human hepatic**

stellate cells. *European Journal of Pharmaceutics and Biopharmaceutics* 2023; 182:32-40.
206. de Abreu RC, Ramos CV, Becher C, Lino M, Jesus C, da Costa Martins PA, et al. **Exogenous loading of miRNAs into small extracellular vesicles**. *J Extracell Vesicles* 2021; 10(10):e12111.

Acknowledgements

First, I would like to thank Prof. Gregor Fuhrmann and Prof. Paola Luciani for revising my thesis and Prof. Christoph von Ballmoos for chairing my PhD Defence.

Hereby, I would like to express my gratitude to Prof. Paola Luciani for giving me the opportunity to work in her research group, as well as helping to build the pharmaceutical sciences at the University of Bern. I could accumulate endless knowledge in the field of drug delivery and extracellular vesicles during those 3.5 years. I want to especially thank you for always encouraging me and trying your best to allow me to go to various national and international conferences, which for me were the best part of the PhD, as it always was a huge honour to discuss science with experts from the field. Even though, we also had a few difficult times, I am extremely grateful for this experience that allowed me to mature, not only into a better scientist, but overall, into a better person. I would also like to thank all former and current Luciani group members, especially "my generation" Ivo, Marianna, and Gregor, but also Cristina, Florian, and Gina for various scientific, as well as non-scientific discussion which were always very refreshing. A special mention goes to my former Master Student Amirmohammad Seidi from whom I learned a lot while teaching him and hope he could also take a few useful things for his path.

I would also like to thank all my family and friends for always supporting me, but also letting me digress from science during free time, allowing me to go back to the lab with a fresh mind when I needed it.

Finally, I would like to express my deepest and most sincere gratitude to my wife, Alexandra, who has always been on my side no matter what. You were always giving me your understanding

and support for everything I faced during my PhD. You always made sure I have everything I need to be in optimal conditions and sacrificed a lot to be there for me. Thank you for everything! I feel truly blessed to having you!

Declaration of consent

on the basis of Article 18 of the PromR Phil.-nat. 19

Name/First Name: Ganguin, Aymar Abel

Registration Number: 13-113-246

Study program: Dissertation

Title of the thesis: Bioderived therapeutics for chronic liver diseases

Supervisor: Prof. Dr. Paola Luciani

I declare herewith that this thesis is my own work and that I have not used any sources other than those stated. I have indicated the adoption of quotations as well as thoughts taken from other authors
as such in the thesis. I am aware that the Senate pursuant to Article 36 paragraph 1 litera r of the University Act of September 5th, 1996 and Article 69 of the University Statute of June 7th, 2011 is
authorized to revoke the doctoral degree awarded on the basis of this thesis.
For the purposes of evaluation and verification of compliance with the declaration of originality and the
regulations governing plagiarism, I hereby grant the University of Bern the right to process my personal data and to perform the acts of use this requires, in particular, to reproduce the written thesis
and to store it permanently in a database, and to use said database, or to make said database available, to enable comparison with theses submitted by others.

Place/Date

Bern, 04.04.2023

Signature

Aymar Abel Ganguin